Studying Ca2+ channel function at sub-micron spatial resolution

Luiza Filipis

Communauté
UNIVERSITÉ Grenoble Alpes

THÈSE

Pour obtenir le grade de

DOCTEUR DE LA COMMUNAUTE UNIVERSITE GRENOBLE ALPES

Spécialité : **Physique pour les sciences du vivant**

Arrêté ministériel : 25 mai 2016

Présentée par

Luiza FILIPIS

Thèse dirigée par **Marco CANEPARI, CR Inserm,** Université Grenoble Alpes et CNRS UMR 5588

Préparée au sein du **Laboratoire Interdisciplinaire de Physique** dans **l'École Doctorale de Physique de Grenoble**

Etude optique et computationnelle de la fonction des canaux ioniques neuronaux

Thèse soutenue publiquement le **19 Décembre 2019** , devant le jury composé de :

Mr, Bertrand, FOURCADE
PR UGA – LIPhy Grenoble, Président
Mr Massimo, MANTEGAZZA
DR Inserm – IPMC Nice, Rapporteur
Mr Stéphane, DIEUDONNE
DR Inserm – ENS Paris, Rapporteur
Mme, Eirini, PAPAGIAKOUMOU
CR Inserm – Institut de la Vision, Paris, Membre
Mme, Cécile, DELACOUR
CR CNRS – Institut Néel Grenoble, Membre

Acknowledgements

This dissertation is the product of support from many people to whom I owe gratitude. My deepest gratitude goes to my supervisor, Dr. Marco Canepari, for giving me the chance to be part of this project, mentored me, guided me, inspired me and believed in me. It is a privilege to have made my first steps in neuroscience next to such an impressive scientist and person whose intelligence, wisdom and integrity have shaped me both as a scientist and a person and will follow me through all my next steps.

It was likewise an honor to collaborate with Dr. Panayota Poirazi and her team in IMBB. I would like to thank her for introducing me into computational neuroscience and furthermore for standing as an example of a woman leader in neuroscience. I would like to especially thank Alexandra Tzilivaki from this team for our productive collaboration that evolved into a nice friendship and will hopefully continue through the years to come.

I would also like to thank my co-workers and friends in LIPhy for making the time I spent in this laboratory a unique experience.

Lastly, I would most certainly like to thank my family and friends who have always been by my side, offering their love and support unconditionally.

Abstract (in English)

The physiology of ion channels is a major topic of interest in modern neuroscience since the functioning of these molecules is the biophysical ground of electrical and chemical behaviour of neurons. Ion channels are diverse membrane proteins that allow the selective passage of ions across the lipid bilayer of cells. They are involved in a variety of fundamental physiological processes from electrical signal integration, action potential generation and propagation to cell growth and even apoptosis, while their dysfunction is the cause of several diseases. Ion channels have extensively studied using electrode methods, in particular the patch-clamp technique, but these approaches are limited in studying native channels during physiological activity in situ. In particular, electrodes give limited spatial information while it is recognised that the contribution of channels in all different processes is a function not only of their discrete biophysical properties but also of their distribution across the neurons surface at the different compartments. Optical techniques, in particular those involving fluorescence imaging, can overcome intrinsic limitations of electrode techniques as they allow to record electrical and ionic signals with high spatial and temporal resolution. Finally, the ability of optical techniques combined with neuronal modelling can potentially give pivotal information significantly advancing our understanding on how neurons work.

The ambitious goal of my thesis was to progress in this direction by developing novel approaches to combine cutting-edge imaging techniques with modelling to extract ion currents and channel kinetics in specific neuronal regions. The body of this work was divided in three methodological pieces, each of them described in a dedicated chapter.

In chapter 3, I introduce a novel confocal system that I contributed in developing in our laboratory, based on a fast spinning disk, a multimode diode laser and a novel high-resolution CMOS camera. This system is highly effective in rejecting out-of-focus light to resolve signals from submicron structures in the ms range, enabling to perform multisite recordings of Ca^{2+} signals in brain slices with unrivalled spatiotemporal resolution. We characterised specific differences in Ca^{2+} transient kinetics and compartmental localisation of different calcium sources.

In chapter 4, I present a unique approach to extract the kinetics of all the channels activated by the climbing fibre input in the dendrites of cerebellar Purkinje Neurons. In this preparation, because of the numerous interacting Ca^{2+} and K^{+} channels along with several Ca^{2+} buffering mechanisms, the fluorescent Ca^{2+} signal is not a direct measurement of the

ion's influx. To deduce the kinetics of the various channels involved in generating this signal, a single compartment computational model was developed, using data from combined Ca^{2+} and voltage imaging along with pharmacological inhibition of the various channels.

Finally, in chapter 5, I demonstrate an innovative approach to measure Na^{+} currents from the neuronal axon initial segment. The method is based on dynamic Na^{+} imaging, a less exploited technique with respect to Ca^{2+} imaging that can reveal analogous information related to Na^{+} signalling. Here I introduce a technique to extract Na^{+} current kinetics associated with action potentials in the axon initial segment of Layer 5 neocortical neurons. Future perspectives of this study involve following the technique described in chapter 4 to deduce the channel kinetics involved in the recorded Na^{+} signals.

Résumé (en Français)

La physiologie des canaux ioniques est un sujet d'intérêt majeur dans les neurosciences modernes puisque le fonctionnement de ces molécules est la base biophysique du comportement électrique et chimique des neurones. Les canaux ioniques sont des protéines membranaires diverses qui permettent le passage sélectif des ions à travers la couche lipidique des cellules. Ils sont impliqués dans une variété de processus physiologiques fondamentaux, à partir de l'intégration des signaux électriques, la génération et la propagation de potentiel d'action jusqu'à la croissance cellulaire et même à l'apoptose, tandis que leur dysfonctionnement est la cause de plusieurs maladies. Les canaux ioniques ont été largement étudiés à l'aide de méthodes basés sur les électrodes, en particulier la technique du patch-clamp, mais ces approches sont limitées pour étudier les canaux natifs pendant l'activité physiologique in situ. En particulier, les électrodes fournissent des informations spatiales limitées alors qu'il est reconnu que la contribution des canaux dans tous les différents processus est fonction non seulement de leurs propriétés biophysiques discrètes, mais aussi de leur distribution dans la surface des neurones et des différents compartiments. Les techniques optiques, en particulier celles impliquant l'imagerie par fluorescence, peuvent surmonter les limites intrinsèques des techniques d'électrode car elles permettent d'enregistrer des signaux électriques et ioniques avec une résolution spatiale et temporelle élevée. Enfin, la capacité des techniques optiques combinées à la modélisation neuronale peut potentiellement fournir des informations essentielles permettant de mieux comprendre le fonctionnement des neurones. L'objectif ambitieux de ma thèse était de progresser dans cette direction en développant de nouvelles approches pour combiner des techniques d'imagerie de pointe avec la modélisation pour extraire les courants ioniques et la cinétique des canaux dans des régions neuronales spécifiques. Le corps de ce travail a été divisé en trois morceaux méthodologiques, chacun d'eux décrit dans un chapitre dédié.

Dans le chapitre 3, je présente un nouveau système confocal que j'ai développé dans notre laboratoire, basé sur un « spinning disk », un laser à diode multimode et une nouvelle caméra CMOS haute résolution. Ce système est très efficace pour rejeter la lumière hors plan focale afin de résoudre les signaux provenant de structures submicroniques dans l'échelle de millisecondes, en permettant d'effectuer des enregistrements multisites de signaux calciques dans des coupes de cerveau avec une résolution spatiale et temporelle jamais attendue auparavant. Nous avons caractérisé des différences spécifiques dans la cinétique transitoire du Ca^{2+} et la localisation spécifique de différentes sources de calcium.

Dans le chapitre 4, je présente une nouvelle approche pour extraire la cinétique de tous les canaux activés par la stimulation de la fibre grimpante dans les dendrites de neurones cérébelleux Purkinje. Dans cette préparation, en raison des nombreux canaux calciques et potassiques en interaction avec plusieurs mécanismes de tampon du Ca^{2+}, le signal fluorescent du Ca^{2+} n'est pas une mesure directe des courantes calciques. Pour déduire la cinétique des différents canaux impliqués dans la génération de ce signal, un modèle de calcul à un seul compartiment a été développé, en utilisant les données de l'imagerie combinée Ca^{2+} et du potentiel de membrane ainsi que l'inhibition pharmacologique des différents canaux.

Enfin, au chapitre 5, je présente une nouvelle approche pour mesurer les courants de Na^{+} dans le segment initial de l'axone neuronal. La méthode est basée sur l'imagerie dynamique du Na^{+}, une technique moins exploitée par rapport à l'imagerie du Ca^{2+} qui peut quand même révéler des informations analogues liées à la signalisation du Na^{+}. Je présente ici une technique pour extraire la cinétique des courantes sodiques associées aux potentiels d'action dans le segment initial de l'axone des neurones néocorticaux de la couche 5. Les perspectives futures de cette étude sont de suivre la technique décrite au chapitre 4 pour déduire la cinétique des canaux impliqués dans les signaux du Na^{+} enregistrés.

Table des matières

CHAPTER 1. INTRODUCTION....1

1.1 BASIC PRINCIPLES OF THE ELECTRICAL ACTIVITY IN NEURONS....2
1.2 HODGKIN-HUXLEY EQUATIONS AND THE ACTION POTENTIAL....5
1.3 THE NEURON AS AN ELECTRICAL CIRCUIT....8
1.4 TECHNIQUES TO EXTRACT CHANNEL KINETICS....10
1.5 STATE OF THE ART....13
1.5.1 Indicators....13
1.5.2 Imaging techniques....14
1.5.3 Light sources....17
1.5.4 The NEURON simulating platform....18
1.6 GENERAL AIM OF THIS DISSERTATION....18

CHAPTER 2. MATERIALS AND METHODS....20

2.1 ANIMALS....20
2.2 SLICE PREPARATION, SOLUTIONS AND ELECTROPHYSIOLOGY....20
2.3 PHARMACOLOGY....24
2.4 EXPERIMENTAL SETUP FOR CONFOCAL CA^{2+} IMAGING (EXPERIMENTS IN CHAPTER 3) 25
2.4.1 Spinning disk....25
2.4.2 CMOS camera....25
2.4.3 Illumination....26
2.4.4 Filters....26
2.5 EXPERIMENTAL SETUP FOR HIGH SPEED NA^{2+} IMAGING (EXPERIMENTS IN CHAPTER 5) 28
2.5.1 CMOS camera....28
2.5.2 Illumination....28
2.5.3 Filters....28
2.6 ANALYSIS AND STATISTICS....29

CHAPTER 3. A NOVEL CONFOCAL SYSTEM FOR RAPID FUNCTIONAL IMAGING IN BRAIN SLICES....31

3.1 CHARACTERIZATION OF THE CONFOCAL SYSTEM....31
3.1.1 Optical Sectioning....32
3.1.2 Temporal performance of the system....33
3.1.3 Spatial performance of the system....36
3.1.4 Bleach improvement....41
3.2 EXAMPLES....43
3.2.1 Example 1: Ca^{2+} signals associated with the Climbing Fibre....43
3.2.2 Example 2: Ca^{2+} signals associated with the Parallel Fibre....45
3.3 SIGNIFICANCE OF THIS WORK....47

CHAPTER 4. DEVELOPMENT OF A SIMPLIFIED NEURON MODEL TO EXTRACT THE ACTIVITY OF ION CHANNELS IN NEURONAL DENDRITES....49

4.1 CONSTANT PARAMETERS OF THE MODEL....52
4.1.1 Morphology....52
4.1.2 Passive membrane parameters....52

4.1.3 Leak/Shunt.....*52*
4.1.4 Ca^{2+} Buffering.....*52*
4.2 Initial Channel models and free parameters.....56
4.2.1 P/Q-type VGCC.....*58*
4.2.2 T-type VGCC.....*58*
4.2.3 A-type VGKC.....*59*
4.2.4 HVA VGKC.....*60*
4.2.5 BK Ca^{2+}-activated K^+ channel.....*61*
4.2.6 SK Ca^{2+}-activated K^+ channel.....*62*
4.3 Model of the CF-associated current.....62
4.4 Parameters of the channel kinetics.....63
4.4.1 P/Q-type VGCC.....*64*
4.4.2 T-type VGCC.....*64*
4.4.3 A-type VGKC.....*65*
4.4.4 HVA VGKC.....*66*
4.4.5 BK Ca^{2+}-activated K^+ channel.....*66*
4.4.6 SK Ca^{2+}-activated K^+ channel.....*67*
4.5 Tuning the model to reproduce the experimental data.....69
4.6 Validation of the model.....72
4.7 Extraction of channel currents.....74
4.8 Importance of CF-activated channels and of this novel approach.....76

CHAPTER 5. IMAGING AXONAL SODIUM INFLUX AT HIGH SPATIAL AND TEMPORAL RESOLUTION.....80

5.1 Quantitative evaluation of data from Na^+ imaging experiments.....83
5.1.1 Spatial and temporal alignment of trials.....*83*
5.1.2 Image analysis, spatial averaging and bleach correction.....*84*
5.1.3 Calibration of Na^+ signals.....*85*
5.1.4 Block of Na^{2+} signals.....*87*
5.2 Spatial distribution of Na^+.....89
5.3 Evaluation and correction for Na^+ lateral diffusion.....92
5.4 Evaluation and correction for Na^+ lateral diffusion.....95
5.5 Perspectives on experiments that are currently going on in the laboratory.....99
5.6 Significance of measuring axonal Na^+ dynamics using our novel approach.....102

CHAPTER 6. DISCUSSION AND CONCLUSIONS.....104

6.1 Objectives and limitations of high spatial and temporal resolution functional imaging.....105
6.2 Why using a computational approach to unravel native ion channel dynamics.....107
6.3 Towards the full understanding of the action potential.....109
6.4 Conclusions and future perspectives.....111

CHAPTER 7. BIBLIOGRAPHY.....112

Chapter 1. Introduction

The history of neuroscience has so far been linked to the history of its methods (Yuste, 2015). The beginning of electrophysiology is believed to be the invention of the galvanometer by Hans Christian Oersted in 1820 (Oerster, 1820), which was later used by Emil Du Bois-Reymond to show the existence of the membrane potential. Remarkably, he also observed that the membrane potential reversed when an action potential (called nerve impulse back then) passed down the axon (Du Bois-Reymond, 1841-1895). Few years later, in 1868, Julius Bernstein invented the 'differential rheotome' apparatus (a specialized galvanometer) to quantitatively explain the action potential and he was the first to theoretically attribute it's formation to the movement of ions between the interior and exterior of the cell when the membrane 'breaks' (Bernstein, 1902). His theory though awaited experimental confirmation for several years.

The most important breakthroughs though came after 1936, when John Zachary Young introduced the 'giant squid axon' that was large enough to insert normal electrodes and test Bernstein's theory of ions (Boycott, 1998). The introduction of the giant squid axon led the history of neurophysiology in its most influential times with the work of Andrew Huxley and Alan Hodgkin in 1939. They provided the first recording of an intracellular action potential (Hodgkin and Huxley, 1939) and later, using the voltage clamp technique, they published their elegant mathematical equations describing the formation of the action potential (Hodgkin and Huxley, 1952). Both voltage clamp and their equations are used up to date in theoretical models and experiments.

The mathematical analysis of Hodgkin and Huxley had assumed the existence of voltage gated Na^+ and K^+ channels, and even their gating properties. However, over 100 different ion channels have been identified today. Moreover, it has been shown that over a dozen different channels may be present on the membrane of a single neuron in different concentrations depending on the compartment (reviewd in Hille, 2001; Tombola et al., 2006). The specific distribution of ion channels in the neuronal membrane is responsible for neuronal signaling as well as other neuronal functions, while mutations of these channels can lead to several diseases (Catterall et al., 2008). For this reason, the extensive study of the function of different ion channels is a very intriguing field of research and my thesis was focused towards this objective.

In the following sections, starting with the basic principles behind the resting membrane potential and the work of Hodgkin and Huxley on describing active ion channels, I show how the neuron is described mathematically as an electrical circuit. I am then introducing and comparing different techniques for studying ion channels and the farewell in imaging techniques and modeling. In the last section, the general aim of this dissertation is presented.

1.1 Basic principles of the electrical activity in neurons

The physical ground of the membrane potential (V_m) is the difference in ion concentrations in the intracellular and extracellular space separated by the cell membrane and the selective permeability of the membrane for each ion (see Nicholls et al., From Neuron to Brain fifth edition, Sinauer Associates, 2011) . The composition of the neuronal membrane is illustrated in Figure 1.1. The cellular membrane is primarily composed of a 5 nm thick lipid bilayer which is impermeable to water molecules and ions (two lipid layers, whit their hydrophilic ends pointing toward the exoplasm and cytosole and their hydrophobic ends pointing inwards). There is a net difference between ions inside and outside the cell which leads to an electrical field across the membrane, similar to a capacitor.

The lipid bilayer is spanned by pores, the ion channels, which can allow certain ions to flow through the membrane. Active and passive ion channels exist on the membrane. Active channels have open and closed states depending on the V_m, ionic concentrations or the presence of bound ligands, while passive channels do not depend on such parameters. Both channel types exhibit selective permeability to different types of ions in the open state and thus are usually labelled by the ion they are most permeable to. Furthermore, numerous channels with different properties exist for each ion.

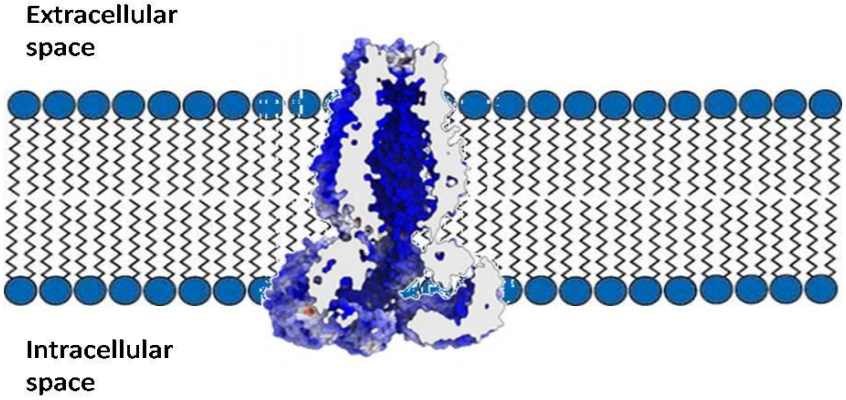

Figure 1.1: *Cellular membrane. The lipid bilayer forms an impermeable barrier for ions. Ion channels span the membrane to allow certain ions to pass through.*

The basis of electrical activity in neurons is the flow of ions through ion channels in the cell membrane. In this section I introduce the simple passive channels and then in the next section active channels are added. Considering only passive channels, the physical principles governing the movement of ions through channels are diffusion and electrical drift. When there are both electric fields and non-uniform ion concentrations, the movement of the ions is described by a combination of these, electrodiffusion.

Electrodiffusion is the origin of the resting V_m. We can consider the cytosol and exoplasm as a container divided into two compartments by the membrane. The cytosol contains a solution consisting of equal numbers of cations K^+ and anions A^- and the exoplasm a lower concentration of the same solution, as shown in the schematic Figure 1.2. If we also assume that the membrane is permeable only to K^+ and not to the anions, only K^+ can diffuse down their concentration gradient. This would create an excess of K^+ on the exoplasm and excess of A^- on the cytosole that would in turn create an electric field, and hence a potential gradient across the membrane causing an electrical drift of cations back across the membrane opposite to their direction of diffusion. The potential difference across the membrane grows until the diffusion and electrical drift become equal and there is no net movement of ions. The system is then at equilibrium and we can measure a stable potential difference across the membrane, the equilibrium potential. The equilibrium potential resulting from the permeability to a single ion is calculated by the Nernst equation (which is derived from integrating the Nernst–Planck equation assuming zero flux):

$$E_X = \frac{RT}{z_X F} ln \frac{[X]_{out}}{[X]_{in}}$$

Where $[X]_{in}$ and $[X]_{out}$ are the intracellular and extracellular concentrations respectively, and E_X is the Nernst potential for that ion. Table 1.1 shows the intracellular and extracellular concentrations of various important ions in a typical neuron and the equilibrium potentials calculated for them. In order to predict the resting V_m of a neuron, a membrane permeable to more than one type of ions must be considered. This was achieved by Goldman, Hodgkin and Katz, who assumed that ions flow through the membrane independently and for the membrane to be in equilibrium, when it is permeable to Na^+, K^+ and Cl^-, the total current flowing through the membrane must be zero. The Goldman– Hodgkin–Katz (GHK) voltage equation for the reversal potential is:

$$E_m = \frac{RT}{F} ln \frac{P_K[K^+]_{out} + P_{Na}[Na^+]_{out} + P_{Cl}[Cl^-]_{in}}{P_K[K^+]_{in} + P_{Na}[Na^+]_{in} + P_{Cl}[Cl^-]_{out}}$$

Where P_K, P_{Na} and P_{Cl}, are the membrane permeabilities to K^+, Na^+ and Cl^- respectively and can include other ions as well, such as Ca^{2+}. The GHK voltage equation is equal to the Nernst equation when the permeability of all ions, except one, is zero. However, GHK voltage equation is not equal to the sum of Nernst equations for different ions.

Table 1.1: *Intracellular and extracellular concentration of ions in a neuron*

Ion	Extracellular concentration (mM)	Intracellular concentration (mM)	Ratio (out:In)	E_{ion} (in mV, at 37°C)
K^+	5	100	1:20	-80
Na^+	150	15	10:1	62
Ca^{2+}	2	0.0002	10000:1	123
Cl^-	150	13	12:1	-65

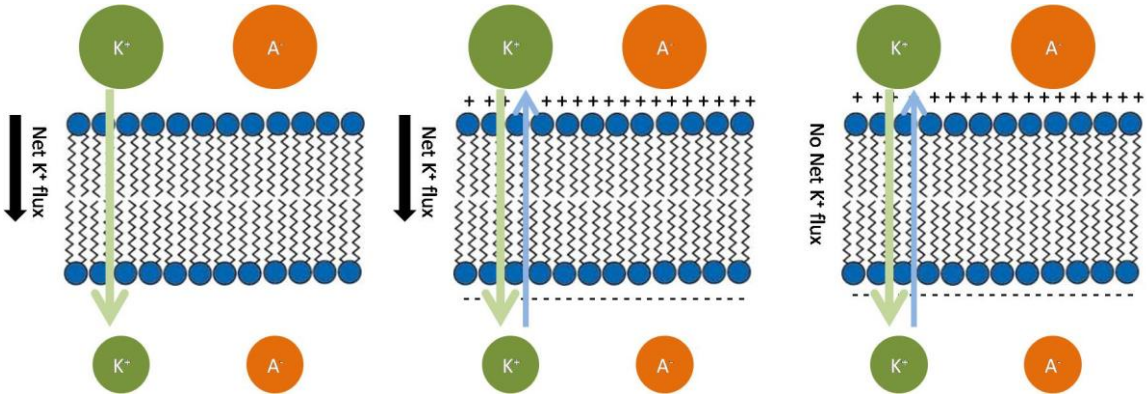

Figure 1.2: *Electrodiffusion. The emergence of a voltage across a semipermeable membrane. The green arrows indicate the net diffusion flux of the potassium ions and the blue arrows the flow due to the induced electric field. (a)Initially, K+ ions begin to move down their concentration gradient (from the more concentrated top side to the bottom side with lower concentration). The anions cannot cross the membrane.(b)This movement creates an electrical potential across the membrane.(c)The potential creates an electric field that opposes the movement of ions down their concentration gradient, so there is no net movement of ions.*

1.2 *Hodgkin-Huxley equations and the action potential*

The history of neurophysiology was introduced into its most influential times with the work of Andrew Huxley and Alan Hodgkin in 1939 that provided the first recording of an intracellular action potential (Hodgkin and Huxley, 1939). With intracellular recordings as shown in Figure 1.3B they could demonstrate that action potentials are characterised by a sharp increase in the V_m (depolarisation) after reaching a distinct threshold, followed by a less sharp decrease towards the resting potential (repolarisation) which may be followed by an afterhyperpolarisation phase in which the V_m falls below the resting potential before recovering gradually to the resting V_m.

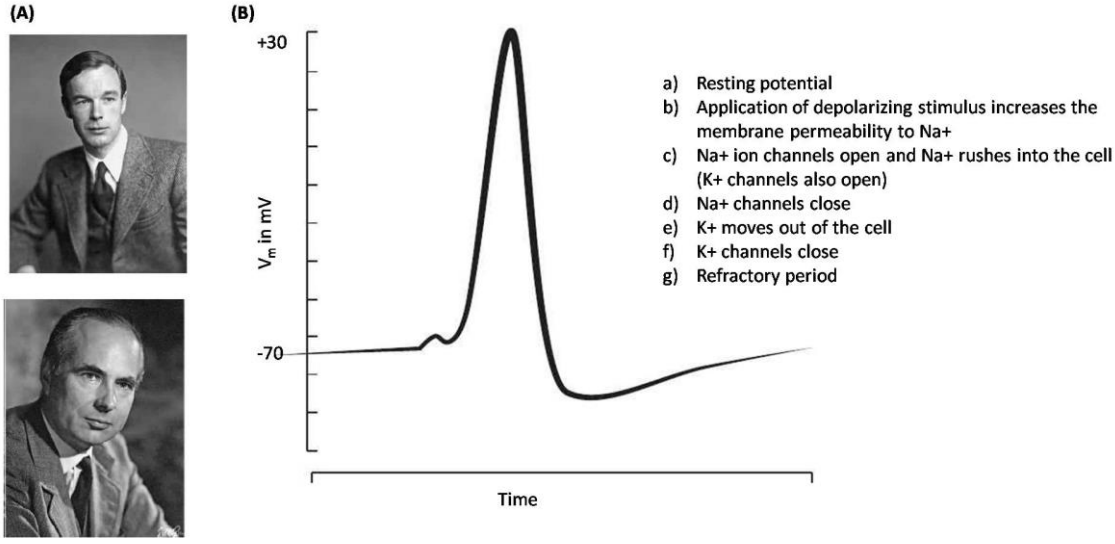

Figure 1.3: *(A) Hodgkin (up) and Huxley (down). (B) A typical account of the action potential recorded by Hodgkin and Huxley. If the resting potential (presented here as –70 mV) is increased to about –55 mV, sodium ions will enter the cell causing the membrane potential to peak at about +50 mV. As this point is reached, the sodium channels close and potassium ions move out of the axon, bringing the membrane potential back to its resting state. Source: Welcome library, London*

Unfortunately, their work was interrupted by World War II and was only continued several years later with the introduction of the Voltage-clamp technique in 1949 by Kenneth Cole. Together with Bernard Katz they used voltage-clamp recordings to investigate the voltage sensitivity and underlying ion channels in the squid giant axon (Hodgkin, Huxley and Katz, 1952). Their work earned them a Nobel prize in 1963. In 1952 they published their elegant mathematical equations describing the formation of the action potential that even predicted gating parameters of ion channels which are used up to date in theoretical models and experimental observations (Hodgkin and Huxley, 1952).

The mathematical analysis of Hodgkin and Huxley (HH) had assumed the existence of voltage gated Na^+ and K^+ conductance but the experimental evidence for the existence of ion channels at the time was not yet available. Their methodology and equations, although they are not made specifically for ion channels, are still used today to describe them mathematically. They predicted that the form of the action potential is associated with the voltage dependent Na^+ and K^+ channels. The depolarization increases the conductance g_{Na} of the voltage dependent Na^+ channels. The threshold is reached when enough Na^+ channels are activated to overcome that of K^+. After the threshold is reached, a sudden increase in g_{Na} depolarizes the cell towards E_{Na}. At this point, the Na^+ channels inactivate and the number of active voltage dependent K^+ channels increases producing a flux of K^+ ions on the opposite direction re-polarizing the membrane. The undershoot appears because the V_m goes towards E_K until the K^+ channels are closed again.

There are three types of ionic current in the cmembrane: a Na^+ current, a K^+ current and a leak current, which is mostly made up of Cl^- ions. The Na^+ and K^+ conductances depend on voltage, meaning that they are active rather than passive channels. The total ionic current is

$$I = I_{Na} + I_K + I_L$$

With the current of each ion being:

$$I_X = g_X(V - E_X)$$

Where E_X is the equilibrium potential; g_X is the conductance per unit area measured in mS/cm^2 and the term $(V- E_X)$ is called driving force. For K^+, they assumed that channels have a number of gates which can be either closed to the passage of all ions or open to the passage of K^+. Each gate has a number of independent gating particles, each of which can be in either open or closed state. K^+ flows through a gate only when all the gating particles are open, which happens with respect to the V_m. The gating variable n is the probability of a single potassium gating particle being in the open state. As the gating particles are assumed to act independently of each other, the probability of the entire gate being open is equal to n^x, where x is the number of gating particles in the gate. The conductance of the membrane is given by the maximum conductance multiplied by this probability.

$$g_K = \overline{g_K} n^x$$

The movement of a gating particle between its closed and open positions can be expressed as a reversible chemical reaction and how the gating variable n changes over time is given as:

$$\frac{dn}{dt} = a_n(1 - n) - \beta_n n$$

The variables α_n and β_n are rate coefficients which depend on V_m. Hodgkin and Huxley found that raising n to the power four was a better match to their experimental data The general form of the time course for n(t) in response to a voltage step is:

$$n(t) = n_\infty(V) - (n_\infty(V) - n_0)e^{(-\frac{t}{\tau_n(V)})}$$

where n_0 is the value of n at the start of the step, defined to be at time zero; the variables $n_\infty(V)$ and $\tau_n(V)$ are related to the rate coefficients $\alpha_n(V)$ and $\beta_n(V)$ by:

$$n_\infty = \frac{a_n}{a_n + \beta_n} \quad and \quad \tau_n = \frac{1}{a_n + \beta_n}$$

where n_∞ describes the limiting probability of a gating particle being open if the V_m is steady as t approaches infinity and τ_n is a time constant.

The same procedure was followed for Na^+ ions but this time they had to introduce an inactivating parameter h similar to the gating parameter n. Their data were fitted satisfactorily by using three independent n gating particles, and one inactivating particle h:

$$g_{Na} = \overline{g_{Na}} n^3 h$$

They also observed a leak, non-sodium current that still flows at the potassium equilibrium potential. They proposed that it was due to a mixture of ions independent on voltage. Both the leakage conductance and equilibrium potential are largely connected to the permeability of the membrane to chloride. To solve the set of these couplet non-linear differential equations Hodgkin and Huxley used numerical integration methods which took them weeks of work on a hand-operated calculator. Today they can be solved in fractions of a second using a

simulation platform such as NEURON. Although the set of the HH equations were constructed to explain the generation and propagation of action potentials specificaly in the squid giant axon, the general idea of gates comprising independent gating particles is used widely to describe other types of channels.

1.3 The neuron as an electrical circuit

The equation for the ionic current, as described in the previous sections:

$$I_X = g_X(V - E_X)$$

shows that channels can be described as resistors of resistance $1/g_X$. Previously the membrane was also described as a capacitance, thus the permeable and impermeable properties of the membrane can be described as electrical properties that form an electrical circuit as shown in Figure 1.4A.

This electrical circuit can be further simplified as shown in Figure 1.4B by including all channels in one, whith a specific membrane resistance R_m, measured in Ωcm^2, and a membrane battery with an electromotive force of E_m. The ohmic equivalent of the GHK voltage equation for two channels X and Y, becomes:

$$E_m = \frac{g_X E_X + g_Y E_Y}{g_X + g_Y}$$

$$\frac{1}{R_m} = g_m = g_X + g_Y$$

This simplified circuit is well known as the RC circuit and the V-I relationship can be derived using Kirchoff's current law:

$$C_m \frac{dV}{dt} = \frac{E_m - V}{R_m} + \frac{I_e}{a}$$

Where α is the area of the studied membrane. This equation shows that at every moment, the rate of change of the V_m is related to the V_m itself and the current injected.

This RC circuit is a good approximation for small membrane regions that can be considered isopotential since axial current flows along neuronal compartments. To extend the model, the neuronal compartment is split up into smaller cylindrical compartments. Each compartment has a length l and a diameter d, with surface area α =πdl and is described by the RC circuit. Additionally, current can flow longitudinally through the subcompartments. We can model the extracellular medium as an isopotential electrical ground. The V-I relationship will now be expressed by the equation:

$$C_m \frac{dV_i}{dt} = \frac{E_m - V_i}{R_m} + \left(\frac{V_{i+1} - V_i}{l^2} + \frac{V_{i-1} - V_i}{l^2}\right) + \frac{I_{e,i}}{\pi dl}$$

This equation can be solved numerically using simulation packages such as NEURON, or with the cable equation proposed by Wilfrid Rall, one of the founders of computational neuroscience (Rall, 1957).

The cable equation allows the spatiotemporal evolution of the V_m to be solved analytically:

$$C_m \frac{\partial V}{\partial t} = \frac{E_m - V}{R_m} + \frac{d}{4R_a}\frac{\partial^2 V}{\partial x^2} + \frac{I_{e,i}}{\pi dl}$$

In this equation the V_m is a function of distance x along a continuous cable. The cable equation is very similar to the equation of a single compartment, except for the partial derivative $\partial V/\partial t$ and the extra term $\frac{d}{4R_a}\frac{\partial^2 V}{\partial x^2}$ which is the net density of current flowing along the length of the cable into point x.The above equations describe the so known passive model of neurons and although they are a very simplified description of real neuronal behavior, they can provide useful information such as the membrane resistance.

A more realistic model should include active properties, such as the HH model described in the previous section. The starting point of the HH model is the equivalent electrical circuit of a compartment shown in Figure 1.4. The key difference between this circuit and the RC is that the Na^+ and K^+ conductances depend on voltage, meaning that they are active rather than passive channels. The equation corresponding to that circuit is

$$I = I_c + I_i = C_m \frac{dV}{dt} + I_i$$

Where I is the membrane current, I_c is the capacitive current and I_i is the total ionic current which is the sum $I_i = I_{Na} + I_K + I_L$, whith $I_X = g_X \cdot (V - E_X)$.

As previously mentioned, the solution of such equations would take weeks to solve on hand. Thanks to the advancements in computer technology and the available simulation packages, these equations can be now solved in fractions of seconds. Modeling of neurons has been a technique widely used in the past century to describe the behavior of neurons and several models of ion channels have been developed to that purpose (McDougal et al., 2017). The inverse, extracting channel models by modeling neuronal signals, is a less exploited technique and is the approach followed in this thesis. In combination with experimental techniques, computational models can be used to extract channel kinetics. Depending on one's questions, different experimental techniques can be followed to extract channel kinetics. In the next section I describe some of these techniques comparing their advantages and disadvantages.

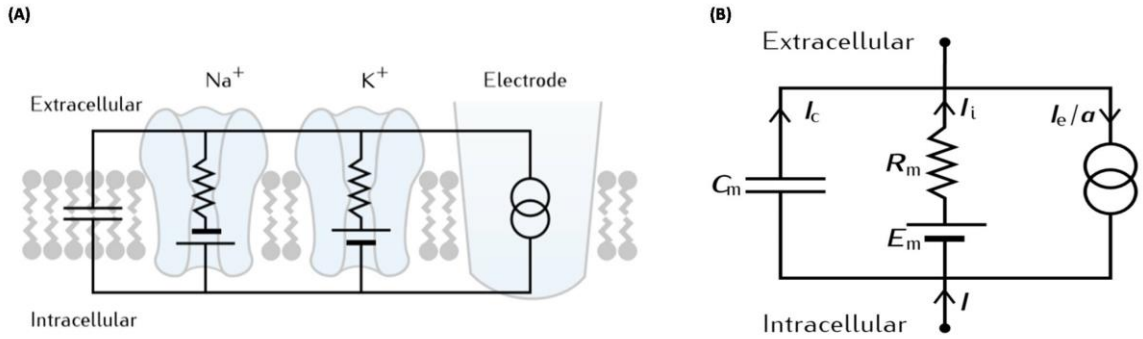

Figure 1.4: *The membrane as an electrical circuit.* ***(A)*** *The equivalent electrical circuit of patch of membrane. (B) The equivqlent reduced circuit. Source: Sterratt et al., 2011*

1.4 Techniques to extract channel kinetics

Since the work of Hodgkin and Huxley, a wide range of techniques have been developed to study the structure and function of ion channels. Among the most popular techniques are patch-clamp and functional imaging. In addition to either technique, blockers of specific ion channels, mutated animals and/or computational modeling can be used. In this section I give a brief description of the two techniques, either alone or in combination with any of the three additional procedures.

The patch-clamp technique: While Hodgkin and Huxley were using two sharp electrodes impaling the same cell, one to hold the V_m and the other to inject the current, this approach was replaced later by the patch clamp technique (Sakmann and Neher, 1984) invented by Bert Sakmann and Erwin Neher who won the Nobel Prize for medicine and physiology in 1991. This technique relies on the use of a fine tipped glass capillary to make contact with a patch of a cell membrane in order to form a giga-ohm seal. This technique has many variants that allow the application of solution on the exterior and interior of whole cells and on membrane patches detached from the cell (outside-out or inside-out).

Single channel recording can be performed with the outside-out or inside-out configuration, as first shown in 1976 by Erwin Neher and Bert Sakmann, who taking advantage of the micropipette development, managed to isolate a tiny part of the membrane and measure currents from single-ion channels (Neher and Sakmann, 1976). This technique has been widely used to study channel kinetics and has been the source of several computational models of ion channels (Nilius et al. 1985; Clay et al., 1983; Linaro et al., 2011). The disadvantage of this technique is that it is highly invasive, does not give any spatial information and does not allow the investigation of the ion channels within their physiological environement, which is essential at understanding how neurons work.

Whole-cell patch clamp on the other hand is widely used to measure V_m (in current clamp mode) or current (in Voltage clamp mode). The disadvantage of the voltage clamp mode, is that it measures currents coming even from remote regions that are unclamped (Williams and Mitchell, 2008). In addition to summing currents from different sites, the recording sites are also limited (Stuart and Sprutston, 1995), thus, carrying little information about the originating site of the current. This technique is also highly invasive and can distort the distribution of channels (Kole et al., 2008). Finally, we cannot measure the current coming from a specific type of channel and thus to get such information we have to combine it with at least one of the procedures.

In contrast to the patch-clamp technique, optical recordings using fluorescent indicators specific for an ion, the recording conditions remain physiological, are specific to the site that is imaged and multiple sites can be recorded simultaneously. Simultaneous recording of multiple currents or V_m at the same time is also possible using multiple dyes (Jaafari et al, 2015). The disdvantage of this technique is that the recording are limited by light diffraction that compromise the signal to noise ratio (SNR). Optical techniques also do not measure the current coming from a specific channel subtype and thus have to be combined with a procedure to extract channel kinetics.

Using control and knock out animals that do not express a specific channel, currents can be compared for the two conditions. This technique though may have several disadvantages with most crucial being the fact that the recordings are not made under the same conditions. Another disadvantage is that some mutations are lethal (Ye et al., 2018).

Channel isolation using specific ion blockers on the other hand allows to record from the same cell and site before and after the inhibition of the channel. The first blocker to be discovered was tetrodotoxin (TTX), a Na^+ blocker extracted by the Japanese puffer fish (Narahashi et al., 1964). The disdvantages of this technique is that by blocking these channels we distort the physiological conditions, complete block of the channel subtype is usually not achieved, the targeting of only a specific channel subtype is not possible (a percentage of other channels is affected as well) and finally toxins for some channels are not available yet.

To overcome the limitations of the two above procedures, they can be combined with computational modeling, as described in chapter 4. Computational models can be built to reconstruct the optical recordings and pharmacological tests can be used as supporting information. This method became possible only recently thanks to the remarkable advance in indicators, detection devices, light sources and computer technology (Davies et al., 2013), described in the next section.

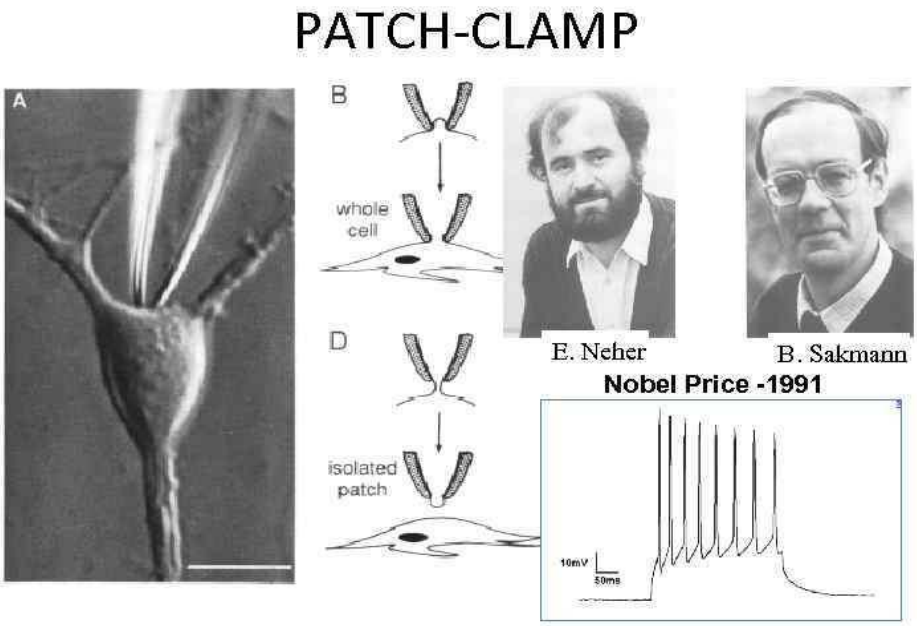

Figure 1.5: *The patch-clamp technique by Sakmann and Neher*. Source: INTRODUCTION TO NORMAL PHYSIOLOGY. CELL PHYSIOLOGY Lecture 1 2014 Irina Vasilyevna Mukhina

1.5 State of the art

1.5.1 Indicators

'Seeing is believing' is probably one of the most used and on-the-point quotes in current physiology, in particular when applying this statement to neuroscience (Stenmark, 2009; McGeown, 2010). Although microscopes existed since the 16th century and were used in biology for observations, dynamic (or functional) imaging became available much more recently. This was highly due to the introduction of fluorescence (light emission from a material at different wavelength from that absorbed), observed initially by Stokes, who created this definition after fluorite (Stokes, 1850). The physical properties of fluorescence were explained later by A. Jablonski (Jablonski, 1935). In brief, he explained that when the fluorophore absorbs the energy of an electromagnetic wave, its electrons are moved to an excited state. After a few nanoseconds they return to their relaxing state emitting a photon of lower energy due to loss of energy in form of vibration, the so called Stokes shift (Figure 1.6). There are several wavelengths that can be absorbed and thus emitted, resulting in the wide excitation and emission spectra of the fluorophores.

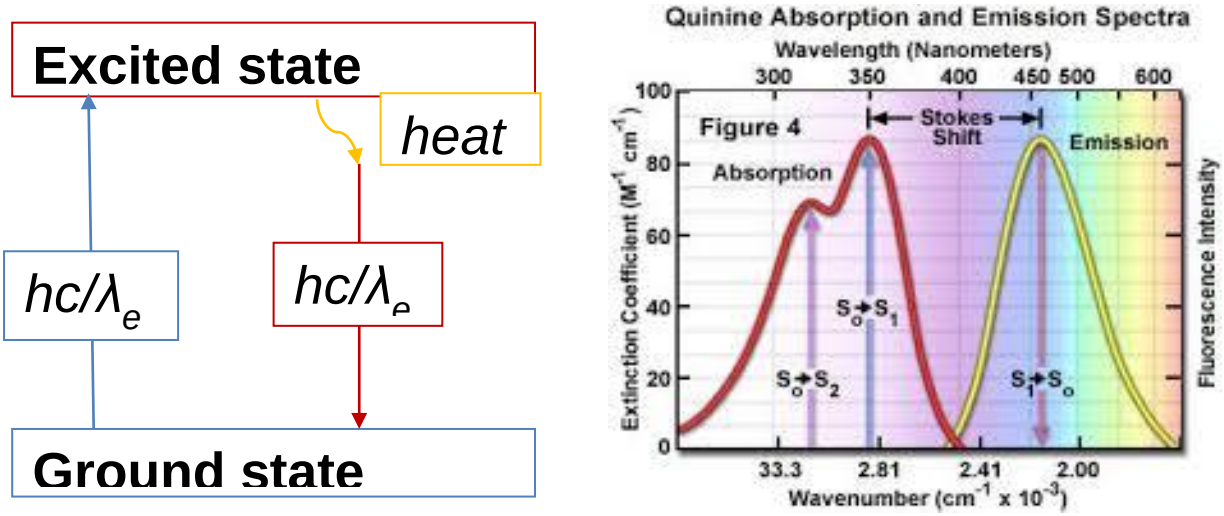

Figure 1.6: *The absorption and emission of light during fluorescence. (left) After excitation by light absorption, the electron moves to an excited state of lower energy (blue arrow). When it drops to the ground state (red arrow) light is emitted. (right) Absorption and emission spectra. (source:Imaging Neurons: A Laboratory Manual by Rafael Yuste, Frederick Lanni, and Arthur Konnerth Cold Spring Harbor Laboratory Press).*

The introduction of fluorescent probes for V_m and Ca^{2+}, came mainly from the work of Lawrence B Cohen for voltage sensitive dyes (Cohen et al., 1978) and of Roger Y. Tsien for

Ca^{2+} indicators (Grynkiewicz et al.,1985). Influx of Ca^{2+} during electrical activity can create up to a 100 fold increase in its concentration which is much higher than most other ions, favoring Ca^{2+} imaging. Intracellular imaging of Na^{+} was first introduced by RY Tsien (Minta and Tsien, 1989) with the developement of the Na^{+} indicator benzofuran isophthalane (SBFI).

Fluorphores are highly used in neuroscience to address several questions and as more sensitive dyes are being introduced in the market, more sensitive imaging technologies are being developed as well.

1.5.2 Imaging techniques

The expansion of imaging techniques has been for decades limited by the available technology in terms of detection devices, illumination sources, but also by the informatics since acquired data must be digitised to be quantitatively analysed and stocked in sufficiently large devices to contain large amount of information. From the point of view of detection devices, the replacement of single-site detectors (for instance photodiodes) with arrays of detectors (i.e. cameras) allowed monitoring multiple sites simultaneously, a task which is pivotal both in the analysis of single cells and in that of neural networks. Dramatic advances in the accuracy of fluorescent microscopy have occurred therefore with the improvement of the cameras used. In particular, since the development of *charged coupled devices* (CCD) by M.F. Tompsett, the introduction in neuroscience of low-noise CCDs, obtained by lowering the temperature of the chip, opened new prospective for the exploitation of imaging techniques developed in parallel (Connor, 1986).

Today, the choice of a device with specific characteristics ideal for a type of measurement includes CCD, EMCCD and sCMOS cameras (Davies et al., 2013). This choice is based on the requirements in terms of spatiotemporal resolution, sensitivity, field of view, size of the signal to measure and number of photons available in the measurements. These requirements translate in the characteristics of the camera.

In particular, any light measurement is limited by the intrinsic photon noise that depends on the quantal nature of the light and not on the device, which is set by the fact that a measurement of N photons is affected by fluctuations of $\sqrt{N}$. It means for instance that in a measurement of 10^4 photons, the detection of a 10^2 photons signal (corresponding to 1% change of light intensity) will be barely detectable, whereas at this level only light changes over 3% can be reliably measured. Hence, an ideal device should measure a signal being

limited by the intrinsic noise, i.e. under the condition in which the noise of the device, namely the *readout noise*, is negligible with respect to the photon noise.

The important parameters of a device, from this point of view, are the *well depth* (i.e. the number of photons that saturate the device) and the *dynamic range* (i.e. the minimal fraction of the well capacity that can be measured above the readout noise). Other important parameters are the acquisition speed and the number of pixels, (the two parameters are correlated), that ultimately set the spatiotemporal resolution of the device.

The three main families of available cameras are briefly described below (reviewed in Davies et al., 2013).

- CCD (Charged Coupled Device)

  There are several families of commercially available CCDs that vary in terms of resolution and well depth. Fast CCD cameras are typically limited in terms of spatial resolution which is ultimately set by the analogue-to-digital conversion, but these cameras can reach a very high acquisition rate up to tenths of KHz. They have been used for Ca^{2+} as well as voltage imaging on single cells because with a low well depth the readout noise is low. Finally, the probably of converting a photon into a conducting electron, namely the *quantal efficiency* (QE), can be very high (>90 %) in the 500-700 nm spectral range thanks to the technique of "back-illuminating" the device.

- EMCCD (Electron Multiplying Charge Coupled Device)

  When measuring relatively low levels of light, the readout noise might be comparable with the photon noise and simple amplification of the CCD current does not solve the problem. In the past, intensified cameras were used to amplify light prior to detection, but this approach is heavy and, mostly, inefficient. EMCCD cameras are capable to amplify the signal at the level of photon-electron conversion, by multiplying the electrons. Briefly, impact ionization makes this camera capable of single photon sensitivity and a good solution for low light experiments such as single molecule imaging. While at high light levels the readout noise is less important than the photon noise, at low-light level EM amplification can amplify only the latter reproducing the conditions of high light level. Today, improvements in this area have made possible to have devices that can behave both as standard CCDs or EMCCDs according to the setting of the amplification, in this way being used for both high and low level light recordings.

- sCMOS (Scientific Complementary Metal Oxide Semiconductor)

These cameras represent an improvement with respect to CCDs in terms of spatial and temporal resolution. They can have 4-5 megapixel sensors, variable pixel size and consequent well depth, and better temporal resolution (up to hundreds of kHz) with low read out noise (~1e^-). They are therefore ideal for single cell recordings. Improvements are still going on in terms of QE and flexibility for amplification and binning, making these devices potentially always superior for all types of applications.

In addition to the device problem of light detection, the spatial (and temporal) resolutions in fluorescence imaging depend on the type of microscopy implemented. The most basic way of illuminating an object is to excite fluorescence over the entire field of view (wide field microscopy). The major disadvantage of the wide field approach is the limited spatial resolution. The exact location of the fluorescence source is not possible because of the scattered light coming from all other directions. In brain slices, the cell is usually not on the surface but several microns below and thus the surrounding tissue scatters the light reducing the resolution.

From this illumination strategy, improvements can be obtained by using light spots shaping the light using holography (Papagiakoumou, 2013) or a Digital Micromiror Device (DMD, Szabo et al., 2014). Further improvements, also in terms of tissue penetration can be obtained using two-photon excitation, an approach that can ne also combined with holography to result in efficient multisite illumination (Dal Maschio et al., 2010).

Another (and also more traditional) strategy to improve the spatial resolution is confocal microscopy (Fine et al., 1988). The first confocal system was introduced by Marvin Minsky in 1955. The basic principle is the use of a pinhole to reject out of focus light. Unlike wide field imaging, only a single spot can be recorded each time and to build the complete image one has to scan the sample. In conventional confocal microscopy the acquisition rate and the number of scanned points are inversely proportional compromising either the field of view or the temporal resolution. When imaging ion signals both are necessary since it is important to measure several sites simultaneously with a temporal resolution in the ms region at least.

To overcome this limitation the Nipkov -spinning- disk was introduced. This system uses a set of pinholes on a disk that covers a wide filed region and rotates rapidly to eliminate scattered light from multiple points simultaneously. The disadvantage of this system is that a big portion of the light is eliminated and even with a great intensity light source, the signal to noise ratio (SNR) is compromised (Coates et al. 2004). Compared to other techniques, some

of its advantages are that more light is collected resulting in better SNR while lower intensities are needed resulting in less photodamage. Furthermore, depending on the detection system used, image acquisition can be very fast (tenths of kHz) (Sanderson et al., 2014).

1.5.3 Light sources

The advances in illumination systems have also played a role in the improvement of imaging techniques (reviewed in Davies et al. 2013; Spring and Davidson, MicroscopyU; Bushwick 2012). To achieve a bright image but at the same time reduce the photodamage, the excitation light must be of high intensity and contain only the necessary wavelengths corresponding to the excitation spectrum of the specific fluorophore. Over the years several light sources have been used and as the technology advances we get sources of higher intensity and narrower spectrum.

Among the first light sources used in microscopy, one can mention the gas discharge lamp, aka arc or burner lamp. Mercury burner has the disadvantage that it has a wide wavelength range but the intensity is high only at specific wavelengths near the UV and specific visible wavelengths. On the other hand the Xenon burner has a nearly uniform spectrum, slightly higher in intensity towards the IR, but most of the power of the lamp is lost in heat. Filters can be used to select the desired wavelengths, but the shorter is the band of the filter the less is the power of the illumination. Another disadvantage is the time required to reach stability, i.e. they don't reach their stable intensity fast enough and therefore the exposure time must be externally controlled by mechanical shutters.

Significant improvements came with the introduction of LEDs (light-emitting diodes) which offer a narrow range of wavelengths and several other advantages over the arc lamps, such as the longer lifetime and the instant switch on/off. The intensity of the LED has increased through the years making it widely used in wide-field fluorescence microscopy.

Finally, lasers are now becoming the most used light sources. Lasers provide high intensity monochromatic light which being collimated can also be easily manipulated with negligible power loss and eventually focused on narrow fields instead of illuminating the whole sample reducing the photodamage and also the out of focus light. Their spread is also boosted by the very recent dramatic drop of price, in particular for stable diode lasers like the one used in my experiments.

1.5.4 The NEURON simulating platform

The biophysical principles introduced at the beginning of this chapter make it clear that the theoretical concepts underlying neurons, namely the passive cable theory and the HH equation must be combined to describe realistically the neuronal activity. As the problem is too complex to be addressed with an analytical approach, computer simulations become necessary to achieve this important step. This idea animated the work of John W Moore and his colleagues who in the eighties developed the software named "NEURON" (Moore, 2010). NEURON modelling (Hines and Carnevale, 1997) is based on combining the passive compartmental modelling introduced by Wilfrid Rall with the active dynamic system accounting for ion conductance introduced by Alan Hodgkin and Andrew Huxley.

After the introduction of NEURON, the database ModelDB, founded in 1996, has grown to include over 1100 published models covering more than 130 research topics (McDougal et al., 2017). The NEURON modelling environment and ModelDB database are ideal instruments for large-scale projects involving many research groups, such as the European flagship *Human Brain Project* (Amunts et al., 2016).

In this type of projects, where the goal is to reconstruct a large-scale neuronal network from the molecular and small compartment information, a NEURON simulation is used as predictive tool. However, NEURON can be used in the opposite sense, to produce simulations *matching* detailed small experimental scenarios with the goal of reconstructing the physiological function and dysfunction of individual molecules (i.e. the channels), as done in chapter 4 of this thesis.

1.6 General aim of this dissertation

To summarise what I introduced in this chapter, neurosciences are today advancing experimentally with optical techniques, and theoretically by more and more detailed modelling, requiring powerful computational technologies but also groundbreaking concepts to exploit the amount of information available. The ability to merge together the experimental and the theoretical pathways is obviously a potential strategy to go beyond our present knowledge. The possibility to carry out a PhD project that enabled me to acquire skills both in imaging techniques and computational neuroscience was therefore very intriguing. Specifically, the problem that my laboratory is addressing is that of how native ion channels

behave during physiological activity. The general aim of this doctoral dissertation is the detailed study of ion channels involved in neuronal signaling.

We used a multidisciplinary experimental approach including cutting edge imaging techniques, pharmacological studies and computational models in order to focus on the unique kinetics of the ion channels in different systems. Our specific aims were:

- To develop a confocal system able to overcome patch-clamp and wide field imaging limitations in resolving Ca^{2+} signals from multiple sites simultaneously with a high spatial and temporal resolution.
- To extract the channel kinetics of multiple channels working in synergy to produce the signals recorded with fluorescence imaging. To that cause, fluorescent imaging and toxins were used to develop a computational model that reproduces the observed signals.
- To develop a methodology for extracting Na^{+} current kinetics using Na^{+} imaging.

Taken together, the three different pieces of work performed in these three years are aimed at being put together in the near future to progress in the understanding of how ion channels really function and how a dysfunction can be the cause of human diseases.

Chapter 2. Materials and Methods

A significant part of my thesis work consisted in developing novel methods and techniques. Most of this work is described in the following chapters and included in the Results. The original assembly of the optical parts is described here in sections 2.4 and 2.5. The rest of this chapter describes the standard methods used in the laboratory.

2.1 Animals

Mice aged 21-35 postnatal days (C57Bl6 strain) used in the experiments of my thesis, were purchased from Janvier (https://www.janvier-labs.com/), and housed in the animal facility of the University campus in Saint Martin d'Héres. All procedures were carried out in accordance with European Directives 2010/63/UE on the care, welfare and treatment of animals. Procedures were reviewed and approved by the ethics committee affiliated to the animal facility of the university (D3842110001).

2.2 Slice preparation, solutions and electrophysiology

1. 800 ml of artificial cerebrospinal fluid (ACSF) was prepared. This solution contained (in mM): 125 NaCl, 26 $NaHCO_3$, 1 $MgSO_4$, 3 KCl, 1 NaH_2PO_4, 2 $CaCl_2$ and 20 glucose.
2. 200 ml of extracellular solution for slicing was prepared, containing (in mM): 125 NaCl, 26 $NaHCO_3$, 2.5 $MgSO_4$, 3 KCl, 1 NaH_2PO_4, 0.5 $CaCl_2$ and 20 glucose.
3. The slicing solution of step 2 was maintained at -20 °C for about 2 hours, to be used for dissection and for cutting in the slicing chamber. After freezing, the formed ice was crushed and the solution was bubbled with 95% 0_2 and 5% CO_2 (carbogen) for at least 20 minutes before slicing.
4. About 200 ml of ACSF of step 1 was kept in a glass rod with a handmade slice holder. The glass rod was maintained in a 37 °C water bath and bubbled with carbogen at least 20 minutes before slicing. Any air bubbles under the slice holder were removed using a pipette. The glass rod was covered with a lid to avoid evaporation.

5. All solutions were continuously bubbled with carbogen.
6. The mouse was anesthetized with isoflurane and decapitated following the approved procedures.
7. The skin and skull were cut with scissors and removed with forceps, exposing the brain. The brain was gently removed using a spatula and transferred to the ice-cold solution of step 3 for a few minutes.
8. In the meantime liquid glue was placed on a tissue holder of the Vibrotome.
9. The brain was then transferred to a filter paper and the selected region was dissected out from the rest of the brain.
10. Three different cell types from different brain areas where used in the experiments during my thesis: Purkinje neurons (PN), CA1 hippocampal pyramidal neurons and Layer5 (L5) neocortical pyramidal neurons.
11. All slices were prepared with a Leica vibrotome VT1200 (Leica, Wetzlar, Germany).
12. For PN experiments, the Cerebellum was first separated from the rest of the brain with a razor blade. The meninges were removed and, with the help of a spatula, the cerebellum was placed on an agarose cube to be sliced along the sagittal plane. Prior to slicing, the agarose-tissue was glued on a flat tissue holder of the slicer, placed in the slicing chamber and covered with the ice-cold solution of step 3. Cerebellar sagittal slices with a thinkness of 250 µm were prepared.
13. For the CA1 pyramidal neuron experiments the cerebellum was carefully dissected away and discarded from the rest of the brain. The rest of the brain was directly glued on a flat tissue holder from the side of the midbrain with the posterior side facing the blade. Transversal hippocampal slices (250 µm thick) were cut and the posterior part containing the hippocampus was separated from the rest.
14. For neocortical L5 pyramidal neuron experiments, the cerebellum was carefully dissected away and discarded from the rest of the brain. The two hemispheres where separated with a blade and glued on a custom made tissue holder with a 15 degrees angle. Coronal slices (350 µm thick) were prepared.
15. The slices were transferred to the glass rod filled with the extracellular solution of step 4 and allowed to incubate for 30-45 minutes at 37 °C.
16. The slices were then cooled down to room temperature (22-24 °C) for at least an hour before the experiments.

17. The rest of the ACSF of step 1 was used to continuously perfuse the recording chamber at the rate of ~2 ml/min. The perfusion pathway was heated to keep the temperature in the recording chamber at 32-34 °C.
18. Experiments were done using either a Slicescope microscope (Scientifica UK, chapters 3 and 5) or a BX51 microscope (chapter 4).
19. With the help of a plastic trimmed-tip transfer pipette, a single brain slice was transferred to the recording chamber.
20. The slice was placed in the desired position with the use of forceps and this position was secured with a homemade platinum grid with nylon wires.
21. After focusing on the slice surface with an Olympus 60X objective (water immersion, NA = 1, WD = 2 mm), a healthy cell was selected to be patched. Unhealthy cells are easily identifiable because they are either swelled, their nucleus is clearly visible or they shrink and show high contrast with respect to the gray matter around them. On the other hand, healthy cells are more symmetrical, their nucleus is difficult to see and the contrast with surrounding tissue is lower (see example in Figure 2.1A).
22. Borosilicate glass pipettes (OD = 1.5 mm, ID = 1.1 mm, Harvard Apparatus) were obtained using a DMZ puller (Martinsried, Germany) and had a pipette resistance range of 3.0-4.0 MΩ when filled with the internal solution.
23. To avoid spillage of the dye, the tip of the pipette was front-filled with dye-free intracellular solution containing in mM: 125 $KMeSO_4$, 5 KCl, 8 $MgSO_4$, 5 Na_2-ATP, 0.3 Tris-GTP, 12 Tris-Phosphocreatine, 20 HEPES, adjusted to pH 7.35 with KOH. The internal solution was prepared in stocks of 50 mL, quoted in vials of 1 mL and kept frozen before use to prevent ATP/GTP degradation.
24. Using a syringe and microfiller, the pipette was backfilled with the intracellular solution containing one or two dyes, according to the experiment.
25. The indicators used in my experiments were Oregon Green BAPTA-5N (OG5N, used at 2 mM concentration) or FuraFF (used at 1 mM concentration) for Ca^{2+} imaging, the Voltage sensitive dye JPW1114 (used at 1 mM concentration) for membrane potential imaging and Asante Natrium Green-2 (ANG-2, used at 0.5 mM concentration) for Na^+ imaging.
26. Before ACSF-immersion, we applied ~20 mbar positive pressure to the pipette to prevent leakage of any dyes from the pipettes.

27. The microscope used in the experiments described in chapters 3 and 5 was equipped with two PatchStar manipulators and a fully adjustable stage to put the recording cell in position and to quickly guide the pipettes.
28. When the patch pipette reached the surface of the slice, we applied a stronger positive pressure of ~100 mbar and, while holding that pressure, we quickly approached the surface of the cell. When the pipette touched the cell, we released the pressure to form a seal in Voltage-Clamp mode and set the voltage at the "measured" value of –60 mV before establishing the whole cell patch. The junction potential was compensated before establishing the seal.
29. We then applied a brief and strong suction to rupture the plasma membrane and achieve a successful whole-cell configuration (Figure 2.1A).
30. After establishing a whole-cell patch, we waited 20-40 minutes for the dye to equilibrate through the cytosol in the recording area.
31. Only in the case of the voltage imaging experiments, for which the voltage sensitive dye diffuses through the membrane, after ~30 minutes we detached the pipette by forming an outside-out patch and repatched the cell with a pipette without the voltage sensitive dye as described in previous publications from the laboratory (Canepari et al., 2007; Canepari et al., 2008).
32. Patch clamp recordings were made with a Multiclamp amplifier 700A (Molecular Devices, Sunnyvale, California) and signals were acquired at 20 kHz using a USB-6221 board (National Instruments, Austin, Texas) in the experiments described in chapters 3 and 5. The measured V_m was corrected for junction potential of -11 mV (Canepari et al., 2010).
33. In the experiments on cerebellar Purkinje Neurons of Chapter 3, either climbing fiber (CF) or parallel fiber (PF) excitatory postsynaptic potentials (EPSP) were elicited by current pulses of 5 to 20 µA amplitude and 100 µs duration delivered by a pipette filled with extracellular solution and placed near the soma to stimulate the CF input or near a dendrite to stimulate the PF input.
34. In experiments in CA1 hippocampal pyramidal neurons in Chapter 3, action potentials were elicited by 2 ms current pulses through the patch pipette.

2.3 Pharmacology

Local block of the various Na^+ channels in Chapter 5 was achieved by gentle pressure application of the extracellular solution containing the specific blocker at selective effective concentration, using a pipette of ~2 µm diameter placed next to the AIS as illustrated in Figure 2.1B. Full names, concentrations and properties of chemicals used to block Nav1.2, Nav1.6 or both were as follows:

Huwentoxin IV (HwTx-IV) was purchased from Smartox Biotechnology (Saint Egreve,France) and was used in 2.5 µM concentration. This toxin is isolated from the Chinese bird spider (Haplopelma schmidti) to selectively inhibit tetrodotoxin-sensitive Voltage Gated Na^+ channels (Minassian NA et al.2013).

4.9-Anhydrotetrodotoxin (4,9-Anhydro-TTX, ab146201) was purchased from Alomone Labs (Jerusalem, Israel) and was used in 1 µM concentration. This toxin is used to block Nav1.6 Voltage Gated Na^+ channels thanks to its grater potency over other TTX-sensitive subunits (Rosker et al.2007).

Phrixitoxin-3 (PaurTx3) was purchased from Smartox Biotechnology (Saint Egreve,France) and was used in 1 µM concentration. This toxin is isolated from the tarantula spider (Phrixotrichus auratus) to selectively inhibit Nav1.2 Voltage Gated Na^+ channels (Bosmans et al.,2006).

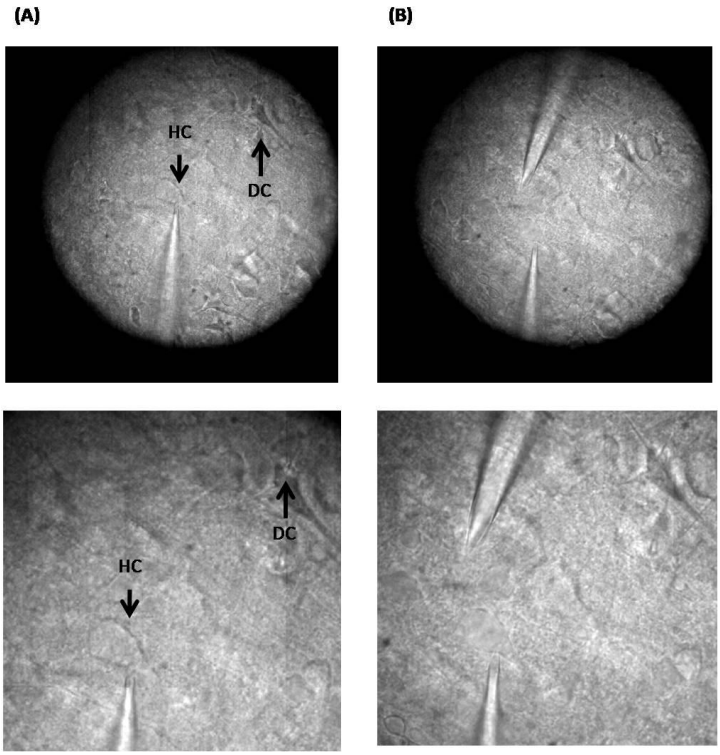

Figure 2.1: *Image of a Layer5 region of a cortical slice with the transmitted light. (A) A selected healthy Layer5 neocortical pyramidal cell (HC) is patched. A dead cell (DC) is indicated. Distinguishing between a healthy and a dead cell is easy as dead cells are no longer symmetrical and have bigger contrast. (B) The pipette for the drug application is placed next to the axon of the patched neuron.*

2.4 Experimental setup for confocal Ca^{2+} imaging (experiments in Chapter 3)

The system was mounted on a SliceScope microscope (Scientifica, Uckfield, UK) equipped with a motorized XY translation stage, PatchStar manipulators and a 60X Olympus water immersion objective (NA =1). The motorized Z translation allowed estimating, with micron precision, the depth of the recording plane from the slice surface. The system, illustrated in the scheme of Figure 2.2A included a spinning disk unit and a novel CMOS camera.

2.4.1 Spinning disk

The spinning disk was a customized version of the X-Light developed by CrestOptics Spa (Rome, Italy). This utilizes a proprietary spinning disk design containing multiple sets of continuous spirals with the following structure: (a) 36 spirals; (b) spiral thickness of 90 µm; (c) spiral step of 16.2 mm; (d) spiral-to-spiral radial distance of 450 µm. The disk was placed in the primary image plane of the microscope (on the trinocular port). The excitation spiral pattern was projected to the sample to scan the entire field of view 36 times per disk revolution, thereby creating a full image of the focal plane in real time with no striping effect. The modified disk unit was spun at 20,000 rpm (333,33 revolution per second). Using an even excitation field, the sample conjugated plane was formed every 83.3 µs. Finally, the spinning disk was automated to move in and out of the light path to enable both confocal and widefield fluorescence imaging in the same experiment.

2.4.2 CMOS camera

The CMOS camera was a DaVinci-2K (SciMeasure, Decatur, GA) using a low-noise 2k X 2k pixel CMOS sensor with traditional readout architecture and true on-chip binning. The flexible sensor and camera design allowed low read-noise performance (<2.8e-) using either correlated double sampling (CDS) or non-destructive read (NDR) to subtract the reset voltage. The large pixel size of 15 µm x 15 µm offered a relatively high fill factor and hence a native Quantum Efficiency (QE) of 65% without using micro lenses. A single 14-bit A/D per readout channel was used to achieve high bit depth without the dual amplifier stitching required in CMOS cameras. Sixteen parallel readout channels were implemented to achieve

high frame rate without compromising the low read-noise. This was the first use of this novel camera in CDS mode for high-speed, live cell imaging. An alternative configuration has been used for stochastic super resolution of fixed samples in non-destructive read (NDR) mode (Barnett, 2017). Within the present configuration, each pixel was mapped to collect light from a square of ~250 nm side. The data was acquired using Turbo-SM written in C by RedShirtImaging (Decatur, GA).

2.4.3 Illumination

The system was equipped with a Tri-Line Laser-Bank (Cairn Research) through a Ø550 µm, 0.22 NA, SMA-SMA Fiber Patch Cable (Thorlabs, Newton, NJ). The laser head used was a multimode diode 465nm / 1.2W (Ushio) illuminating a ~60 µm region as illustrated in Figure 2.2B-C. The microscope also incorporated an OptoLED unit (Cairn Research, Faversham, UK) mounted on the Olympus epifluorescence unit to provide wide-field illumination at 470 nm independent of the spinning disk.

2.4.4 Filters

Different emission and excitation filters, all manufactured by Semrock (Rochester, NY), were used for the different described indicators. Fluorescence excitation light in the Ca^{2+} imaging experiments described in Chapter 3, either from the laser or the LED, was band-passed filtered at 469 ± 17 nm and reflected towards the objective by a 495 nm dichroic mirror. Emitted OG5N fluorescence was filtered at 525 ± 25 nm before detection.

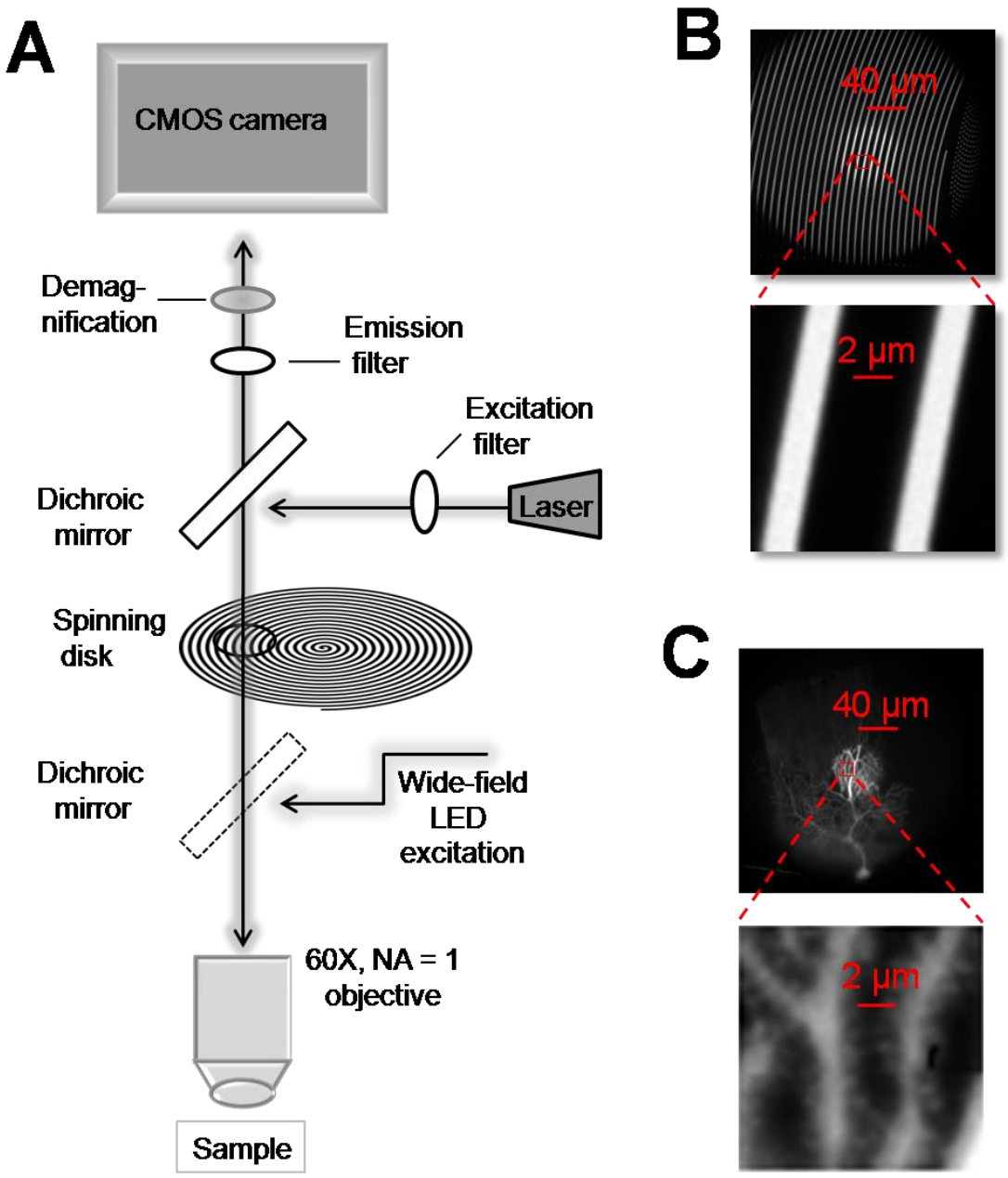

Figure 2.2: *Description of the confocal system. (**A**) Schematic showing the fast spiral pattern spinning disk, coupled to a 465 nm multimode laser and a fast CMOS camera. The configuration includes widefield LED illumination at 470 nm independent of the spinning disk. (**B**) Top: image of the disk obtained using a uniform fluorescence slide with the 60X objective. A frame obtained with whole-field LED illumination is superimposed to a frame with ~60 µm laser spot. Bottom: enlargement of the red square region on the top to appreciate the fine structure of the disk. (**C**) Top: image of a PN filled with OG5N showing the detailed confocal region acquired with laser and spinning disk superimposed over a full frame taken with widefield LED illumination.Bottom: enlargement of the red square region on the top to appreciate the resolution of dendrites and synaptic spines.*

2.5 Experimental setup for high speed Na^{2+} imaging (experiments in Chapter 5)

The system was mounted on the same microscope as explained in the previous section. The system, illustrated in the scheme of Figure 2.3A, included a novel CMOS camera with a 0.5X demagnification and a Tri-Line Laser-Bank with a telescope.

2.5.1 CMOS camera

The CMOS camera is described in the previous section. Within the present configuration, a 0.5X demagnification was used, thus each pixel is mapped to collect light from a square of a ~500 nm.

2.5.2 Illumination

The system is equipped with a Tri-Line Laser-Bank (Cairn Research) through a Ø550 µm, 0.22 NA, SMA-SMA Fiber Patch Cable (Thorlabs, Newton, NJ). The laser head used in the experiments of Na^+ was a multimode diode 520nm / 0.5W (Ushio). A telescope with two lenses (Cairn Research) was used at the output of the fiber. When both lenses were inserted, it generated a homogeneous wide-field illumination at the sample. When using one of the lenses, it generated a concentrated and homogeneous illumination of ~30 µm at the sample. The fiber was stressed and vibrated to mix modes and to reduce laser speckle. For the experiments describing Voltage and Ca^{2+} imaging in Chapter 5, 470nm / 1.2W and 520nm / 0.5W were used respectively.

2.5.3 Filters

For Na^+ imaging experiments, fluorescence excitation light from the laser was band-passed filtered at 517± 20 nm and reflected towards the objective by a 538 nm dichroic mirror. Emitted ANG-2 fluorescence was filtered at 559 ± 34 nm before detection. For V_m imaging experiments, fluorescence excitation light from the laser was band-passed filtered at 517 ± 20 nm and reflected towards the objective by a 593 nm dichroic mirror. Emitted JPW1114 fluorescence was filtered at 610 nm before detection. For the $Ca2^+$ imaging experiments, fluorescence excitation light from the laser was band-passed filtered at 405 ± 40

nm and reflected towards the objective by a 490 nm dichroic mirror. Emitted FuraFF fluorescence was filtered at 531 ± 46 nm before detection.

2.6 Analysis and statistics

All data were analysed in Matlab (The Mathworks Inc. USA) and fluorescence signals were initially expressed as fractional changes of fluorescence ($\Delta F/F_0$). Comparisons were established by performing the paired Student's t-test. A difference was considered significant when $p < 0.005$.

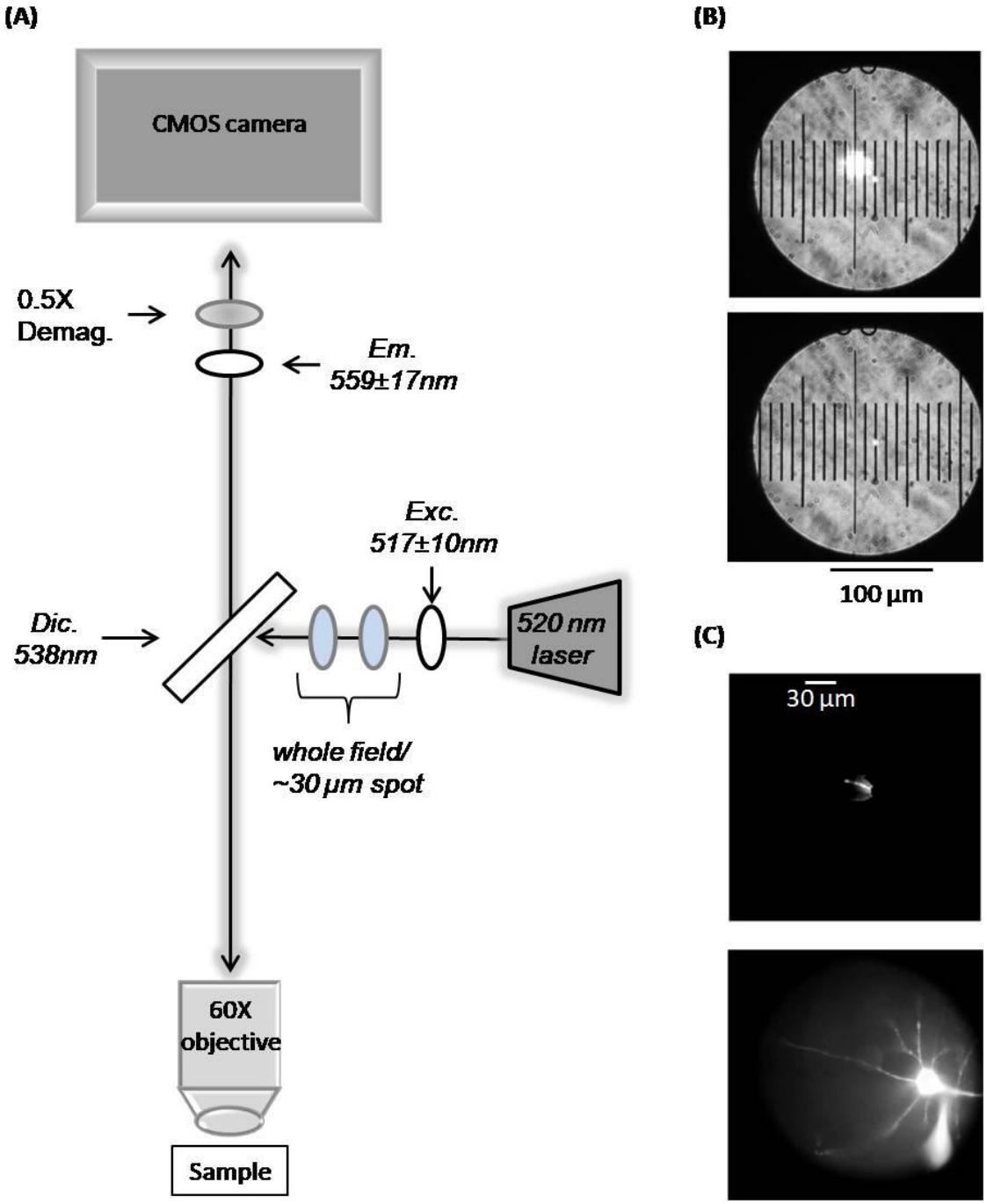

Figure 2.3: *Description of the Na^+ imaging system. (A) Schematic showing the fast CMOS camera and the 520 nm multimode laser. The laser beam was focused with a telescope to illuminate a spot of ~30 µm. Images were demagnified by 0.5X to obtain a pixel resolution of ~500 nm. (B) (top) Iimage of the spot obtained using a uniform fluorescence slide with the 60X objective and 0.5 demagnification. A frame obtained with transmitted light is superimposed and a 0.01 mm intervals grid also shown in the bottom (C) (top) a Layer 5 neuron filled with 0.5 mM ANG2 illuminated by the ~30 µm spot. (bottom) widefield.*

Chapter 3. A novel confocal system for rapid functional imaging in brain slices

To investigate in detail signal processing in neuronal and other cells it is crucial to have precise information on calcium signalling at the highest spatial and temporal resolution and from many sites simultaneously. When designing calcium imaging experiments, this principle translates in recording signals from several sites simultaneously, with a temporal resolution in the ms region and a submicron spatial resolution that can discriminate small compartments such as dendritic spines from their parent dendrites.

In this chapter, I describe a novel confocal system that I developed in the laboratory during my PhD and that has been reported in a publication (Filipis et al., 2018). The system is based on a fast spinning disk, a multimode diode laser and a novel high-resolution CMOS camera. The experimental setup is explained in Chapter 2. Here I demonstrate its effectiveness in rejecting out-of-focus light to resolve signals from submicron structures in the ms range. A characterisation of the performance of the confocal system in comparison to widefield imaging is also reported. Special emphasis is put on the discrimination of signals coming from single spines and their adjacent dendrites. Finally, I show two examples of the system's ability to perform multisite recordings of calcium signals in brain slices with unprecedented spatiotemporal resolution, revealing differences in calcium transient kinetics and compartmental localisation of different calcium sources.

3.1 Characterization of the confocal system

The set-up that I built and used in the experiments of this thesis is fully described in the Materials and Methods chapter (Chapter 2). In this section, I describe the characterization of the confocal system that led to my first publication (Filipis et al., 2018). Specifically, I analyse the optical sectioning, the temporal and spatial performances of the confocal system as well as the bleach improvement in comparison with wide-field imaging recordings obtained by removing the disk from the optical path (see Figure2.3 in the Material and Methods in Chapter 2).

3.1.1 Optical Sectioning

The confocal system was tested for optical sectioning performance against widefield illumination using 500 nm diameter fluorescent beads attached to a coverslip. I took images at different depths bellow the focal plane of the bead with steps of 250 nm (Figure 3.1). The step is comparable to the pixel dimension. In N=16 beads, fluorescence normalised to the value in the focal plane was 0.68 ± 0.09, 0.28 ± 0.09 and 0.10 ± 0.02 at 1, 2 and 3 µm, respectively, using confocal imaging. These values were significantly different from 0.86 ± 0.04, 0.51 ± 0.10 and 0.22 ± 0.12 obtained with widefield imaging ($P<0.01$, paired t-test), indicating an about two fold improvement in the optical sectioning performance of the novel confocal system we developed.

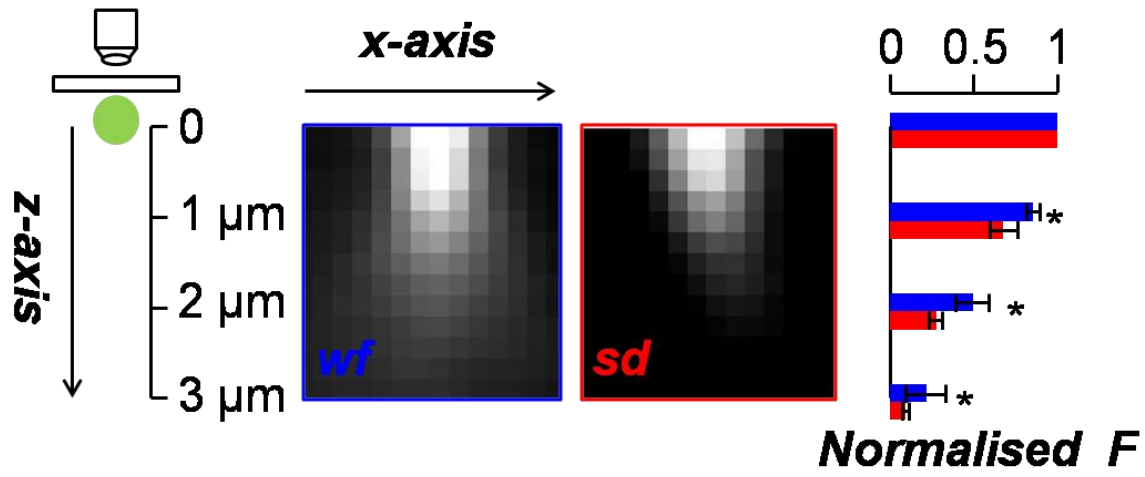

Figure 3.1: *A 500 nm fluorescent bead attached to a coverslip is imaged at different depths with 250 nm steps from its focal plane in widefield (wf) or with the spinning disk (sd); the two images are in the xz plane; on the right the mean ± SD from N = 16 beads of the fluorescence normalised to that in the focal plane at 1 µm, 2µm and 3 µm from the focal plane; * indicates that the difference between sd and wf imaging was significantly different (p<0.001, paired t-test).*

3.1.2 Temporal performance of the system

The temporal resolution of a system is correlated with the detection device. As mentioned in the introduction, different kinds of cameras exist that can offer acquisition rates of less than a millisecond. However, the acquisition rate limits the number of acquired pixels and therefore fast acquisitions rates are typically achieved at the expense of reduced spatial resolution. Nowadays, CMOS devices offer the possibility to record at sub millisecond scale from thousands of points.

The CMOS device developed by Scimeasure within a collaboration with our laboratory, has a very large sensor of 2048 X 2048 pixels of 15μm X 15μm, each arranged in a ~3cm X 3cm area, as illustrated in Figure 3.2A. Each pixel covers an area of 250 nm X 250 nm when using the 60X objective. To reach very high acquisition rates and a high dynamic range, the full frame array is divided into 16 parallel processed arrays of 256 X 1024 pixels each, where digitisation occurs at 14 bits. The actual field of view used in our configuration was half of that, 1024 X1024 pixels, as illustrated by the blue square in the scheme of figure 3.2A.

Figure 3.2B shows the dendrite of a Purkinje Neuron filled with 2 mM OG5N illuminated with a wide-field LED on the left and with the spinning disk and laser on the right. Notably, the light spot covers only part of the 1024 X 1024 pixels. The camera can be set with several configurations that define the maximal acquisition rate, which can be selected according to the experimental needs. Four different configurations are illustrated on the right in figure 3.2B with different colour rectangles representing the acquired pixel array.

- Blue: 1024 X 1024 pixels with a maximal acquisition rate of 200 frames/second.
- Green: 1024 X 512 pixels with a maximal acquisition rate of 400 frames/second.
- Red: 1024 X 256 pixels with a maximal acquisition rate of 800 frames/second.
- Purple: 1024 X 160 pixels with a maximal acquisition rate of 1250 frames/second.

In the 160 X 160 pixels region illustrated in the top Figure 3.2C, one notices how the confocal system de-blurs the images, an effect that can readily be observed by eye. This ability of the spinning disk will be discussed in more detail in the next section of this chapter. Here widefield imaging was done simply to give a visual representation of the full field of view. The aim of this part of the experiments is to characterise the temporal performance of our confocal system and so the following signal analysis will be only on the recordings acquired with the combination of the laser illumination and spinning disk. Ca^{2+} traces associated with a CF-EPSP acquired at the maximal acquisition rate of each configuration are illustrated in the bottom of Figure 3.2C following the colour indication as described above.

These traces correspond to the average $\Delta F/F_0$ of the 40 X 40 yellow region shown on the top right image of Figure 3.2C and 3.2B. The 20% range of fluorescence change shows the great ability of the system to record traces at over 1 KHz speed. Increasing the acquisition speed from 200 Hz to 1250 Hz the unavoidable gradual increase in the noise is obvious, yet even at such high frame acquisition frequency we get a remarkable signal to noise ratio (SNR). Next, we wanted to see if this performance is maintained when looking at submicron structures. To this purpose we focussed on a 7 μm X 7 μm region shown on top left of Figure 3.2D where synaptic spines are distinguishable. On the bottom left of Figure 3.2D, the same picture is illustrated with three superimposed square regions of 2 X 2 pixels corresponding to ~0.25 μm^2. Squares 1 and 3 correspond to two different synaptic spines while square 2 corresponds to a site of the parent dendritic bulk. The traces on the right of the figure show the corresponding $\Delta F/F_0$ at 1250 Hz associated with a CF-EPSP. To improve the SNR, we have averaged three trials, obtaining a discrimination usually obtained by averaging hundreds of trials. In these three traces, besides the remarkable high SNR, one can notice that the traces are kinetically different from each other, something that would not occur in widefield imaging recordings. In summary, we have shown that the system can record Ca^{2+} signals from submicron structures at speeds over 1 KHz.

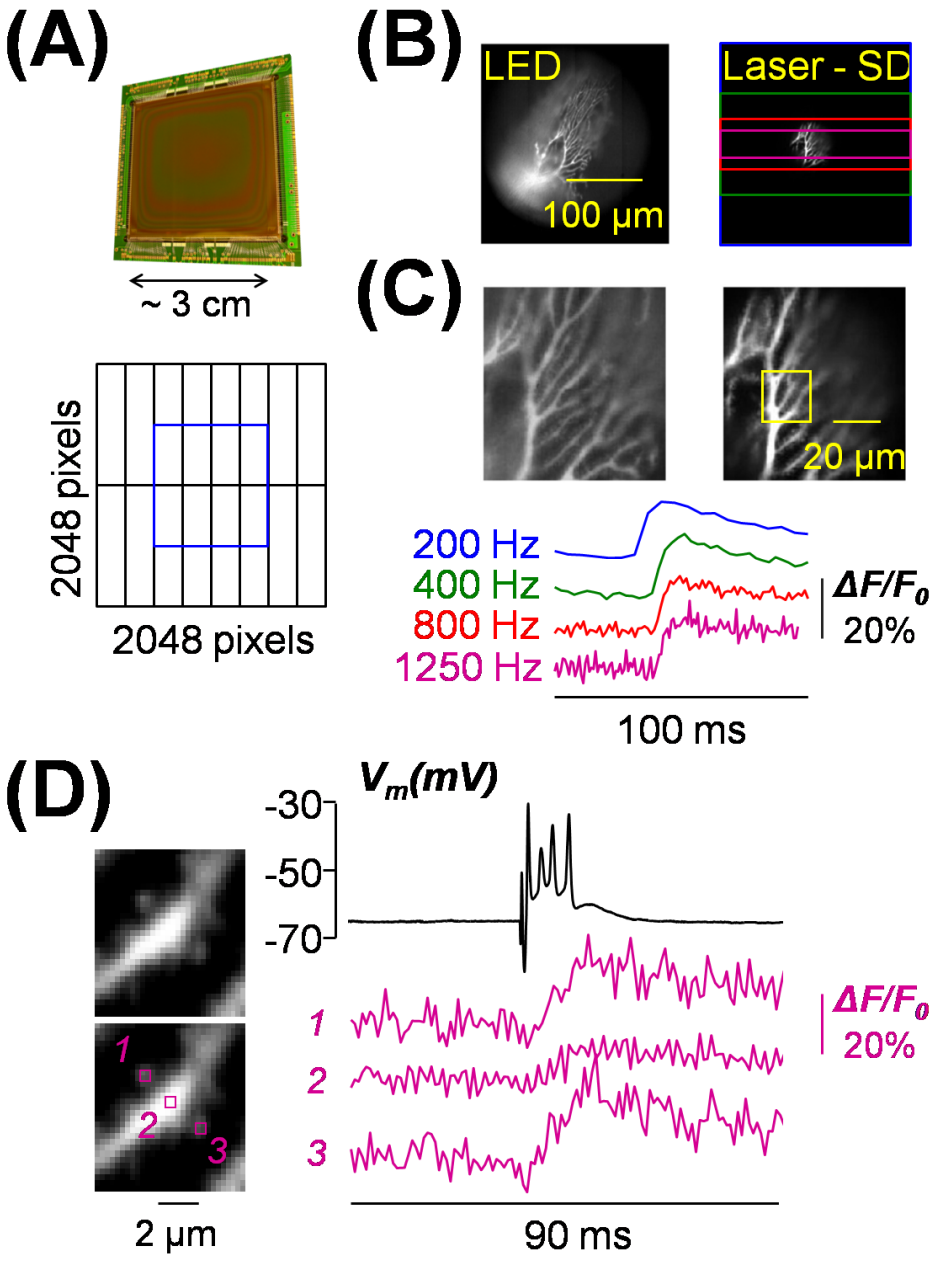

Figure 3.2: *Speed performance of the system. (**A**) Top: picture of the full CMOS sensor composed of 2048 x 2048 pixels of 15 µm X 15 µm (~3 cm length). Bottom: scheme of the 16 parallel processed sectors with blue square indicating the actual field of view. (**B**) Images of a PN filled with OG5N obtained with widefield LED illumination (left) and laser and spinning disk (right); in the image on the right, the blue, green, red and purple rectangles are CMOS areas where acquisitions can be achieved at maximal speeds of 200, 400, 800 and 1250 frames/s. (**C**) Top: image detail (160X160 pixels) obtained with widefield LED illumination (left) and laser and spinning disk (right); Bottom: Ca^{2+} signals (single trials) associated with a CF-EPSP at the maximal speeds of the four rectangles in the yellow region on the top-right image. (**D**) Left: detail of the image in (A) with regions (2X2 pixels, ~0.25 µm^2) 1 and 3 corresponding to synaptic spines and 3 in the parent dendrite. Right: Ca^{2+} signals (average of 3 trials) associated with a CF-EPSP in regions 1-3; somatic patch recording on the top.*

3.1.3 Spatial performance of the system

After having characterized the temporal performance of the system, we focus the attention on the precise localization of signals, which is essential for understanding important physiological mechanisms in neurons. Different signaling pathways can be activated at different sites of the neuronal dendrites or in the spines. A major factor that reduces the spatial resolution is the scattered light. To minimize the scattered light, no tissue should be present between the fluorescent site of interest and the objective (only the solution in the case of a water-immersion objective). However, in brain slices, the cell can be several tens of microns below the surface. This fact produces light scattering by the tissue which will increase with the thickness of the tissue, i.e. with the localization of the cell in the z-axis (depth from slice surface).

A major objective of our confocal system is to de-blur the images from the light scattering produced by the tissue between the fluorescence site and the objective. In other words, the goal is to recover the spatial resolution that would be attained if no tissue is present, which is essentially limited by light diffraction. In this section, we demonstrate that our confocal system can de-blur images to faithfully resolve signals from neurons within 40 μm from the surface with a high spatial and temporal resolution.

In order to characterise the spatial performance of our confocal system we used CA1 hippocampal pyramidal neurons because the initial part of the apical dendrites of these neurons has an approximately cylindrical geometry. We obtained sequential recordings with or without the spinning disk (widefield vs. confocal imaging) of dendrites located at approximately 20 μm to 60 μm depth from the surface of the slice. This depth is indicated by "δ". Figure 3.3A shows three different dendritic portions at δ=23, 37 and 50 μm, obtained in widefield (wf) or confocal (sd) imaging. The scattering effect, as we go deeper into the slice, is visible on these figures as well as the deblurring effect of the spinning disk.

We compared the fluorescence profile of the dendrites in each case by measuring the light across a line drawn on an in-focus site of the dendrite (X lines shown in Figure 3.3A). The absolute intensity profile across the line is shown in Figure 3.3B where the maximum is placed on X=0. Each point corresponds to light averaged over a 2 x 4 pixel region across the line and the values were normalised to the maximum. The profile was then fitted with a Lorentzian function:

$$L = \frac{1}{\pi} \cdot \frac{\Gamma/2}{X^2 + \left(\frac{\Gamma}{2}\right)^2}$$

Where Γ specifies the width of the intensity profile and depends both on the dendrite's thickness and the light scattering (Corle 1986).

Figure 3.3C reports the analysis of intensity profiles from 8 different dendrites in 5 cells. Γ values in widefield (Γ_{wf}) and confocal imaging (Γ_{sd}), as well as their difference (Γ_{wf} - Γ_{sd}) increase with the depth δ. And while Γ_{wf} and Γ_{sd} depend both on the dendrite's thickness and the light scattering, their difference should depend only on tissue scattering. The systematic increase of Γ_{wf} - Γ_{sd} provides an estimate of the improvement produced by the use of the spinning disk. This result indicates that at positions $\pm\Gamma_{sd}$ the Ca^{2+} transients acquired with the confocal system have been cleared from scattered light. To visualize this conclusion, we calculated the $\Delta F/F_0$ associated with 4 action potentials at $X=\pm\Gamma_{sd}$ for widefield and confocal imaging and normalised the signals to those at X=0. As shown on the right of Figure 3.3B, the $\Delta F/F_0$ at $X=\pm\Gamma_{sd}$ was systematically smaller in confocal imaging. Figure 3.3D reports the mean ± SD of normalized $\Delta F/F_0$ peak at $\pm\Gamma_{sd}$ that was 0.27 ± 0.07 in confocal imaging and almost double 0.55 ± 0.17 in widefield imaging ($P < .001$, paired t-test). The comparison between widefield and confocal imaging indicates that, within 40 μm from the slice surface, the gain in spatial resolution quantified by Γ_{wf} - Γ_{sd} was between 200 and 600 nm. We thus obtain direct evidence that, in this δ region, our confocal system can effectively de-blur images to restore spatial resolution closer to the diffraction limit.

Having characterised the deblurring effect of the confocal system in the z-axis, we then tested the ability of the system to specifically resolve signals from submicron structures in the δ range up to 40 μm below the surface. To do this we measured the $\Delta F/F_0$ associated with CF-EPSPs from PN synaptic spines, again comparing widefield and confocal imaging. Figure 3.4A shows a PN dendrite and its adjacent spines at δ=25 μm imaged either in widefield (wf) or confocal (sd) configuration. We measured the averaged $\Delta F/F_0$ on 2x2 pixels centred in two different spines in focus from an average of 8 trials.

To see how much the confocal deblurs the image we did the same measurement in regions outside the cell, ~0.5 μm and ~1 μm away from the edge of the spine centred region . Figure 3.4B shows that, in widefield imaging, there is no significant difference in Ca^{2+} signals coming from the spines or the adjacent regions outside the cell due to the scattered light. In contrast, with confocal imaging, signals were progressively smaller with distance from the

spine, indicating scattered light elimination by the spinning disk. The same analysis was done in 48 spines in focus from 6 cells with varying δ from 18 to 30 μm. Figure 3.4C reports the mean ± SD of $\Delta F/F_0$ peaks at ~0.5 μm and ~1 μm away from the spines, normalised to the peaks on the spines, in widefield and confocal configuration. In confocal imaging, the normalised peak at ~0.5 μm was 0.62 ± 0.11; while in widefield imaging at the same distance it was significantly larger at 0.90 ± 0.13 ($p < 0.001$ paired t-test). The difference was even more pronounced at the ~1 μm distance where in confocal configuration the mean ± SD was 0.29 ± 0.08 while in widefield this was significantly larger, 0.86 ± 0.16 ($p < 0.001$, paired t-test). In particular, this ~0.3 value at ~1 μm distance with the confocal configuration is within our ability to discriminate the signal from noise.

Thus, these results indicate that our confocal system, unlike widefield imaging, can resolve Ca^{2+} signals from submicron structures in the δ range of up to ~40 μm.

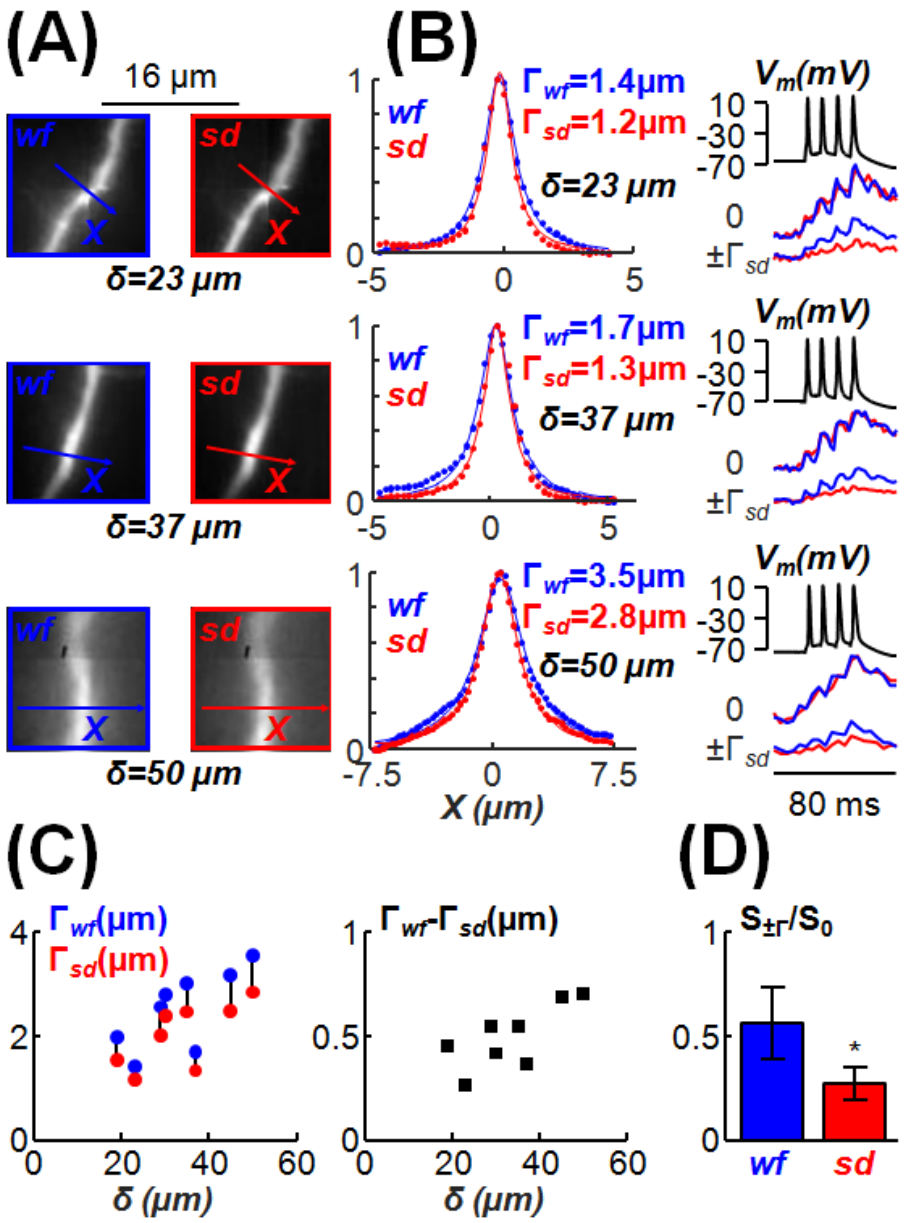

Figure 3.3: *Improvement of spinning disk (sd) imaging with respect of widefield (wf) imaging at different depths from the slice surface (δ). (**A**) Images of three apical dendrites from CA1 hippocampal pyramidal neurons at δ = 23, 37 or 50 µm with wf imaging (blue, left) or with sd imaging (red, right); the X axes of analysis are positioned on the dendritic part in focus. (**B**) Left: fluorescence normalised to the maximum (at X = 0) along the X axes (points) fitted with a Lorentzian function (lines) in the three cases with wf and sd imaging; each spot was calculated by averaging fluorescence of 2X4 pixels; Γ values are indicated. Right: Ca^{2+} signals (average of 4 trials) associated with 4 action potentials at 10 ms interval at X = 0 and X = ±$Γ_{sd}$; since the sd is removing scattered light, the Ca^{2+} $ΔF/F_0$ signal drops away more rapidly with distance from the dendritic centre making confocal imaging significantly better is resolving the origin of a Ca^{2+} signal. (**C**) Γ values with wf and sd imaging (left plot) and their difference (right plot) versus δ in 8 X-lines from 5 cells. (**D**) Mean ± SD of Ca^{2+} $ΔF/F_0$ signal associated with 4 action potentials at X = ±Γ, normalised to the signal at X = 0, in 8 X lines from 5 cells; * indicates that the sd signal was significantly smaller than the wf signal (p<0.001, paired t-test).*

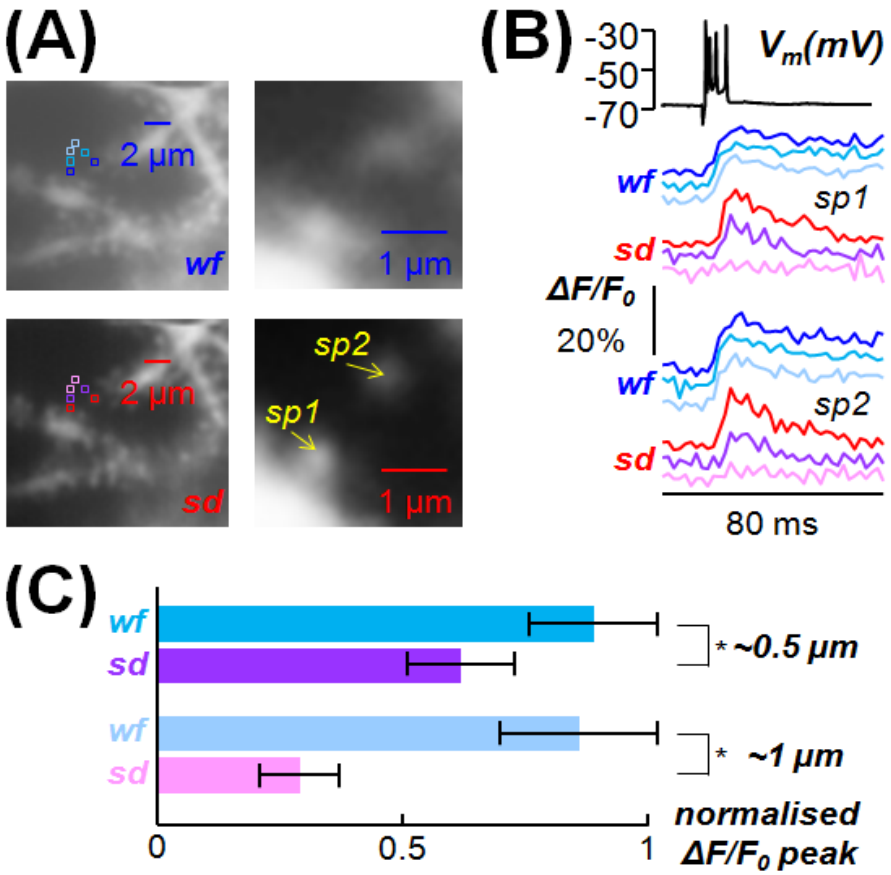

Figure 3.4: *Ability of the system to resolve Ca^{2+} transients from synaptic spines. (**A**) Images of a PN dendrite at δ = 25 µm with widefield illumination (wf, top) or with the spinning disk (sd, bottom); two spines in focus (sp1 and sp2) are indicated on the right; 2 X 2 pixels regions centred on sp1 and sp2, at ~0.5 µm from the spine or at ~1 µm from the spine are shown on the left. (**B**) Ca^{2+} signals (average of 8 trials) associated with a CF-EPSP at 500 Hz in the regions in (A) shown in the same colour code; somatic patch recording on the top; the Ca^{2+} $\Delta F/F_0$ signal decreases with distance in sd imaging but not in wf imaging. (**C**) Mean ± SD of Ca^{2+} $\Delta F/F_0$ signal associated with a CF-EPSP, normalised to the signal in the spines, from 2 x 2 pixels regions at ~0.5 µm from the spine or at ~1 µm from the spine calculated over 48 spines in focus in 6 cells with δ ranging from 18 µm to 30 µm; * indicates that both at ~0.5 µm and at ~1 µm the difference between sd and wf imaging was significantly different (p<0.001, paired t-test)*

3.1.4 Bleach improvement

In experiments that involve rapid image acquisition or long image duration, photobleaching can be a major factor limiting fluorescence detectability and compromising the calibration of the Ca^{2+} concentration. Photobleaching is the process at which a fluorophore undergoes loss of fluorescence, while at its excited state, mainly because of interaction with oxygen (D-O) or another fluorescence molecule in its excited state (D-D).

The confocal system seems to have another advantage over the widefield imaging by reducing the bleaching. The dendrite in the bottom Figure 3.5A was exposed to laser illumination for 80 ms at the maximum laser intensity with the spinning disk. The same dendrite shown in the top Figure 3.5A was exposed for the same time at reduced laser intensity to get a similar photon noise, without the spinning disk this time. As shown in Figure 3.5B, photobleaching reduced fluorescence by ~3% in widefield imaging, but only ~0.5% in confocal imaging. This result was confirmed with 7 other cells where bleaching was 2.9 ± 1.0% in widefield imaging and 0.5 ± 0.1% in the confocal setup (P<.001 paired t-test). This result indicates that spinning disk imaging can dramatically reduce photobleaching.

A possible explanation of this result is that the spinning disk is not continuously illuminating the whole sample but, as it rotates, regions of the sample are illuminated for shorter times. During fluorescence imaging, the illuminated fluorophore absorbs a photon and moves from its ground state to an excited 'singlet' state before returning back to the ground state, in the nanosecond timescale, emitting a photon with a longer wavelength (Jablonski.1935). Alternatively, there is a probability that the fluorophore, instead of the 'singlet' state, will be excited to a non fluorescent 'triplet' state which has a longer, microsecond time scale of decay. While at the 'triplet' state, the fluorophore can absorb additional photons and break covalent bonds releasing reactive oxygen species which can cause further photobleaching (Donnert et al., 2007). The fact that the spinning disk does not allow continuous illumination could provide enough time for some molecules in the 'triplet' state to return back to the ground state instead of absorbing additional energy and break down. This is explanation is confirmed by reduced photobleaching observed in experiments with pulsed excitation light (Nishigaki et al., 2006; Penjweini et al., 2012) and high speed confocal laser scanning (Borlinghaus et al., 2006).

Furthermore, in both confocal and widefield imaging, bleaching shows a single-exponential decay rate indicating that the distance between the fluorescent molecules is greater than the average distance to oxygen (Song et al., 1995). In all other cases the decay

rate can be approximated by a discrete sum of exponentials (Berglund, 2004), such as the tri-exponential decay rate used to describe photobleaching of the Na^+ fluorescent indicator dye used in chapter 5.

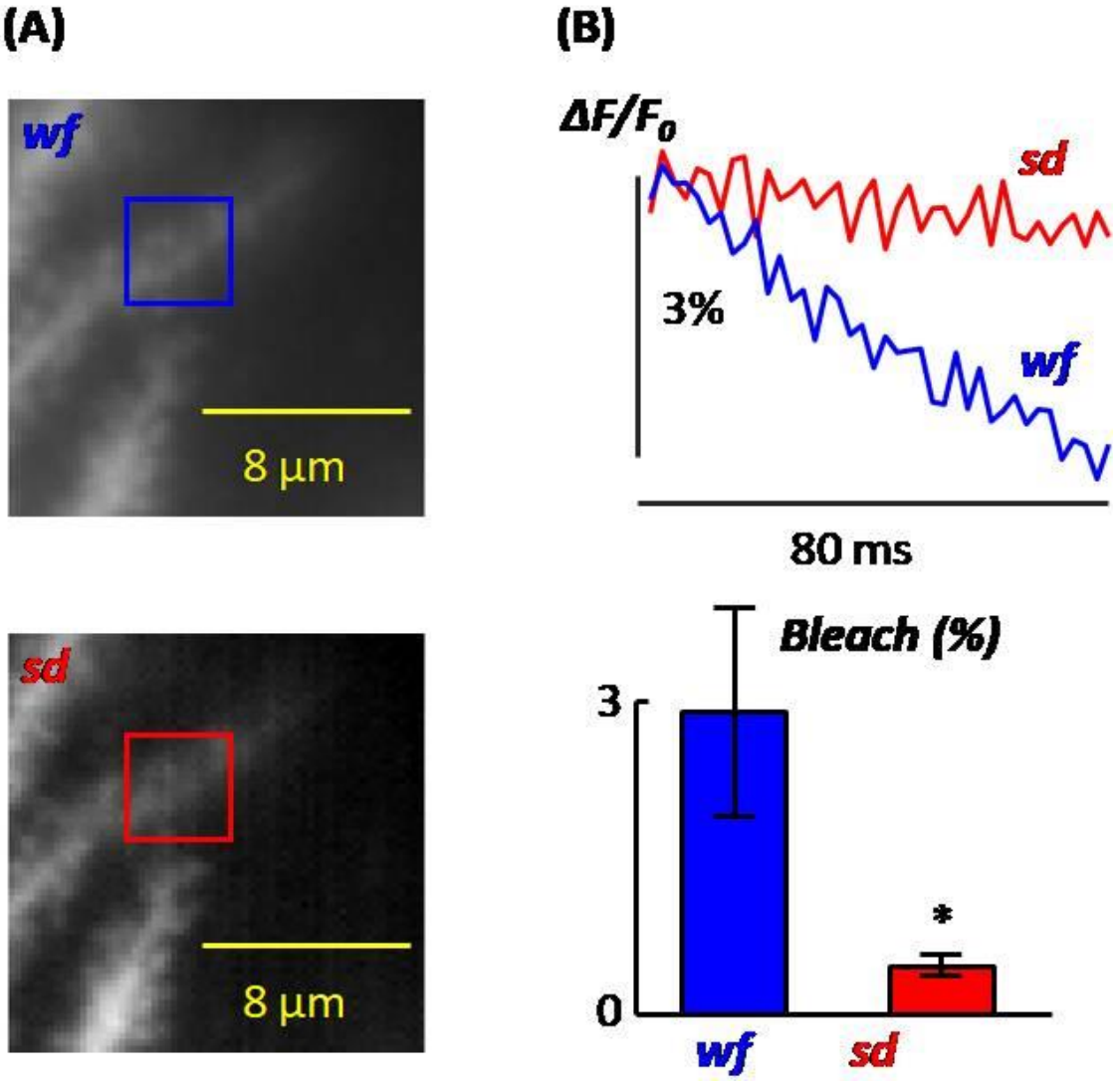

Figure 3.5: *Bleach improvement of the system. (**A**) Images of a PN dendrite detail with widefield illumination (wf, top) or with the spinning disk (sd, bottom); a region of interest is indicated. (**B**) Top: $\Delta F/F_0$ from the region of interest in (A) in wf (blue trace) and sd (red trace) mode following 80 ms light application; light intensity was the maximum for the sd whereas it was decreased in wf in order to obtain comparable photon noise. Bottom: mean ± SD of the $\Delta F/F_0$ in wf and sd (red trace) mode following 80 ms light application, calculated from N = 7 cells; * indicates that the difference between sd and wf imaging was significantly different ($p<0.001$, paired t-test)*

3.2 Examples

After having evaluated our novel confocal system in terms of spatial and temporal capabilities, the following two examples give an idea of the information that we can obtain. These examples illustrate the advantage of recording multiple sites simultaneously with a high spatiotemporal resolution, in contrast to traditional scanning systems where only a few selected submicron regions can be simultaneously analysed. We studied two examples of Ca^{2+} signals in the dendrites and dendritic spines of the cerebellar Purkinje neuron (PN).

The study of the cerebellum is of high importance in neuroscience because of the multiple functions it serves in balance, equilibrium, muscle tone, coordination and motor learning. In addition, it has been shown recently to play a role in several cognitive processes (Glickstein, 2011). The PN is the principal neuron of the cerebellar cortex since it provides the sole output to the deep cerebellar nuclei. The PN receives excitatory input from two sources, the Climbing Fibre (CF) and the Parallel Fibres (PFs).

In the next two examples we recorded Ca^{2+} signals in Purkinje Neuron dendrites associated with each of these two inputs. The physiology of the CF-PN synapse will be the subject of Chapter 4 and will be introduced in more detail in that part of my thesis.

3.2.1 Example 1: Ca^{2+} signals associated with the Climbing Fibre

In the first example we studied the Ca^{2+} signals associated with the CF input. The CF originates from the inferior olive and each fibre wraps tightly around the soma and proximal dendrites of a PN forming about 500 contacts (Silver et al., 1998) in the process. Each PN receives input from exactly one CF while each CF contacts approximately ten Purkinje neurons. When the PN is depolarized by a CF excitatory synaptic potential (EPSP), a complex spike occurs. PN depolarization spreads throughout the dendritic tree where it activates voltage-gated Ca^{2+} channels (VGCCs). The distribution of these channels and their biophysical properties is of high importance and their characterization will be fully described in chapter 4.

Here, we recorded the Ca^{2+} signal associated with a CF-EPSP in a PN to provide a meaningful example of the capabilities of our system. We recorded signals at 500 Hz from a dendritic region with several spines where we can compare the differences between multiple spines and their parent dendrites. Figure 3.6A shows the PN and two selected regions on the left while on the right we see these two regions zoomed in and two spines and their parent

dendrite selected in each region. Figure 3.8B illustrates the representative $\Delta F/F_0$ of each spine and its parent dendrite. These signals indicate that the Ca^{2+} kinetics are systematically different in spines and dendrites. In spines, the Ca^{2+} signal is much larger and decays more rapidly compared to that of the parent dendrite. This phenomenon can be attributed to several phenomena such as a different distribution of Ca^{2+} channels or Ca^{2+} -binding proteins or to a different surface-to-volume ratio between dendrites and spines.

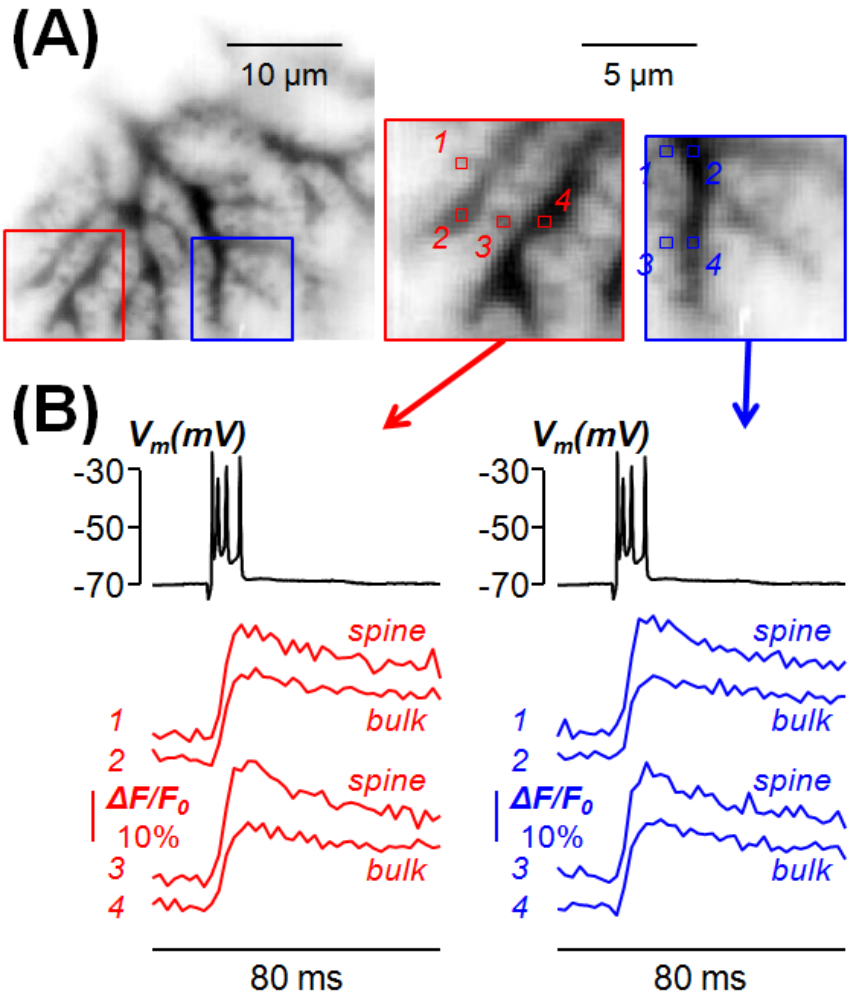

Figure 3.6: *Example 1: analysis of Ca^{2+} transients associated with a CF-EPSP. (**A**) Left: intensity inverted confocal image of a PN filled with OG5N. Right: enlargements of the red and blue square regions of the left with four spine regions (1 and 3) and four regions of the parent dendrites (2 and 4). (**B**) Ca^{2+} signals (average of 8 trials) associated with a CF-EPSP at 500 Hz in the spines and dendritic regions in (A); somatic patch recording on the top.*

3.2.2 Example 2: Ca^{2+} signals associated with the Parallel Fibre

In the second example, we studied the Ca^{2+} signals associated with the PF input from cerebellar granule cells. PFs release glutamate which can activate α-amino-3-hydroxy-5-methyl-4-isoxazolepropionic acid (AMPA) receptors and type-1 metabotropic glutamate receptors (mGluR1s) at the PN spines (Tempia et al., 1996; Hoxha et al., 2016). Notably, AMPA receptors in PNs are not Ca^{2+} permeable and, therefore, Ca^{2+} entry during AMPA receptor activation is due to voltage-gated Ca^{2+} channels activated by dendritic depolarization (Hoxha et al., 2016). In contrast, mGluR1 activation triggers Ca^{2+} signals (Finch and Augustine, 1998; Takechi et al., 1998; Tempia et al., 2001).

Here, we recorded the Ca^{2+} signal associated with a train of 5 PF-EPSPs in a PN to specifically analyze the ability of the system to resolve signals from the spines of origin. In this example, Ca^{2+} transients from spines and dendrites in a region of ~100 μm^2 were recorded. Figure 3.7A shows the PN and a selected region on the left while on the right we see this region zoomed in and several spines and dendritic regions selected. Figure 3.7B illustrates the somatic recording (top) and the representative $\Delta F/F_0$ of each spine and dendrite indicated in panel A. We recorded signals at 250 Hz from this dendritic area with several activated spines where we could compare the differences between the signals from the different spines and the adjacent dendritic sites. The spatial pattern of the Ca^{2+} signal in this case is given by the number and spatial distribution of the activated PFs.

The signals reported in Figure 3.7B indicate that the Ca^{2+} transient has two distinguished components. The first and fast component nearly coincides with the EPSPs recorded in the soma (Canepari and Vogt, 2008). The second and slow component is mediated by mGluR1s (Canepari and Ogden, 2006). In particular, mGluR1s activate a slow non selective cation conductance that is responsible for this component of the Ca^{2+} influx (Canepari et al., 2001). The false-colour scale images in Figure 3.7C illustrate the spatial profile of the signal at different time-windows of the recording; in particular images *b* and *d* correspond to the peak of the fast and slow components. As shown by these images, but also by the traces in panel B, the two images do not spatially overlap within dendrites or spines. In addition, the fast component is larger than the slow component at some sites while in other sites it is the opposite. This result suggests that mGluR1 activation does not spatially coincide with activation of VGCCs, i.e. that PF-EPSPs may trigger multiple signalling pathways at different sites of the dendrite.

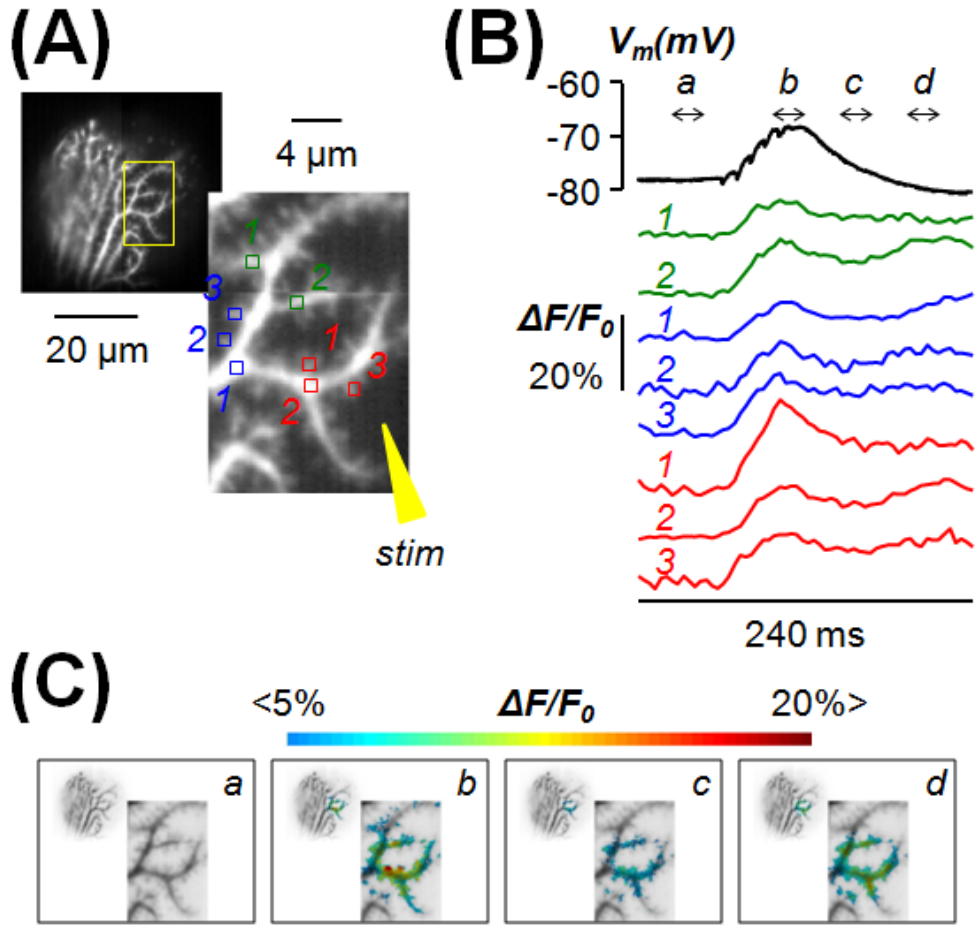

Figure 3.7: *Example 2: analysis of Ca^{2+} transients associated with parallel fibre EPSPs. (**A**) Left: confocal image of a PN filled with OG5N. Right: enlargements of the activated dendritic region with 8 spine or dendritic regions indicated. (**B**) Ca^{2+} signals (average of 8 trials) associated with a train of 5 parallel fibre EPSPs at 250 Hz in the spines and dendritic regions in (A); somatic patch recording on the top. (**C**) Colour scaled signals of the experiment in (B) superimposed on the inverted fluorescence image of the dendrite. Signal profiles are obtained by averaging 6 frames in the time windows a, b, c and d indicated in (B). Signal b corresponds to the peak of the fast component of the Ca^{2+} transient, mediated by voltage-gated Ca^{2+} channels. Signal d corresponds to the peak of the slow component of the Ca^{2+} transient, mediated by metabotropic glutamate receptors.*

3.3 Significance of this work

In neurobiology it is important to be able to measure fast Ca^{2+} signals from different sites, such as dendrites and spines, with the highest possible spatial and temporal resolution. Ongoing research, exploiting several approaches, is devoted to improve imaging techniques in this direction (Coates et al., 2002; Oertner, 2002; Takahara et al., 2011; Ceriani et al., 2016; Nguyen et al., 2016).

In this respect, confocal imaging is possibly the simplest and cheapest approach, as well as easiest to implement. However, traditional confocal systems are based on scanning a pinhole over the recording region and therefore are limited in either number of recorded points or in temporal resolution. Indeed, today, a standard confocal imaging system can operate in the kHz range but either the number or recorded sites is limited, or a higher number of recording sites corresponds to a proportionally shorter exposure time resulting in larger noise.

Other systems are based on fixed pinhole arrays (Tominaga and Tominaga, 2013) where the number of recorded points is larger, but in this case the flexibility in choosing the recordings sites is compromised. Hence, the strategy of using Nipkov (or spinning) disks is currently the most convenient strategy to overcome these limitations (Coates et al., 2004).

The novel fast confocal system described here is based on a spinning disk specifically designed to investigate Ca^{2+} signals in submicron neuronal compartments in brain slices, in combination with patch clamp recordings. It must be pointed out that, in the last few years, the dramatic fall in price of diode lasers make a system as the one described here affordable also for laboratories of relatively low size. Our results demonstrate the ability of this confocal system to overcome the inherent limitations of standard confocal imaging allowing the recording of Ca^{2+} transients from continuous structures and tens of thousands pixels simultaneously. The capability to study structures at 20-40 µm from the slice surface allows for single neuron imaging nearly free of scattered light, unlike wide-field imaging. Moreover, the achieved recordings at 250-1250 Hz from submicron structures show the ability of the system to detect fast Ca^{2+} transients associated with action potentials or synaptic activity. This was possible thanks to the combination of the fast custom-patterned spinning, the efficient powerful laser source and the novel fast CMOS camera (see Materials and Methods). The two examples described in this chapter show the application of the confocal system into measurements of fast Ca^{2+} imaging in different cases. Differences in signal amplitude, decay or peak time were identified between spines and their parent dendrites, between different dendritic compartments or between adjacent spines. Despite this, the

resolution is still insufficient to measure the kinetics of fast Ca^{2+} channels, a goal that will be addressed in the next chapter.

At present, the temporal resolution of the confocal system appears to be limited mainly by the number of detected photons, which is intrinsically reduced in a confocal approach based on light rejection. This can be ameliorated, for example, by increasing the light intensity. We have achieved this in Chapter 5 by introducing a telescope that focuses the laser beam into a spot of ~20 µm instead of 60 µm.

Another way to obtain submicron resolution without rejection of emitted light is to use two-photon imaging that, in contrast to confocal imaging, also allows axial confinement of fluorescence excitation. Two-photon imaging without scanning microscopy can be achieved by patterning the light shape to match the imaged structures, i.e. by performing holographic illumination (Papagiakoumou et al., 2013). In membrane potential imaging, signals have been recorded at several kHz from small neuronal compartments using one-photon holographic illumination (Tanese et al., 2017). In contrast, two-photon holographic illumination has been done for Ca^{2+} imaging, but without achieving recordings from submicron structures in the kHz range (Pozzi et al., 2015; Yang et al., 2016). Yet, it appears possible to achieve this resolution in the near future.

Whereas two-photon imaging combined with holographic illumination is potentially a more powerful approach, the present confocal system has several advantages. It can be easily coupled to existing microscopes equipped for patch clamp recordings; it requires moderate knowledge of optics to implement the measurements; and it is economic and requires minimal maintenance. For these reasons it is expected that this system will be adopted to measure Ca^{2+} transients from submicron structures at high temporal resolution.

Chapter 4. Development of a simplified Neuron model to extract the activity of ion channels in neuronal dendrites

The improvements in imaging techniques over the years have allowed us for more detailed investigation of the neuronal functions. An example of recent improvement is the work presented in the previous chapter, with the confocal system developed in our laboratory being able to record from multiple sites of a neuron with a spatial resolution in the µm range and a temporal resolution in the ms range. Yet, the availability of unprecedented large sets of data requires a novel strategy of analysis to extract useful information. An important case is that of the multi-channel kinetics that characterise a particular neuronal signal.

Previous research from our laboratory has shown that the kinetics of VGCCs can be extracted by ultrafast Ca^{2+} imaging (Jaafari et al., 2014; Jaafari and Canepari, 2016) for instance in the PNs (Ait Ouares et al., 2016). Nevertheless, a signal is the result of a complex synergy of several types of ion channels and the analysis of Ca^{2+} and membrane potential (V_m) transients can lead to the extraction of all relevant channels involved in a signal.

In the case of PNs, where the role of the CF in short and long term depression of the PF inputs is established (Brenowitz and Regehr, 2005; Safo and Regehr, 2005), the kinetics of each channel involved in the CF signal is of high importance in understanding how the CF transmits information in the dendritic arborisation. The CF can be activated by electrical stimulation in the granule cell layer near the PN in sagittal slices. The CF activation is associated with a large current of more than 2 nA at -60 mV that depolarises the soma and proximal dendrite of the Purkinje Neuron (Llano et al., 1991). This depolarisation then spreads in the dendritic arborisation where it activates Ca^{2+} and K^+ Voltage Gated Channels (Canepari and Vogt, 2008). Interestingly, voltage-gated Na^+ channels are not expressed beyond the major branches of the dendrites, a fact that simplifies the study of the channels kinetics in this specific neuronal type (Llinás and Sugimori, 1980, Stuart and Häusser, 1994). The activated Ca^{2+} channels allow Ca^{2+} to flow into the cell and, as a result, to activate Ca^{2+}-activated K^+ channels that contribute to afterhyperpolarisation (Stocker, 2004). Some of these Ca^{2+}-activated K^+ channels, namely the BK channels, are gated both by voltage and Ca^{2+} and, in general, all of these channels may even be coupled, at molecular level, to specific Ca^{2+} channels (Anwar et al., 2012; Edgerton and Reinhart, 2003, Stocker, 2004; Cueni et al.2008).

Besides this, the dynamics of the free intracellular calcium are determined by calcium buffers such as Parvalbumin, Calbindin etc. (Schwaller 2010, Canepari and Mammano 1999).

Electrode techniques are routinely used to investigate channel kinetics and their biophysical properties (Sakman and Neher, 1984; Stuart and Spruston, 1995). In particular, single channel or whole-cell patch clamp recordings are performed in transfected cells which are used to isolate one channel type only (Maki et al., 2014; Fertig et al., 2002). Thus, single channel recordings are a very powerful approach that has provided a good understanding of the principal properties of channel kinetics. Yet, native ion channels are always expressed in multiple types and, as they interact with their environment, their kinetics differ from that of isolated channels expressed in heterologous systems (Hamil, 1981). The use of blockers along with imaging recordings, on the other hand, allows a channel to be studied in its native environment. In this case however, even if the blocking is complete and totally specific, the indirect effect on other channels makes it hard to extrapolate the kinetics by simple linear subtraction of the two signals before and after addition of the blocker (Yu et al., 2005). Principally, the use of computational models along with the above technique can be the ideal approach to overcome the technical limitations. This was a major objective of the projects carried out during my thesis.

In the work presented in this chapter, I developed an original approach to combine computational modelling with Ca^{2+}/V_m imaging and with channel blocking using selective toxins or organic molecules to tackle the problem of calculating the channel kinetics activated by the CF-EPSP in the dendrites of the PN. Specifically, I used the data provided by Karima Ait Ouares and described in her thesis (discussed in April 2019) where she first acquired sequential V_m and Ca^{2+} optical measurements by alternating excitation of FuraFF and the Voltage sensitive (VSD) JPW1114 (example shown in Figure 4.1). Electrical and optical signals associated with the CF-EPSP were recorded for 20 ms with the CF stimulation occurring 2 ms after the beginning of trials. Fluorescence from a region of ~17 x 17 μm^2 was averaged and V_m and Ca^{2+} signals at three different initial V_m: hyperpolarized (hyp, ~-80 mV), intermediate (int, ~-65 mV) and depolarized (dep, ~-50 mV) were expressed in mV and $[Ca^{2+}Dye]$ respectively. Then, using the OG5N she did Ca^{2+} imaging along with pharmacological analysis where specific channels where locally blocked and signals where provided as fractional changes of fluorescence proportional to $[Ca^{2+}Dye]$.

Based on this rich experimental dataset, I built a NEURON model of a simplified PN dendritic compartment as shown in the schematic of Figure 4.1. The model is based on a study by Anwar et al. (2012) and incorporates modified channel models to accurately

reproduce the V_m and Ca^{2+} transients associated with the CF-EPSP at different initial V_m. The model included P/Q-type high-voltage activated (HVA) VGCCs, T-type low-voltage activated (LVA) VGCCs, A-type LVA-VGKCs and Ca^{2+}-activated K^+ channels (both SK and BK). The model also included a generic HVA-VGKC (HVAK), an immobile endogenous Ca^{2+} buffer (Canepari and Mammano, 1999), and the two Ca^{2+} binding proteins Calbindin-D28k and Parvalbumin highly expressed in PNs (Maeda et al., 1999; Kosaka et al., 1993).

The systematic and extensive feedback between experiments and model simulations allowed the investigation of the physiological kinetics of all dendritic Ca^{2+} and K^+ channels activated by the CF-mediated V_m transient, under different initial V_m conditions, providing a realistic model for the ion channels. This model is also available in the ModelDB website under the reference #244679. My original work described below was performed in collaboration with Panayiota Poirazi and Alexandra Tzilivaki (IMBB-FORTH, Heraklion-Crete, Greece).

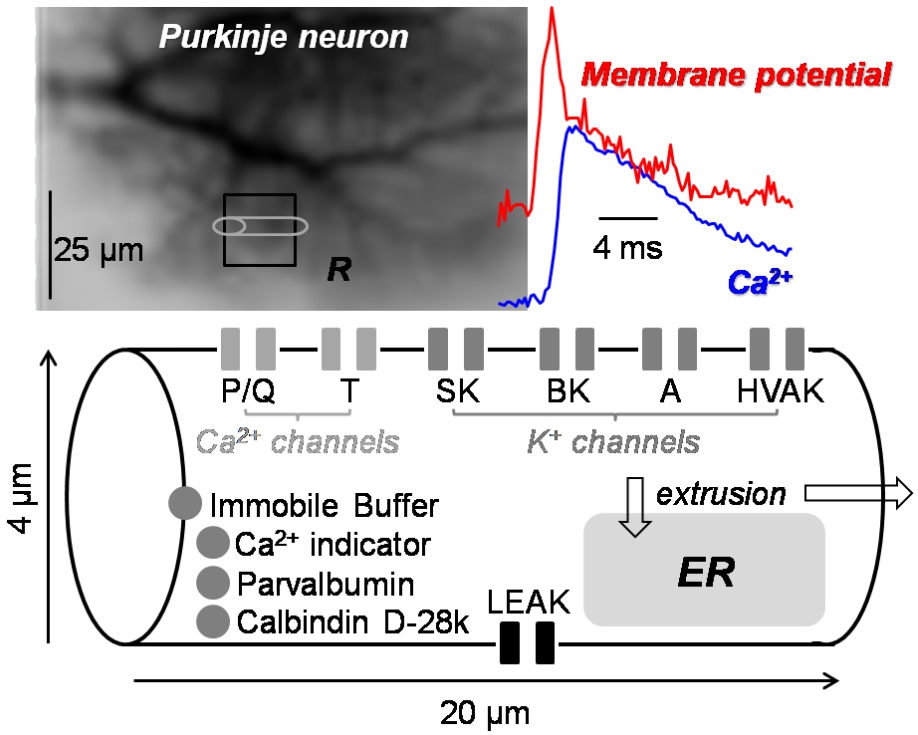

Figure 4.1: *Up: Image of a Purkinje Neuron provided by Ait Ouares with the square region R indicating a region of ~17 x 17 µm² and the cylinder of 4 x 20 µm² approximating this region in the model. An example of averaged V_m and Ca^{2+} signals measured experimentally in such a region. Down: Schematic of the model with the mechanisms included.*

4.1 Constant parameters of the model

As mentioned in the Materials and Methods, the simulation was based on the published model of Anwar et al., (2012) designed to predict activation of Ca^{2+} activated K^+ channels in PN dendrites. This model can be found on ModelDB under the reference #138382.
Several parameters, such as the morphology and passive membrane parameters were adopted from this model and maintained in the model I developed here. The detailed Ca^{2+} dynamics of this starting model were also partially adopted as explained in the following sections.

4.1.1 Morphology

The morphology of the model was adopted from the starting model and consists of a cylinder of 4 µm diameter and 20 µm length that approximates the dendritic region of ~17 x 17 μm^2 where experimental recordings were provided. The single compartment model, instead of the morphologically detailed, was chosen to reduce the number of free parameters. Considering a morphologically detailed model with N compartments would increase the free parameters by N as well and therefore it would lead to multiple solutions of the problem without providing any additional information on our question, which are the channel kinetics and the interaction of different channels.

4.1.2 Passive membrane parameters

The passive membrane properties were also adopted from the starting model with the axial resistant set at R_a=250 Ω·cm and the membrane capacitance at cm=1.5 µF/cm^2.

4.1.3 Leak/Shunt

The leak current was set as 0.002 mA/(mV·cm^2)·(V_{init}-V_{rest}) where V_{init} is the initial V_m (in mV) and V_{rest} is the resting V_m (-65 mV).

4.1.4 Ca^{2+} Buffering

The detailed Ca^{2+} dynamics model adopted from the starting model included a single Ca^{2+} extrusion mechanism which was kept intact, the two Ca^{2+} binding proteins Parvalbumin and

Calbindin D28k that were corrected to account for differences in temperature reported in the model and the experiment, a generic fast immobile buffer and the Ca^{2+} indicator used in the experiments. Diffusion was removed from our model since the averaged region recorded in the experiments does not allow its discrimination. The single Ca^{2+} extrusion mechanism is described by the following kinetic scheme:

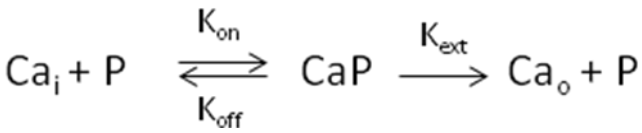

where Ca_i is the intracellular Ca^{2+} concentration, P= 10^{-9} mol/cm^2 is the Ca^{2+} pump density, CaP is an intermediate state, Ca_o is the extracellular Ca^{2+} concentration, and $K_{on} = 3 \cdot 10^{-3}$ $\mu M^{-1} s^{-1}$, $K_{off} = 1.75 \cdot 10^{-2}$ s^{-1}, and $K_{ext} = 7.255 \cdot 10^{-5}$ $\mu M^{-1} s^{-1}$ are rate constants.

Parvalbumin and Calbindin D28k were also adopted from this model following the standard buffering scheme:

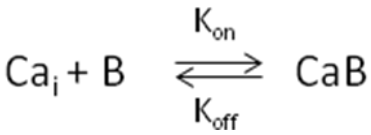

where Ca_i is the intracellular Ca^{2+} concentration, B is the Buffer concentration, CaB is the Ca^{2+} bound to the buffer concentration and K_{on} and K_{off} are the reaction kinetic parameters. Diffusion was removed from the model and therefore the concentration and kinetic parameters of these buffers were corrected to take in account radial diffusion and the different temperature in our experiments. Experiments were performed at 34°C, but the kinetic parameters for Parvalbumin and Calbindin were published at room temperatures. Therefore, their K_{on} was multiplied by a factor of 5 (De Schutter and Bower, 1994). Compensation for buffer diffusion was done by increasing Calbindin concentration by a factor of 4.

Parvalbumin has two binding sites and a medium affinity to Mg^{2+}. The empirical values of the concentration and kinetic parameters reported were corrected assuming a near physiological temperature and also for the number of binding sites (two per molecule) B = 150 µM, K_{on}^{Ca} = 535 $\mu M^{-1} s^{-1}$, K_{off}^{Ca} = 0.95 s^{-1}, K_{on}^{Mg} = 4 $\mu M^{-1} s^{-1}$ and K_{off}^{Mg} = 525 s^{-1}.

Calbindin D28k has four binding sites, two fast and two slow. The empirical values of the concentration and kinetic parameters reported where corrected to take in account radial

diffusion and the difference in temperature. The fast binding sites concentration (two per molecule) B_{fast} = 1.2 mM, K_{on}^{f} = 217.5 $\mu M^{-1}s^{-1}$, K_{off}^{f} = 35.8 s^{-1} and the slow binding sites concentration (two per molecule) B_{slow} = 1.2 mM, K_{on}^{s} = 27.5 $\mu M^{-1}s^{-1}$ and K_{off}^{s} = 2.6 s^{-1}. In the above model I also introduced an immobile buffer adopted from Ait Ouares et al., (2016) with concentration B = 1 mM, K_{on} = 570 $\mu M^{-1}s^{-1}$ and K_{off} = $5.7 \cdot 10^3$ s^{-1}.

In the reported experiments, two different Ca^{2+} indicators were used, either FuraFF for sequential V_m and Ca^{2+} imaging or OG5N for Ca^{2+} imaging alone. The indicators act as Ca^{2+} buffers as well and so they were also introduced in the model. For FuraFF in the concentration B = 1 mM, K_{on} = 570 $\mu M^{-1}s^{-1}$ and K_{off} = $5.7 \cdot 10^3$ s^{-1}. For OG5N in the concentration B = 2 mM, K_{on} = 570 $\mu M^{-1}s^{-1}$ and K_{off} = $19.95 \cdot 10^3$ s^{-1}. The parameters that did not require tuning after they were calculated were treated as constants in the model (Table 4.1).

Table 4.1: *Buffer concentrations and kinetic parameters*

Parameter	Value	Reference and Notes
Extrusion		Anwar et al 2012
Binding sites concentration	10^{-9} mol/cm^2	
K_{on}	$3 \cdot 10^{-3}$ $\mu M^{-1}s^{-1}$	
K_{off}	$1.75 \cdot 10^{-2}$ s^{-1}	
K_{ext}	$7.255 \cdot 10^{-5}$ $\mu M^{-1}s^{-1}$	
Parvalbumin		Anwar et al 2012
Binding sites concentration	150 µM	
$K_{on,Ca}$	535 $\mu M^{-1}s^{-1}$	Corrected for temperature
$K_{off,Ca}$	0.95 s^{-1}	
$K_{on,Mg}$	4 $\mu M^{-1}s^{-1}$	Corrected for temperature
$K_{off,Mg}$	525 s^{-1}	
Calbindin D28k		Anwar et al 2012
Fast sites concentration	1.2 mM	Corrected for diffusion
$K_{on,fast}$	217.5 $\mu M^{-1}s^{-1}$	Corrected for temperature
$K_{off,fast}$	35.8 s^{-1}	
Slow sites concentration	1.2 mM	Corrected for diffusion
$K_{on,slow}$	27.5$\mu M^{-1}s^{-1}$	Corrected for temperature
$K_{off,slow}$	2.6 s^{-1}	
Immobile Buffer		Ait Ouares et al 2016
concentration	1 mM	
K_{on}	570 $\mu M^{-1}s^{-1}$	
K_{off}	$5.7 \cdot 10^3$ s^{-1}	
OG5N		Canepari and Ogden, 2006
concentration	2 mM	
K_{on}	570 $\mu M^{-1}s^{-1}$	
K_{off}	$19.95 \cdot 10^3$ s^{-1}	
FuraFF		Canepari and Ogden, 2006
concentration	1 mM	
K_{on}	570 $\mu M^{-1}s^{-1}$	
K_{off}	$5.7 \cdot 10^3$ s^{-1}	

4.2 Initial Channel models and free parameters

The next step in constructing the model was to introduce active membrane properties. The choice of the channels was based on the experimental data of Ait Ouares et al., (2019) where pharmacological analysis revealed the dendritic Ca^{2+} and K^{+} channels activated by the CF-EPSP. Specifically, the channels where the P/Q-type high-voltage activated (HVA) VGCCs, the T-type low-voltage activated (LVA) VGCCs, the A-type LVA-VGKCs and the SK and BK Ca^{2+}-activated K^{+} channels. In addition to these channels I also included a generic HVA-VGKC (HVAK). These channels are known to be present in PN dendrites, but cannot be pharmacologically blocked due to lack of a selective inhibitor.

To build the model, I started with previously published channel models available in the database. However, there are several models for the same channel available in the database and so the choice of the channel model was based on pharmacological studies that also provided us with a coarse-grained approximation of the kinetics of each channel. The channel models from the database that proved able to closely represent the experimental results were included in the simulation and several parameters in their kinetics were set as free tuneable parameters.

The general mathematical equations describing each channel are given in the following section. For most of the used channels the conductance is described by the Hodgkin-Huxley (H-H) scheme (Hodgkin and Huxley, 1952) formalised by the equation below:

$$G(V, \lfloor Ca^{2+} \rfloor, t) = \tilde{g} \cdot \mathrm{m(V,t)^p} \cdot \mathrm{h(V,t)^q} \cdot \mathrm{z(\lfloor Ca^{2+} \rfloor,t)^r}$$

The independent gating parameters n, m, h, z stand for the probability of one gating parameter being in an open state and the probability of the entire gate/channel to be open is the product of these variables raised to a power. The ion current is described by:

$$I = G(V, \lfloor Ca^{2+} \rfloor, t) \cdot (V - E)$$

Where the Nernst potential is computed continuously with the channel considered as a constant resistance and the Goldman-Hodgkin-Katz is initially neglected (Hille 1991). Otherwise, the ion current is described by:

$$I = G(V, \lfloor Ca^{2+} \rfloor, t) \cdot GHK$$

Where GHK is the Goldman-Hodgkin-Katz factor (expressing the current per unit permeability) used to model the rectification of channels.

The SK Ca^{2+}-activated K^+ channel is the only channel in our simulation that is not described by the H-H scheme but by a Markov chain model instead. A **Markov chain** is a memory-less stochastic process where transitions from one state to another happen with a probability that is independent on the past steps (Markov 1906). A Markov chain model of ion channels describes the probability of the entire ion channel being in one of the possible states and one or more of these states may correspond to the ion channel being open. Markov chain models are more accurate but have more parameters, while remaining rough approximations of the actual dynamics. The states and possible transitions between them are represented by a kinetic scheme such as the one shown in the example below

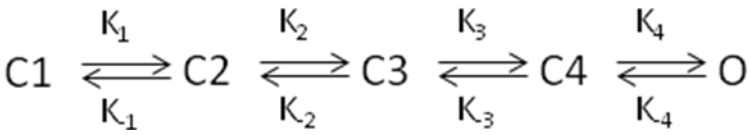

Where $C_{1,2,3,4}$ represent four different closed states of the channel and O one open state. The possible transitions between these states have rate coefficients $K_{1,2,3,4}$. The channel conductance measured in S/cm^2 is then given by the following equation:

$$G = \tilde{g} \cdot O$$

and the current by the equation:

$$I = G \cdot (V - E)$$

The specific equations for each channel are given in the following sections. In these equations, I is the current density (expressed in mA/cm^2), $\prod$ is the channel permeability to Ca^{2+} (expressed in cm/s), $\sum$ is the channel conductance (expressed in S/cm^2), m_∞, t_m, m_{exp} and h_∞, t_h are the voltage-dependent activation and inactivation parameters respectively, z_∞, z_{exp} and t_z are the Ca^{2+}-dependent activation parameters, and GHK is the Goldman-Hodgkin-Katz

factor. Voltage (V) and time are expressed in mV and ms respectively. The free parameters are noted as p1, p2... pn.

4.2.1 P/Q-type VGCC

The P/Q-type Ca^{2+} channel was first described in PNs by Llinas et al. (1989a) as a High-Voltage-Activated (HVA) channel with very slow inactivation. The initial channel model was adopted from Anwar et al. (2012) with kinetics described by the Hodgkin-Huxley (H-H) scheme with three independent activating parameters m and no inactivation. Starting from this formulation, the activation curve was multiplied with a sigmoid function and several values were replaced with free parameters.

$$I = \Pi \cdot m^3 \cdot GHK$$

$$m_\infty = \frac{1}{1 + e^{-(V+29.458)/8.439}} \cdot \frac{1}{1 + e^{-p1 \cdot (V+p2)}}$$

$$t_m = \begin{Bmatrix} p3 \cdot \left(0.2702 + 1.1622 \cdot e^{-\frac{(V+26.798)^2}{164.19}}\right) & if\ V \leq -40mV \\ p3 \cdot 0.6923 \cdot e^{V/1089.372} & otherwise \end{Bmatrix}$$

4.2.2 T-type VGCC

The T-type VGCC is a low-threshold, faster inactivating channel (Hirano and Hagiwara, 1989). The initial channel model was adopted from Anwar et al. (2012) with kinetics described by the Hodgkin-Huxley (H-H) scheme with two independent activating parameters m and one inactivating h. Starting from this formulation, the activation curve was multiplied with a sigmoid function and several values were replaced with free parameters.

$$\mathrm{I} = \Pi \cdot \mathrm{m}^2 \cdot \mathrm{h} \cdot \mathrm{GHK}$$

$$\mathrm{m}_\infty = \frac{1}{1 + e^{-(V+51)/6}} * \frac{1}{1 + e^{-p1 \cdot (V+p2)}}$$

$$h_\infty = \frac{1}{1 + e^{-(\frac{V+72}{7})}}$$

$$t_m = \left\{ \begin{array}{ll} 1 & \text{if } V \leq -90\text{mV} \\ \frac{p3}{e^{(V+40)/9} + e^{-(V+108)/18}} + p4 & \text{otherwise} \end{array} \right\}$$

$$t_h = p5 + \frac{p6}{e^{\frac{V+32}{7}}}$$

4.2.3 A-type VGKC

The A-type VGKC was shown to be present in PNs first by Housnsgaard and Midtgaard (1988). The initial channel model was adopted from De Schutter and Bower (1994) with kinetics described by the Hodgkin-Huxley (H-H) scheme with four independent activating parameters m and one inactivating h. The Nernst potential was computed continuously. Starting from this formulation, the activation curve was multiplied with a sigmoid function and several values were replaced with free parameters.

$$I = \Sigma \cdot h \cdot m^4 \cdot (V + 85)$$

$$m_\infty = \frac{a_m}{a_m + b_m} \cdot \frac{1}{1 + e^{-p1 \cdot (V+p2)}}$$

$$h_\infty = \frac{a_h}{a_h + b_h}$$

$$a_m = \frac{1.4}{1 + e^{-(V+p3)/12}}$$

$$a_h = \frac{0.0175}{1 + e^{(V+p4)/8}}$$

$$b_m = \frac{0.49}{1 + e^{(V+30)/4}}$$

$$b_h = \frac{1.3}{1 + e^{-(V+13)/10}}$$

$$t_m = \frac{1}{a_m + b_m}$$

$$t_h = \frac{1}{a_h + b_h}$$

4.2.4 HVA VGKC

The HVA-VGKC (HVAK) has been reported in several experiments to be responsible for the repolarisation (Hirano and Hagiwara, 1989; Gahwiler and Llano, 1989) but its kinetics are not very well defined since it is not a specific channel but rather a combination of channels and to this day there is no specific toxin to block the activity of this channel. The initial channel model was adopted from De Schutter and Bower, (1994) ("delayed rectifier channel") with kinetics described by the Hodgkin-Huxley (H-H) scheme with two independent activating parameters m and one inactivating h. The Nernst potential was computed continuously. Starting from this formulation, the activation curve was multiplied with a sigmoid function and several values were replaced with free parameters.

$$I = \Sigma \cdot h \cdot m^2 \cdot (V + 85)$$

$$m_\infty = \frac{a_m}{a_m + b_m} \cdot \frac{1}{1 + e^{-p1 \cdot (V+p2)}}$$

$$h_\infty = \frac{1}{1 + e^{(V+25)/4}}$$

$$a_m = \frac{-0.0047 \cdot (V - 8)}{-0.9999 + e^{-(V-8)/12}}$$

$$b_m = e^{-(V+127)/30}$$

$$t_m = \frac{p3}{\frac{-0.0047 * (V + 12)}{-0.9999 + e^{-(V+12)/12}} + e^{-\frac{V+147}{30}}}$$

$$t_h = \begin{cases} 1200 \text{ if } V < -25 \\ 10 \text{ otherwise} \end{cases}$$

4.2.5 BK Ca^{2+}-activated K^+ channel

The BK Ca^{2+}-activated K^+ channels are large conductance channels (B in 'BK' corresponding to Big) and have been reported to be responsible for the repolarisation of dendritic Ca^{2+} spikes (Latorre et al., 1989). This channel is characterised by its Voltage and Ca^{2+} dependence and has been shown to be coupled with P/Q channels in Purkinje Neuron dendrites. The selective coupling is achieved by their proximal localization to these Ca^{2+} channels. Because P/Q-type VGCC are the primary source of Ca^{2+} activating BK channels, the kinetics and voltage dependence of activation of the BK Ca^{2+}-activated K^+ channel will depend on those of the P/Q-type VGCC (Womack et al., 2004). The initial channel model was adopted from De Schutter and Bower (1994), with kinetics described by the Hodgkin-Huxley (H-H) scheme with two independent state variables, one m descibing the voltage-dependency and two z for the Ca^{2+} dependency. Starting from this formulation, three free parameters were introduced.

$$I = \Sigma \cdot m \cdot z^2 \cdot (V + 85)$$

$$m_\infty = \frac{p1}{7.5 + a_m}$$

$$z_\infty = \frac{1}{1 + \frac{p3}{[Ca^{2+}]}}$$

$$a_m = \frac{0.11}{e^{(V-p2)/14.9}}$$

$$t_m = \frac{1}{7.5 + a_m}$$

$$t_z = 4$$

4.2.6 SK Ca^{2+}-activated K^+ channel

The SK Ca^{2+}-activated K^+ channels are small conductance channels (S in 'SK' corresponding to Small). This channel is characterised by its Ca^{2+} dependence alone and has been shown to be coupled with T-type VGCC in Purkinje Neuron dendrites (Cueni and Canepari, 2009; Stocker, 2004; Swensen and Bean, 2003). The initial channel model was adopted from Solinas et al., 2008 with kinetics described by a Markov chain model instead of a Hodgkin-Huxley (H-H) scheme. Four different closed states and two open states where modelled. The Ca^{2+} dependent rates are K_1 = 200 $ms^{-1}mM^{-1}$, K_2 = 160 $ms^{-1}mM^{-1}$and K_3 = 80 $ms^{-1}mM^{-1}$. The Ca^{2+} independent rates are K_4 = 1.2 ms^{-1}, K_5 = 160e-3 ms^{-1}, K_{-1} = 80e-3 ms^{-1}, K_{-2} = 80e-3 ms^{-1}, K_{-3} = 200e-3 ms^{-1}, K_{-4} = 100e-3 ms^{-1}, K_{-5} = 1 ms^{-1} according to the following kinetic scheme:

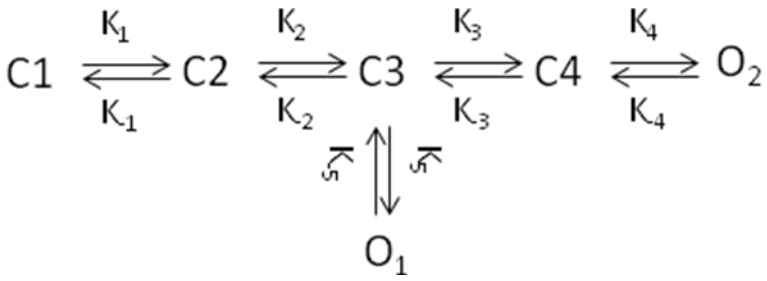

The current is given by the equation:

$$I = \Sigma \cdot (O_1 + O_2) \cdot (V + 85)$$

4.3 Model of the CF-associated current

The model of the current associated with a CF-EPSP, designed to mimic the shape of the current reported by Llano et al. (1991), was expressed by the equation:

$$I_{CF} = I_{HOLD} + I_{STANDING} \cdot \left(1 - e^{-(t-DELAY)/RISE}\right) \cdot e^{-(t-DELAY)/DURATION}$$

Where I_{HOLD} is the holding current before CF-EPSP occurrence that holds the V_m at the different initial V_m: hyperpolarized (~-80 mV), intermediate (~-65 mV) and depolarized (~-50 mV). $I_{STANDING}$ is the peak current evoked by the CF-EPSP and has a linear relation with V_m. DELAY is set by the actual experimental delay where the CF stimulation occurred 2 ms after the beginning of each trial. In the simulation, the value of DELAY varied between 2 and 2.4 ms between different cells, a variation attributed to the distance of the recorded site from the site of CF contacts. DELAY also slightly varied by ±0.1 ms between different states of the same cell in some cases since this is the variability of experimental jitters in recordings performed at 5 kHz. RISE depends on the characteristics of the synaptic current but also on the distance from the site of origin so it can significantly differ from cell to cell and slightly between two states of the same cell. DURATION also depends on the characteristics of the synaptic current and the distance from the site of origin but unlike the rising time, it also highly depends on the initial V_m. DURATION increases as the V_m is held at more positive values. The parameters in this equation were tuned accordingly to obtain the match of experimental V_m and Ca^{2+} transients.

4.4 Parameters of the channel kinetics

The final stages of constructing the channel models involved tuning the CF-current parameters, channel densities and the free parameters set in the previous section in the channel kinetics. The initial tuning of the model was done based on the experimental V_m and Ca^{2+} transients of a single cell. Starting from the initial models for the channels adopted from the database and estimations about the CF-associated current, the set of the free parameters was tuned to obtain traces from the simulation that matched the experimental V_m and Ca^{2+} optical measurements from ~17X17 μm^2 square regions at the three different initial V_m's.

After obtaining a satisfactory set of models for each channel in one cell, the same channel models were used to match the experimental data in three more cells, only by tuning the channel densities and the current input associated with the CF-EPSP. The following sections describe the modifications made to match the experimental results and the final mathematical functions for each ion channel. Figure 4.2 summarizes the kinetics of the voltage-gated Ca^{2+} and K^+ channels with curves of steady-state activation and inactivation (when included in the model) as well as their time constants with respect to voltage.

4.4.1 P/Q-type VGCC

The P/Q-type Ca^{2+} channel from Anwar et al. (2012) with kinetics described by the Hodgkin-Huxley (H-H) was modified by multiplying the activation curve by a sigmoid function to account for the fact that we did not observe P/Q channel activation below -50 mV. We also reduced the activation time by 40% to reproduce the observed Ca^{2+} spiking rate at depolarised states.

$$I = \Pi \cdot m^3 \cdot GHK$$

$$m_\infty = \frac{1}{1 + e^{-(V+29.458)/8.439}} \cdot \frac{1}{1 + e^{-0.1 \cdot (V+50)}}$$

$$t_m = \begin{cases} 0.6 \cdot \left(0.2702 + 1.1622 \cdot e^{-\frac{(V+26.798)^2}{164.19}}\right) & if\ V \leq -40mV \\ 0.6 \cdot 0.6923 \cdot e^{V/1089.372} & otherwise \end{cases}$$

4.4.2 T-type VGCC

The T-type VGCC from Anwar et al. (2012) with kinetics described by the Hodgkin-Huxley (H-H) scheme was modified by multiplying the activation curve by a sigmoid function to account for the observed activation at hyperpolarised and intermediate states. The activation time was decreased by 70% while the inactivation time was doubled to fit the rise and decay of the experimental V_m trace at the hyperpolarised state.

$$I = \Pi \cdot m^2 \cdot h \cdot GHK$$

$$m_\infty = \frac{1}{1 + e^{-(V+51)/6}} * corr$$

$$corr = \begin{cases} \frac{1}{1 + e^{-0.3 \cdot (V+53)}} & \text{at hyperpolarised states} \\ \frac{1}{1 + e^{-0.3 \cdot (V+45)}} & \text{at intermediate states} \end{cases}$$

$$h_\infty = \frac{1}{1 + e^{-(\frac{V+72}{7})}}$$

$$t_m = \left\{ \begin{array}{c} 1 \quad \text{if } V \leq -90\text{mV} \\ \frac{0.2}{e^{(V+40)/9} + e^{-(V+108)/18}} + 0.3 \ \text{otherwise} \end{array} \right\}$$

$$t_h = 32 + \frac{2}{e^{(V+32)/7}}$$

4.4.3 A-type VGKC

The A-type VGKC from De Schutter and Bower (1994) with kinetics described by the Hodgkin-Huxley (H-H) scheme, was modified in line with modifications of T-type VGCCs to account for behaviours at hyperpolarised states. The density was corrected at intermediate states to account for partial inactivation.

$$I = \Sigma \cdot h \cdot m^4 \cdot (V + 85)$$

$$m_\infty = \frac{a_m}{a_m + b_m} \cdot \frac{1}{1 + e^{-0.2 \cdot (V+50)}}$$

$$h_\infty = \frac{a_h}{a_h + b_h}$$

$$a_m = \frac{1.4}{1 + e^{-(V+50)/12}}$$

$$a_h = \frac{0.0175}{1 + e^{(V+85)/8}}$$

$$b_m = \frac{0.49}{1 + e^{(V+30)/4}}$$

$$b_h = \frac{1.3}{1 + e^{-(V+13)/10}}$$

$$t_m = \frac{1}{a_m + b_m}$$

$$t_h = \frac{1}{a_h + b_h}$$

4.4.4 HVA VGKC

The HVA-VGKC (HVAK) from De Schutter and Bower (1994) ("delayed rectifier channel") with kinetics described by the Hodgkin-Huxley (H-H) scheme was modified to account for the behaviours at depolarised states. Specifically, the activation curve was multiplied by a sigmoid function to track the occurrence of the first Ca^{2+} spike. Then the activation time was decreased by ~95% to reproduce the number and shape of the observed Ca^{2+} spikes.

$$I = \Sigma \cdot h \cdot m^2 \cdot (V + 85)$$

$$m_\infty = \frac{a_m}{a_m + b_m} \cdot \frac{1}{1 + e^{-0.4 \cdot (V+35)}}$$

$$h_\infty = \frac{1}{1 + e^{(V+25)/4}}$$

$$a_m = \frac{-0.0047 \cdot (V - 8)}{-0.9999 + e^{-(V-8)/12}}$$

$$b_m = e^{-(V+127)/30}$$

$$t_m = \frac{0.055}{\frac{-0.0047 * (V + 12)}{-0.9999 + e^{-(V+12)/12}} + e^{-\frac{V+147}{30}}}$$

$$t_h = \begin{cases} 1200 \text{ if } V < -25 \\ 10 \text{ otherwise} \end{cases}$$

4.4.5 BK Ca^{2+}-activated K^+ channel

The BK Ca^{2+}-activated K^+ channels from De Schutter and Bower (1994) were modified by reducing the Ca^{2+} dependent activation time to about half to account for the larger slow repolarisation at depolarised states.

$$I = \Sigma \cdot m \cdot z^2 \cdot (V + 85)$$

$$m_\infty = \frac{8.5}{7.5 + a_m}$$

$$z_\infty = \frac{1}{1 + \frac{0.4}{[Ca^{2+}]}}$$

$$a_m = \frac{0.11}{e^{(V-55)/14.9}}$$

$$t_m = \frac{1}{7.5 + a_m}$$

$$t_z = 4$$

4.4.6 SK Ca^{2+}-activated K^+ channel

The SK Ca^{2+}-activated K^+ channels from Solinas et al. (2008) with kinetics described by Markov models instead were not modified in terms of kinetic parameters but we set 95% of the SK channels coupled to T-type VGCCs to account for effect of blocking these channels observed exclusively at hyperpolarised states.

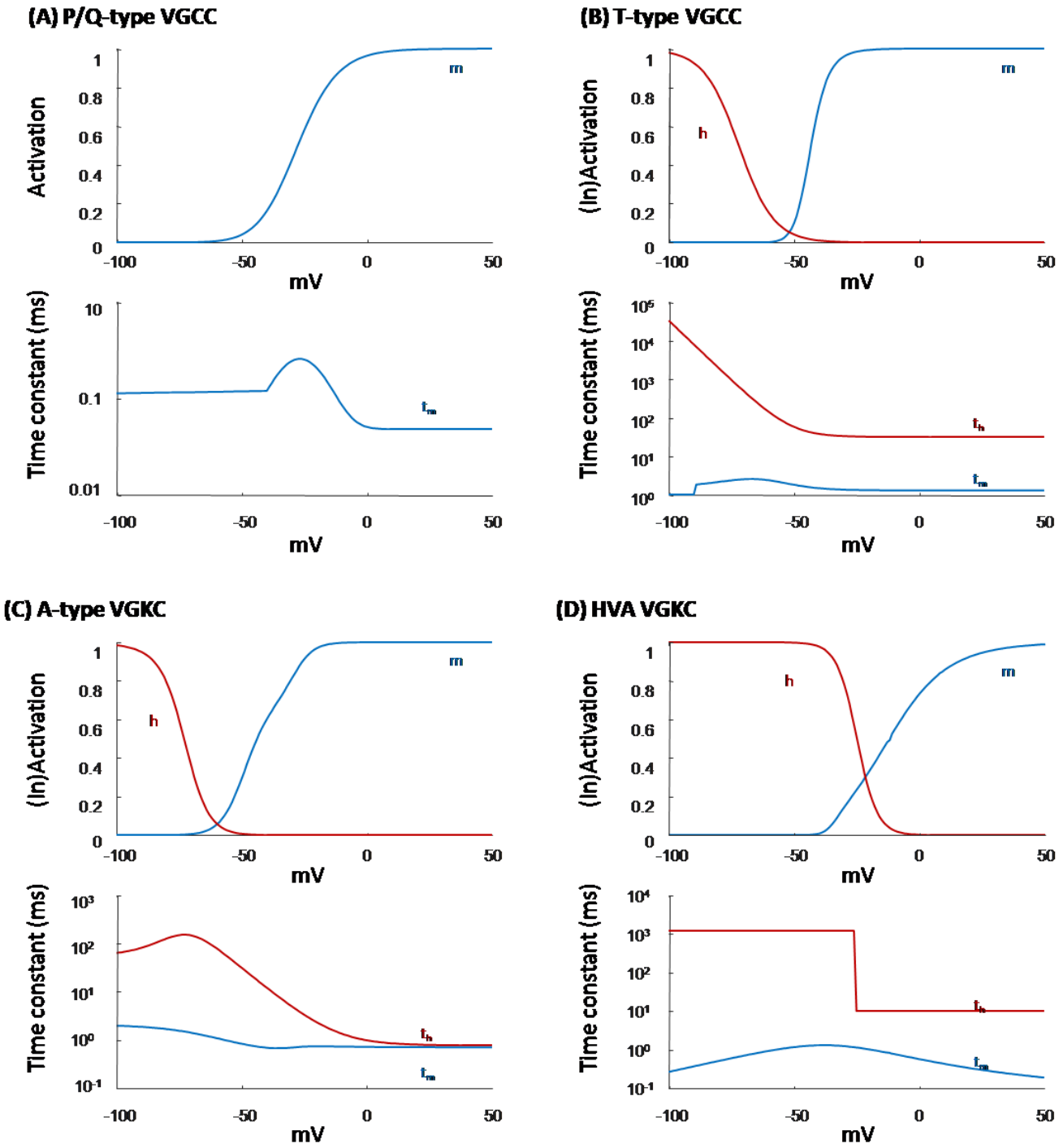

Figure 4.2: *Steady-state activation (m) and inactivation (h) and time constants of activation (t_m) and inactivation (t_h) vs. Voltage in mV. Time constants are plotted on a semilogarithmic scale. (A) P/Q-type VGCC. (B) T-type VGCC. (C) A-type VGKC.*

4.5 Tuning the model to reproduce the experimental data

Having established a satisfactory set of models for each channel in one cell, the same channel models were used to match the experimental data in three more cells to extrapolate individual dendritic ion currents underlying V_m transients and Ca^{2+} signals associated with CF-EPSPs at different V_m initial states. Four dendritic sites from four different PNs were selected with the criteria that the somatic resting V_m and the CF-EPSP, at different initial V_m, were stable for the entire duration of the recordings, in order to assume the same conditions for the V_m and Ca^{2+} recordings.

The parameters in the CF current equation were tuned to obtain a match between the experimental V_m and Ca^{2+} transients within the following ranges: I_{HOLD}: between -0.03 and 0.04 mA/cm^2, $I_{STANDING}$: between -0.4 and -0.1 mA/cm^2, DELAY: between 2 and 2.4 ms, RISE: between 0.4 and 1.8 ms and DURATION: between 2.5 and 6 ms. As representative example, the CF-current parameters for the three initial V_m of the first cell are given in Table 4.2.

The channel conductances were also tuned to obtain the match of experimental V_m and Ca^{2+} transients as shown in Table 4.3 for each cell and state.

The conductance of the P/Q-type, the HVAK and the BK-type channels was constant in all states of each cell while the conductance of the T-type, A-type and SK-type channels needed adjustments at each state to account for different experimental observations.

For the T-type and A-type channels, the concentration at depolarised states was set to 0 to account for no observed effect when blocking these channels.

For the A-type channels the density was also corrected at intermediate states to account for partial inactivation.

The concentration of SK channels decreased with hyperpolarised to depolarised states in line with the T channel. This represents roughly 95% of the SK channels coupled to T-type VGCCs to account for the observation that blocking these channels has an effect exclusively at hyperpolarised states.

Only channel conductance and CF current parameters were altered until the model was able to reproduce the experimental V_m and Ca^{2+} transients of each cell at the three different initial V_m. The direct comparison between experimental and simulated traces is shown in Figure 4.3.

Table 4.2: *CF-associated current parameters*

Parameter	Hyperpolarised	Intermediate	Depolarised
I_{HOLD}	0.044	0.004	-0.031
I_{STAND}	-0.4	-0.32	-0.15
DELAY	2.2	2.2	2.1
RISE	1.4	1.4	1
DURATION	3	4.8	5.3

Table 4.3: *Channel conductances at each state*

	P/Q (cm/s)	**T (cm/s)**	**A (S/cm^2)**	**HVAK (S/cm^2)**	**BK (S/cm^2)**	**SK (S/cm^2)**
Hyp						
Cell 1	0.00075	0.00015	0.07	0.032	2.5	0.03
Cell 2	0.00085	0.00014	0.12	0.029	3	0.03
Cell 3	0.00095	0.00018	0.1	0.034	2	0.03
Cell 4	0.00068	0.00012	0.07	0.035	4	0.04
Int						
Cell 1	0.00075	0.00015	0.19	0.032	2.5	0.008
Cell 2	0.00085	0.00014	0.032	0.029	3	0.008
Cell 3	0.00095	0.00018	0.027	0.034	2	0.008
Cell 4	0.00068	0.00012	0.19	0.035	4	0.01
Dep						
Cell 1	0.00075	0	0	0.032	2.5	0.001
Cell 2	0.00085	0	0	0.029	3	0.001
Cell 3	0.00095	0	0	0.034	2	0.001
Cell 4	0.00068	0	0	0.035	4	0.0012

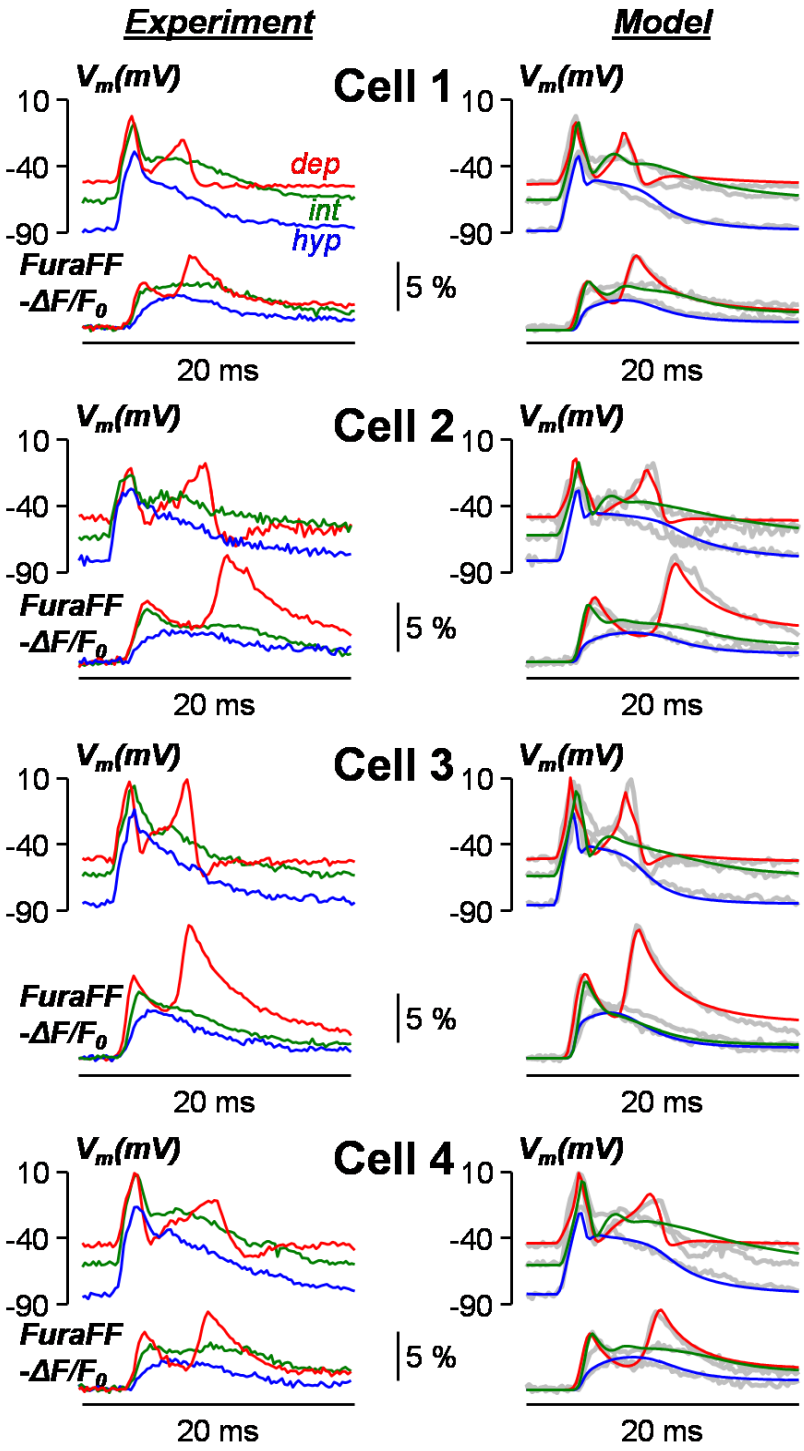

Figure 4.3: *Neuron model of four PN dendritic compartments reproducing V_m and Ca_{2+} transients associated with the CF-EPSP. Left: Experimental dendritic V_m and Ca_{2+} transients associated with the CF-EPSPs from four selected cells at three different initial V_m: hyperpolarized (hyp, blue trace), intermediate (int, green trace) and depolarized (dep, red trace). Right: Simulations of dendritic V_m and Ca^{2+} transients associated with CF-EPSPs reproducing experimental data (gray traces)*

4.6 Validation of the model

To validate the consistency of the four variants of the model, we run computer simulations by modelling the replacement of 1 mM Fura-FF with 2 mM OG5N and analysed Ca^{2+} signal modifications produced by the elimination of 90% of each channel, in this way mimicking the experiments in which individual channels were pharmacologically blocked. As an example, the results for the model variant of cell 1 in Figure 4.3 are reported in Figure 4.4, showing that 90% reduction in the density of each channel qualitatively reproduced the experimental behaviour observed after toxin or drug inhibition (see our paper Ait Ouares, Filipis et al., 2019).

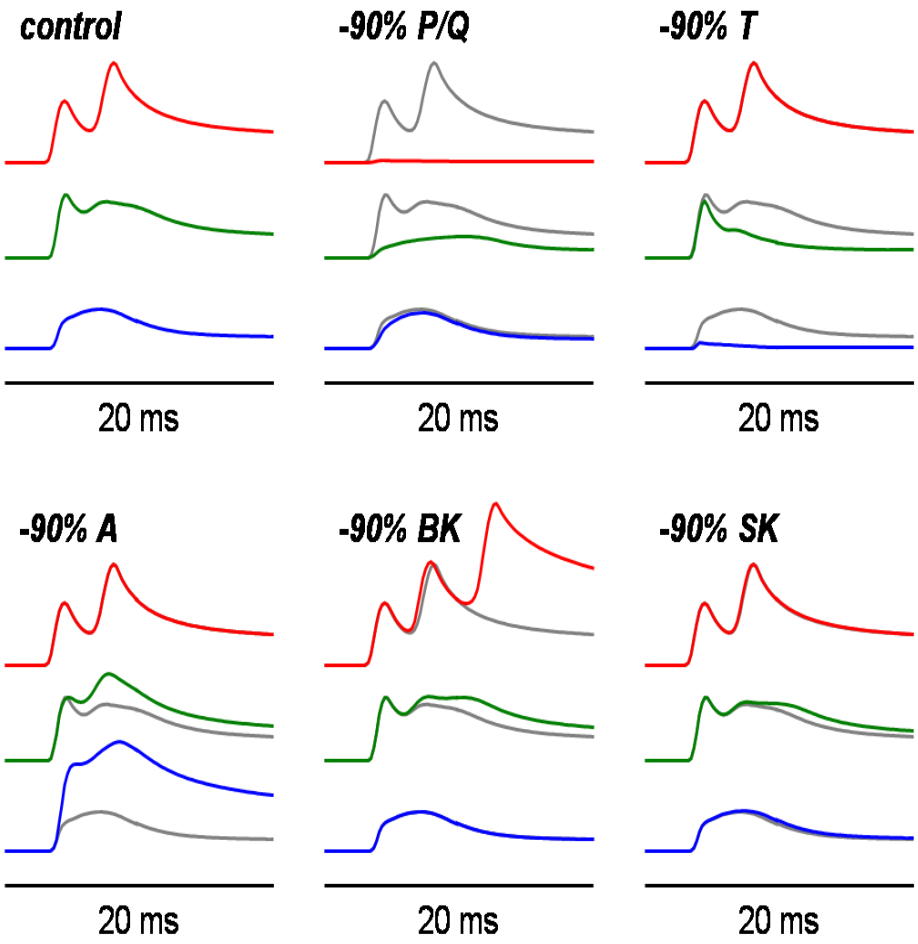

Figure 4.4: *Simulation of Block of channels in the NEURON model. Simulated Ca^{2+} transients (OG5N) associated with CF-EPSPs at three different initial V_m in control condition and after reduction of 90% of one individual channel from Cell1 model variant. For each case, the control trace is shown in gray.*

In order to compare experiments and simulations, we calculated the percentage of the 1st peak and the 2nd peak of the Ca^{2+} transient after elimination of 90% of each channel. The comparisons, reported in Table 4.4, indicate that the observed effects on Ca^{2+} signals in the experiments are all in line with the predictions from the simulations. In addition, in all 4 variants of the model, the 90% reduction of BK channels reproduced the appearance of a third Ca^{2+} spike that was also observed in experiments. In summary, matching experimental data with NEURON simulations generated a simplified yet biological plausible dendritic model that successfully reproduced the complexity of experimental signals.

Table 4.4: *Comparison of the percentage of the control Ca^{2+} transient produced by the pharmacological block of a channel type in the experimental data and with the percentage of the control Ca^{2+} transient produced by the elimination of 90% of the channel in the model*

Channel block		*Hyp*		*Int*		*Dep*	
		1st peak	2nd peak	1st peak	2nd peak	1st peak	2nd peak
PP/Q	+1 µM AgaIVA	50 ± 24*	90 ± 30	25 ± 12*	61 ± 31	10 ± 5*	6 ± 4
	-90% Model	***74±2***	***92±3***	***13±2***	***22±6***	***6±2***	***4±1***
TT	+5 µM ML+30 µM NNC	52 ± 24*	21 ± 9*	94 ± 8	45 ± 15*	100 ± 4	99 ± 11
	-90% Model	***19±3***	***12±2***	***89±3***	***90±3***	***100***	***100***
AA	+1 µM AmmTx3	151 ± 34*	187 ± 44*	114 ± 8*	160 ± 33*	102 ± 4	102 ± 5
	-90% Model	***247±39***	***281±34***	***104±2***	***180±68***	***100***	***100***
BBK	+1 µM Iberiotoxin	97 ± 5	99 ± 5	98 ± 3	98 ± 4	98 ± 9	106 ± 5
	-90% Model	***100±0.08***	***101±0.2***	***100±0.1***	***100±0.1***	***101±0.4***	***117±18***
SSK	+1 µM Apamin	101 ± 9	101 ± 10	100 ± 8	99 ± 6	103 ± 7	97 ± 8
	-90% Model	***100±0.1***	***101±0.2***	***100±0.03***	***100±0.01***	***100±0.02***	***103±5***

4.7 Extraction of channel currents

We then used the model variant of cell 1 to extrapolate the kinetics of each channel contributing to the CF-mediated signal under different conditions (Figure 4.5). At hyperpolarised state (blue traces), the depolarisation transient carried by the CF-EPSP activates a robust Ca^{2+} current, mediated by T-type channels, and a K^+ current, mediated by A-type channels. A very small K^+ current mediated by SK channels is elicited by the transient Ca^{2+} elevation. P/Q-type VGCCs and HVAK VGKSs are barely activated in this state. As the initial V_m becomes more positive (intermediate state, green traces), part of T-type and A-type channels become inactivated, reducing the associated currents and allowing more P/Q and HVAK channels to activate. Finally, at depolarised state (red traces), T-type and A-type channels are fully inactivated and the depolarisation transient carried by the CF-EPSP activates a Ca^{2+} current, mediated by P/Q-type Ca^{2+} channels, and a K^+ current, mediated by HVAK channels, which are responsible for multiple Ca^{2+} spikes. The number of spikes is limited by the K^+ current mediated by BK channels. The strong activation of P/Q-type VGCCs and HVAK VGKCs is prevented at hyperpolarized states by the K^+ current mediated by A-type VGKCs. Hence, when A-type channels are reduced by 90% (purple traces), activation of P/Q-type VGCCs is strongly enhanced, substantially increasing the dendritic Ca^{2+} transient. In summary, by extrapolating the kinetics of individual Ca^{2+} and K^+ channels, we resolved their functional interaction establishing a specific role of A-type VGKCs in controlling activation of P/Q-type channels, HVAK channels and BK channels.

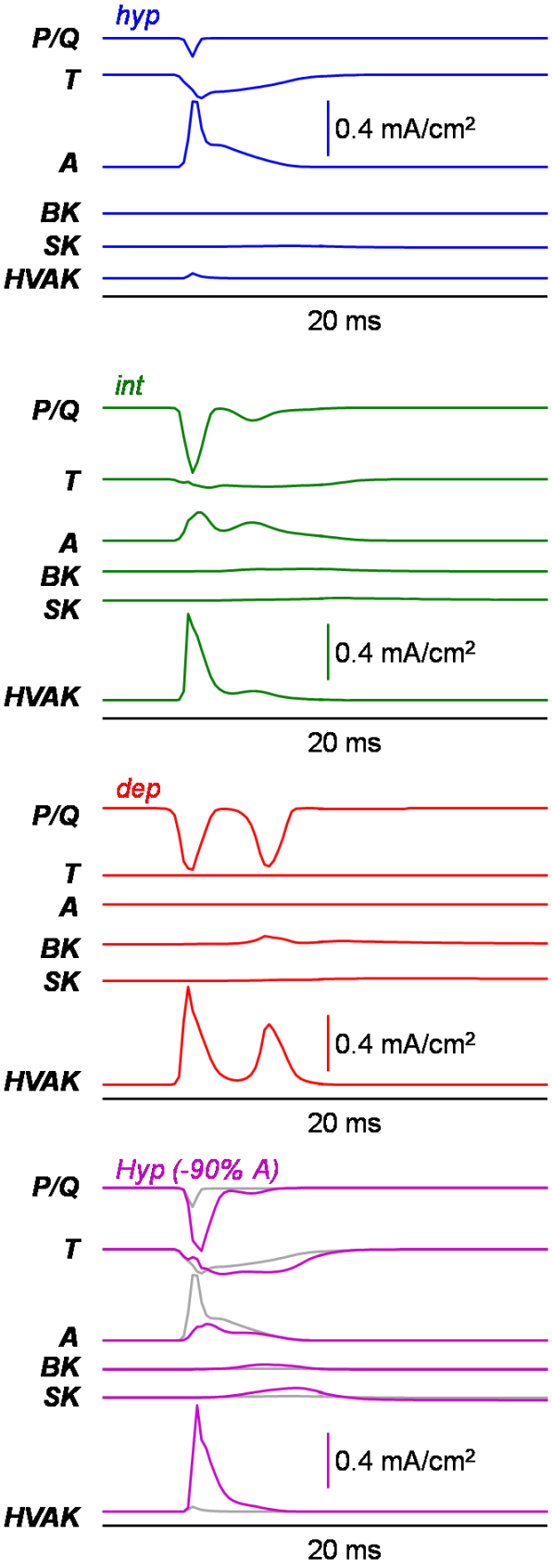

Figure 4.5: *Individual currents extracted from the NEURON model. Ca^{2+} currents of P/Q and T type channels and K^{+} currents of A, BK, SK and the HVA channels from the simulation of cell1 model variant. Simulations were at hyperpolarized (blue traces), intermediate (green traces) and depolarized (red traces) states in control conditions and at the hyperpolarized (purple traces) after blocking 90% of A-type VGKCs superimposed to currents in control conditions (gray traces).*

4.8 Importance of CF-activated channels and of this novel approach

In this chapter, I reported a procedure to extrapolate the kinetics of six channels in parallel. This was achieved using the rich information from experimentally combined V_m and Ca^{2+} imaging and a single compartment model that accurately matches experimental data. Interestingly, for the four stable cells that were used for this analysis, the matching models were obtained using the same kinetic models of the six channels with relatively small variations in conductance densities only. Using this strategy, which combines fast imaging techniques, pharmacological analysis and biophysical modelling, the precise kinetics of dendritic Ca^{2+} and K^+ channel activation in PNs during CF-EPSPs under different V_m conditions were unravelled. In particular, a clear role for the A-type VGKC in limiting the membrane depolarisation and the activation of P/Q-type VGCCs was established. In addition, it is clear that two different sets of channels are selectively activated at different initial V_m.

When the dendrite is hyperpolarised (V_m ~ -80 mV), the transient depolarisation, produced by the CF-EPSP invading the dendritic branch, activates T-type VGCCs (Isope et al., 2012) which in turn enhances the distal dendritic V_m depolarisation produced by the spread of the EPSP. The dendritic V_m, however, is capped below ~10 mV by the K^+ current via A-type VGKCs, thereby limiting the opening of HVA Ca^{2+} and K^+ channels. In this situation, Ca^{2+} influx activates SK channels (Hosy et al., 2011) which regulates V_m repolarisation and appears selectively linked to T-type VGCCs, presumably by molecular coupling (Stocker, 2004).

In contrast, when the dendrite is depolarised (V_m ~ -50 mV), both T-type VGCCs and A-type VGKCs are inactivated and the CF-EPSP can drive the dendrite to more positive V_m values that activate first P/Q-type VGCCs (Usowicz et al., 1992) and subsequently HVAKs, leading to Ca^{2+} spikes. In this situation, Ca^{2+} influx activates BK channels (Rancz and Häusser, 2006), which in turn enhances V_m repolarisation, thereby limiting the number of Ca^{2+} spikes. HVAKs include Kv3.3 which is highly expressed in PNs (Goldman-Wohl et al., 1994) and are involved in regulating dendritic Ca^{2+} spikes (Zagha et al., 2010; Veys et al., 2013). However, the lack of a selective channel blocker for this VGKC didn't permit the experimental assessment of the kinetics of this channel and therefore we cannot exclude a possible contribution of other VGKCs with similar biophysical properties. The role of BK channels is to dampen the generation of Ca^{2+} spikes, which are typically only two when these

channels are active. Finally, significant activation of both sets of channels occurs only at intermediate initial V_m (~ -65 mV).

In summary, The CF-evoked dendritic Ca^{2+} influx is mediated by two VGCCs that exhibit two different activation kinetics and that are presumably associated with two distinct molecular pathways. In particular, P/Q-type VGCCs are believed to trigger endocannabinoid release and short-term synaptic depression (Rancz and Häusser, 2006). The scheme of activation of the two distinct sets of functionally-coupled channels is illustrated in Figure 4.6.

The scheme in Figure 4.6 also shows the effect of blocking or inactivating A-type VGKCs. As these channels prevent the activation of the second set of channels when the dendrite is hyperpolarised, the modulation of this channel by synaptic transmission may provide a mechanism for triggering CF non-linear behaviour which may play a role in associative plasticity. Indeed, it has been shown that A-type VGKCs are modulated by type-1 metabotropic glutamate receptors (Otsu et al., 2014) and this mechanism can play a role when the CF-EPSP is concomitant with PF activation. A-type VGKCs can also be rapidly inactivated by depolarisation produced by excitatory postsynaptic potentials, driving the dendrite to a depolarised state. This mechanism occurs in the dendrites of CA1 hippocampal pyramidal neurons where inactivation of A-type VGKCs by Schaffer collateral EPSPs leads to the boosting of backpropagating action potentials, a mechanism playing a role in Hebbian plasticity at the same synapses (Magee and Johnston, 1997).

While A-type VGKCs can act as a functional trigger of synaptic plasticity, these channels can be potentially the target of meta-plasticity mechanisms to regulate dendritic functions, in particular with respect to membrane excitability. In CA1 hippocampal pyramidal neurons, coupling between local dendritic spikes and the soma can be modified in a branch-specific manner through regulation of dendritic A-type K^+ channels, a phenomenon that allows spatio-temporal correlation of synaptic inputs (Losonczy et al., 2008). In the cerebellum, this phenomenon occurs in the case of long-term potentiation of mossy fibre inputs to granule cells (Rizwan et al., 2016).

Our approach can add in the understanding of synaptic behaviour of ion channels since voltage-gated and Ca^{2+}-activated ion channels shape the integration of incoming inputs in dendritic compartments and determine the pattern of V_m and Ca^{2+} influx (Magee and Johnston, 2005). In particular, each ion channel contributes to the V_m transient that in turn regulates the state of the channel (open, close or inactivated). This patterning of mutual interactions determines a global synergy with sets of distinct channels that are functionally coupled. Hence, the understanding of dendritic integration relies on the precise reconstruction

of the kinetics of all principal channels underlying the response of a dendritic compartment to a given physiological input. This concept also applies to abnormal dendritic behaviours associated with channelopathies, such as the reported cases in Fragile X syndrome (Zhang et al., 2014; Brager and Johnston, 2014). Yet, the direct measurement of diverse ionic currents, mediated by different ions, is beyond available experimental techniques.

In the last few years, techniques to directly measure the kinetics of VGCC-mediated Ca^{2+} currents in the dendrites of CA1 hippocampal pyramidal neurons (Jaafari et al., 2014; Jaafari et al., 2015; Jaafari and Canepari, 2016) and PNs (Ait Ouares et al., 2016) were introduced, starting with high-temporal resolution Ca^{2+} imaging. In the present work we used an alternative strategy to indirectly extract all the Ca^{2+} and K^+ currents underlying the CF-mediated signals applied to the same type of recordings, combined with V_m imaging, using the NEURON simulation environment (Hines and Carnevale, 1997). This novel approach allowed the reconstruction of the functional interaction among individual channels, thereby demonstrating the role of A-type VGKCs in controlling the activation of P/Q-type VGCCs. For the first time, it was possible to obtain the kinetics of several Ca^{2+} and K^+ channels in parallel.

It should be highlighted that a single compartment model, or a multi-compartment model with a few compartments, is not a realistic neuronal model of a PN since they don't account neither for the precise morphology of the cell nor for the mechanisms present in small protrusions like dendritic spines. Yet, our approach is based on the concept that fewer parameters allow better constraining of their values when fitting with a set of experimental observations. From the variety of channels, the PN dendritic single compartment appears to be an ideal choice to initially develop this, as it comprises only two VGCCs and no voltage-gated Na^+ channels, which would be the case of several other neuronal systems including cortical and hippocampal pyramidal neurons. In contrast, a complex multi-compartmental model based on thousands of compartments (De Schutter, 1998) can be used to predict general, cell integrative behaviours leading to firing activity, but is not ideal for the precise kinetics of dendritic channels from detailed experimental observations. Precisely reconstructing dendritic or axonal compartments in other systems is possible, in principle, using the same approach by expanding the pharmacological analysis to all channels involved in a signal. For this purpose, the database ModelDB for NEURON simulations already includes over 1100 published models covering more than 130 research topics (McDougal et al., 2017). These models can be used as a starting framework to produce more simplified models with realistic channel kinetics matching the complexity of V_m and Ca^{2+} imaging

experiments at high temporal resolution. The application of this novel approach also concerns the study of alterations induced by mutated proteins associated with channelopathies.

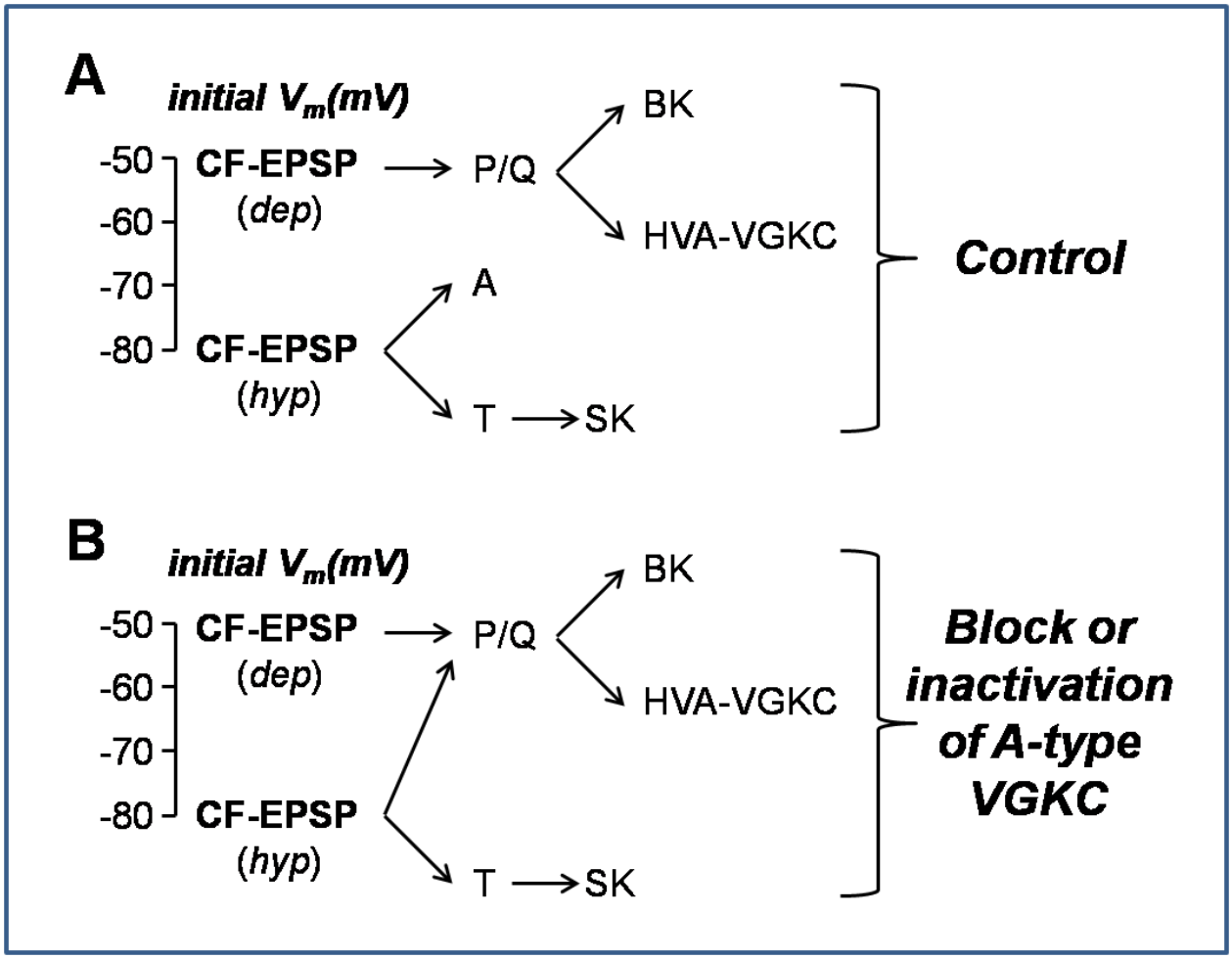

Figure 4.6: *Channel activation following CF-EPSPs at hyperpolarised (hyp) and depolarised (dep) states. (A) In control conditions, at hyp state, the CF-EPSP activates T-type channels, which activate SK channels and A channels which limit the activation of P/Q and HVAK channels. At depolarised states, the CF-EPSP activates P/Q channels, which activate BK channels and HVAK channels.*

Chapter 5. Imaging axonal sodium influx at high spatial and temporal resolution.

The basic principles behind fluorescent Ca^{2+} imaging can in general be applied to other ion species, in particular to Na^{+} imaging. There are however several practical differences between these two imaging techniques. A first important difference is the resting concentration of the two ions in the cytosol. With Na^{+} being over 10000 times more concentrated than Ca^{2+} at rest, changes of sodium concentration take place on a much higher background level compared to changes in calcium concentration (Ross et al., 2014). A second important difference is that once it has entered the cell cytoplasm, Na^{+} is pumped out slowly and does not bind to proteins (i.e. there is no endogenous Na^{+} buffer in the cell). Thus, whereas recording Ca^{2+} is partly aimed at investigating the biochemical activity triggered by a Ca^{2+} signal, recording Na^{+} signals is achieved principally to monitor the activity of Na^{+}-permeable channels. In particular, it is biologically relevant to monitor voltage-gated Na^{+} channels (VGNCs) as they are the main source of inward current responsible for the rising phase of the action potential (Hodgkin and Huxley, 1952), which is the primary signal of inter-neuronal communication.

VGNCs are found in high concentrations in the axon initial segment (AIS) of Layer 5 neocortical pyramidal neurons (Kole et al., 2008),as in most myelinated neurons in the central nervous system. The AIS is the portion of the axon between the axon hillock and the beginning of the myelin sheath (Deiters, 1865), where, shown since the early 1950s, action potentials are generated (Araki and Otani, 1955; Coombs et al., 1957; Edwards and Ottoson, 1958). Computational studies also supported these finding (Dodge and Cooley, 1973) first suggesting that the high concentration of Na^{+} channels in the AIS is the reason for a lower threshold for action potential initiation. More recently, the location of the action potential initiation in cortical neurons was further sub localized to the distal part of the AIS (Palmer and Stuart, 2006; Shu et al., 2007a; Meeks and Mennerick, 2007; Kole et al., 2007; Atherton et al., 2008; Schmidt-Hieber et al., 2008; Foust et al., 2010; Palmer et al., 2010; Popovic et al.,2011) at a distance of about 35 µm away from the soma.

Although there is little, if any, controversy about the site of the action potential initiation, a major question in the last decades has been why the AIS, and specifically the distal part, is

the preferred location for action potential initiation. Several mechanisms have been proposed to explain the preferential site of action potential initiation, either separately or cooperatively: (i) The AIS has a higher local density of Na^+ channels compared to neighboring compartments, which compensates for the large electrical load of the soma (Mainen et al., 199; Wollner and Catteral, 1986; Boiko et al., 2013). (ii) The low threshold of the initial segment has been attributed to the high ratio of source to load (Moore et al., 1983; Mainen et al., 1995; Baranauskas et al., 2012). The high density of Na^+ channels in the AIS providing a large source current which, along with its small axonal diameter, provides the optimal capacitive load and electrical isolation from the soma. (iii) Different Na^+ channel subtypes with different activation thresholds are distributed within different sub compartments of the AIS (Hu et al., 2009; Van Wart et al., 2007; Lorincz and Nusser, 2008; Fleidervish et al., 2010).

The main source of the discrepancies has been the different techniques used in the studies cited above. Cell attached and outside out patch clamp recordings had found similar densities of Na^+ channels in the AIS and soma (Colbert et al., 1996; Colbert et al., 2002). This was later shown not to reflect the real VGNC density due to the strong anchoring of the Na^+ channels in the AIS to the cytoskeleton which reduces their detection ability or can lead to redistribution of Na^+ channels to other sites (Kole et al., 2008; Nakada et al.,2003). Similarly, recording in blebs (injured axonal parts) also could differ from those in intact axons as channels at these sites could be dislocated from the cytoskeleton and be partially proteolysed. In addition, channels could adopt different properties resulting from the cytoskeleton break and the channel densities could depend on the bleb surface area (Hu et al., 2009; Bradke et al., 2012; Aldrich et al., 1987). On the other hand, immunocytochemical techniques can overestimate Na^+ channel density by labeling nonfunctional channel proteins (Kole et al., 2008).

Finally, the Na^+ imaging study of Baranauskas et al., 2012 revealed a Na^+ current density between AIS and soma three times higher as well as a four times increase of Na^+ flux in the middle of the AIS instead of the distal part where initiation occurs, challenging the first proposed mechanism. In support of the third mechanism, the study of Hu et al., 2009 claimed that the low threshold for action potential initiation in the distal AIS was set by the low-threshold Nav1.6 channel found in high densities there. Furthermore, they proposed that the proximal part of the AIS contains an accumulation of the higher threshold Nav1.2 channel, responsible solely for the action potential back propagation. The latter findings were also questioned by Baranauskas et al., 2012 who, using computational models, showed that the

lower activation threshold of the distal Na^+ channels could not be the cause of the lower threshold for action potential initiation in that region. They concluded that the cable properties are the main mechanism underlying the action potential initiation location.

Although the Baranauskas study revealed the main mechanism providing the favourable conditions for the action potential initiation, the spatial and temporal resolution (1 μm and 500 Hz respectively) of the Na^+ imaging measurements were not sufficient to test other contributions such as the lower threshold of Nav1.6 located in the distal AIS. They showed computationally that this lower threshold was not the main factor but could contribute to some extent. Additionally, determining the contribution of the persistent Na^+ current (Fleidervish et al., 2010; Osorio et al.2010) which has been shown to be linked to the Nav1.6 channel (Smith et al., 1998; Burbidge et al., 2002) was beyond the limitations of their imaging technique.

Apart from the initiation site of the action potential, several properties of the action potential are important for neuronal signaling. Properties of the AIS such as length, position and ion channel subunit densities are crucial for the shape of the spike and are independently modulated in the axon and soma by the local distribution of ion channels (Yu et al., 2008; Shu et al., 2007; Kole et al., 2007). Furthermore, VGNCs are thought to be the main determinants of the onset and upstroke of the action potential and cooperative gating of these channels has been suggested to be important for the spike initiation (Brette, 2013; Oz et al., 2015). In addition, it has been suggested that Na^+ channels are distributed throughout the membrane of the AIS in a few μm clusters (Naundorf et al., 2006), but experimental validation of such a theory would require Na^+ imaging with μm range spatial resolution and a few μs temporal resolution. Patch clamp techniques not only do not provide enough spatial resolution, but can also interfere with and change the channel properties. These and many other open questions regarding Na^+ channels in the AIS could be possibly addressed by technological advancements in the optical imaging technique.

In this chapter I present a Na^+ imaging technique using the ANG2 fluorescent Na^+ dye along with the fast Davinci2K CMOS Camera and a power laser source. The spatial resolution of the system at about 0.5 μm per pixel combined with a 10 KHz temporal resolution will permit addressing some of the above questions while also allowing for a precise current kinetics extraction. Imaging recordings combined with pharmacological and computational studies of the two Na^+ channels, Nav1.2 and Nav1.6, reported in the AIS of the Layer 5 neocortical pyramidal neuron can yield important insights about their contribution in the spike shape at physiological as well as pathological conditions, since

numerous diseases have been associated with the deregulation of one of these two Na^+ channels (Mingyu et al., 2017; Sugawara et al., 2001; Lauxmann et al., 2013; Meisler and Kearney, 2005).

5.1 Quantitative evaluation of data from Na^+ imaging experiments.

5.1.1 Spatial and temporal alignment of trials

Na^+ fluorescence was recorded typically for 8 ms at a frame rate of 10 KHz using a partial readout mode (a strip of 30×128 pixels of an 1024X1024 CMOS chip) with a pixel size of ~0,5 µm, resulting from a 0.5X demagnification of the field of view with respect to the configuration used in the experiments reported in Chapter 3.

The analysis and the display of data were carried out using Matlab. In most cases, 2-6 trials were averaged to increase the SNR. Only trials where the difference in the duration of the electrically recorded AP was less than 0.2 ms (two frames) were averaged, after correction for the temporal jitter, using a custom written signal alignment function in Matlab. This control was important as sequential light exposure ultimately provokes photodamage, resulting in an increase in the duration of the action potential due to phototoxicity. Therefore the data reported in this study are exclusively the measurements in which the shape of the electrically recorded action potential did not change during the repetitive light exposures. Furthermore, Matlab was used for spatial corrections for aligning images to compensate for possible small lateral movements of the preparation.

The same focus of the images in the z-dimension was verified after each individual trial and small adjustments were made when necessary. Only trials that were spatially and temporally aligned were averaged, otherwise single trials were used. After acquiring all trials, direct measurement of the photo bleaching effect was measured from a recording with no stimulation. The bleach recording was also checked for lateral movements and aligned with the signal trials when necessary.

5.1.2 Image analysis, spatial averaging and bleach correction

The fractional fluorescence change ($\Delta F/F_0$) depends on the background fluorescence. When this is not negligible it needs to be corrected. For that purpose, the average background fluorescence intensity, determined from an unstained area on the slice, was subtracted from the raw images of both the signal and the bleach recordings.

To simplify the analysis process, a freehand mask was drawn around the axon, out of which all values were set to zero (Figure 5.1B). Each of the 30 pixel lines was then reduced into a 1 x 128 line by averaging since we were interested only in the analysis of Na^+ signals along the axon. Each of the 128 pixels along the axon was then averaged using a Gaussian weight applied on the pixel of interest and 4 pixels left and right (9 pixels in total), as shown in Figure 5.1C, following the equation below:

$$G(x) = \sum_{j=1}^{9} \frac{F(j)}{\sqrt{3\pi}} \cdot e^{-\frac{1}{3}(j-x)^2}$$

Where F(j) is the fluorescence at each of the 9 pixels and G(x) is the new, averaged, fluorescence at the central pixel.

Each of the newly filtered 128 pixels thus corresponds to a weighted average of 9 X 30 pixels (with the 30 pixels containing values only where there is a neuronal segment). The same process was done in parallel for the bleach recording. Then the $\Delta F/F$ was calculated for each of the 128 pixels. To correct the $\Delta F/F$ from the effect of photo bleaching, the bleach recording was subtracted from the signal. Instead of the actual bleach signal, a fit of it was subtracted, to not introduce additional noise into the data. In order to find the optimal bleach fit that did not introduce artifacts in the signal, I tried several functions such as the mono-exponential, bi-exponential, tri-exponential, zero-phase digital filtering, two term power series and stretched bi-exponential. None of these functions was a good fit for the bleach recording but only the stretched-bi-exponential:

c1*exp(-(x*c2)^c3)+c4*exp(c5*x)+c6

and the tri-exponential:

c1*exp((x*c2))+c3*exp(c4*x)+c5*exp(c6*x)+c7

functions did not introduce visible artifacts into the signal.

Between these equations, the tri-exponential function was chosen to fit the $\Delta F/F_0$ of the bleach recordings, as this mathematical description was consistent with a recent study (Roder and Hille, 2014). The fitted bleach was then multiplied by a factor that takes into account the differences in light levels between the bleach and the signal recordings and was finally subtracted from the signal to get the bleach corrected $\Delta F/F_0$ (Figure 5.1D). In the following Figures, all $\Delta F/F$ signals shown are calculated using the above described procedure.

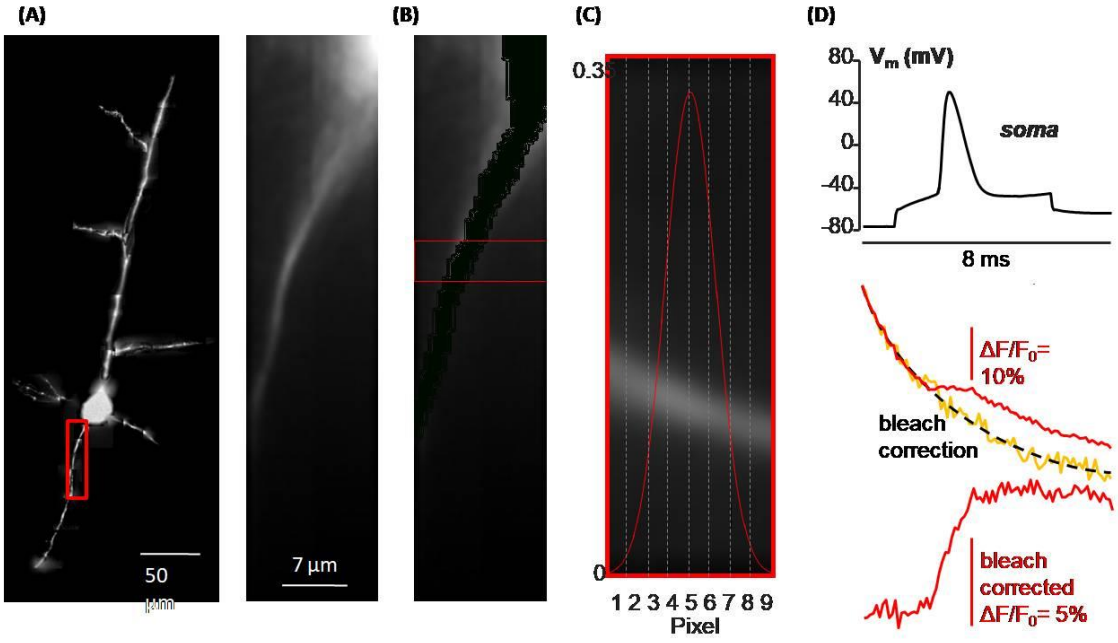

Figure 5.1: *Description of the bleach correction process.(A)(left) Reconstruction of a layer5 Pyramidal neuron filled with 0.5 mM ANG2. Red rectangle corresponds to the field of view during fluorescent experiments. (right) The same neuron as seen during fluorescence experiment with the 128 X 30 pixels configuration and the 20 µm laser spot (average of 4 trials). (B) The applied mask and a selected region of 9 X 30 pixels. (C) The selected region from (b) zoomed and rotated. The red line is the Gaussian weight applied to each pixel when averaging the region. (D)(top) somatic V_m recording of an evoked action potential. (middle) the red trace is the corresponding $\Delta F/F_0$ signal and the black dotted trace is the tri-exponential fit to the bleach. (bottom), the $\Delta F/F_0$ signal corrected for the bleach*

5.1.3 Calibration of Na^+ signals

When using Na^+ indicator dyes, the Na^+ concentration is not measured directly and a calibration is necessary to express fluorescence changes into changes of sodium concentration. In the case of the sodium indicator ANG2, a linear relation between the fluorescence change and the sodium change can be considered, such that $\Delta[Na] \approx \Delta F/F_0$ since the K_D of ANG2 is high (32 mM) and therefore fluorescence changes are expected to be

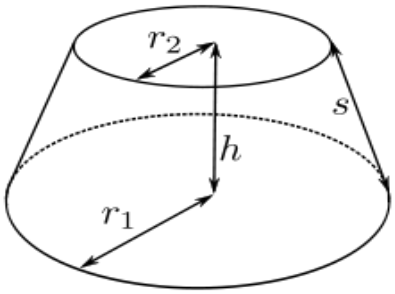

linear (Naumann et al., 2018). We calibrated the Na^+ dye using intracellular solutions with different sodium concentrations from 0 to 25 mM. The number of light counts was plotted against the mM concentration in Na^+ (Figure 5.2A). The linear part (2.5 mM to 15 mM) was fitted by the linear equation below:

$$F([Na^+]) = 3.9 \cdot 10^2 \cdot [Na^+] + 2.9 \cdot 10^3$$

Considering that the intracellular sodium concentration at rest is 10 mM, F_0=F([10mM]) and thus, from the above equation, it can be calculated that 1% $\Delta F/F_0$ = 0.1743 mM.

It is also useful to convert fluorescence changes into number of Na^+ ions instead of mM and for that, the diameter of the axon needs to be measured. This was done using the mask that was applied during the image analysis step. From this mask, the number of pixels at each of the 128 pixel- lines inside the mask was considered to be equal to the diameter. A power equation a*x^b+c was fitted to this measurements to get a smoother transition from one region to another (Figure 5.2B). Knowing the diameter of the axonal compartment at each position we could then calculate the volume of the axon at each pixel line, considering each axonal compartment to have the shape of a truncated cone with r_1 and r_2 the small and bigger site radius as calculated and h=0.5 µm the distance between two pixels . In the same way we can calculate the lateral surface area.

$$V = \frac{\pi}{3} \cdot (r_1^2 + r_2^2 + r_1 \cdot r_2) \cdot h$$

$$A = \pi \cdot (r_1 + r_2) \cdot \sqrt{(r_1 - r_2)^2 + h^2}$$

The number of Na^+ ions (N_{ions}) at each compartment is then calculated following:

$$N_{ions} = \frac{\Delta F}{F_0} \cdot Calibration \cdot N_{avogadro} \cdot V$$

Where $\Delta F/F_0$ is the fluorescence signal, Calibration=0.17 mM (or mol/dm^3) as calculated previously, $N_{avogadro}$= $6 \cdot 10^{23}$ mol^{-1} is the number of Avogadro and V the Volume. Subsequent conversions to the sodium current (I_{Na}) can be easily made:

$$I_{Na} = \Delta N_{ions} \cdot C/t$$

Where C is the fundamental charge ($1.6 \cdot 10^{-19}$ Coulombs), t is the time and ΔN_{ions} is the change in the number of ions. The following realistic example consistent with our measurement is given. An 8% change of fluorescence will be equivalent to 1.36 mM change of Na^+ corresponding to a charge concentration change of ~0.13 pC/µm^3. Thus, in a volume of 80 µm^3, a charge of 10.4 pC changing in 1 ms will contribute a sodium current of 10.4 nA.

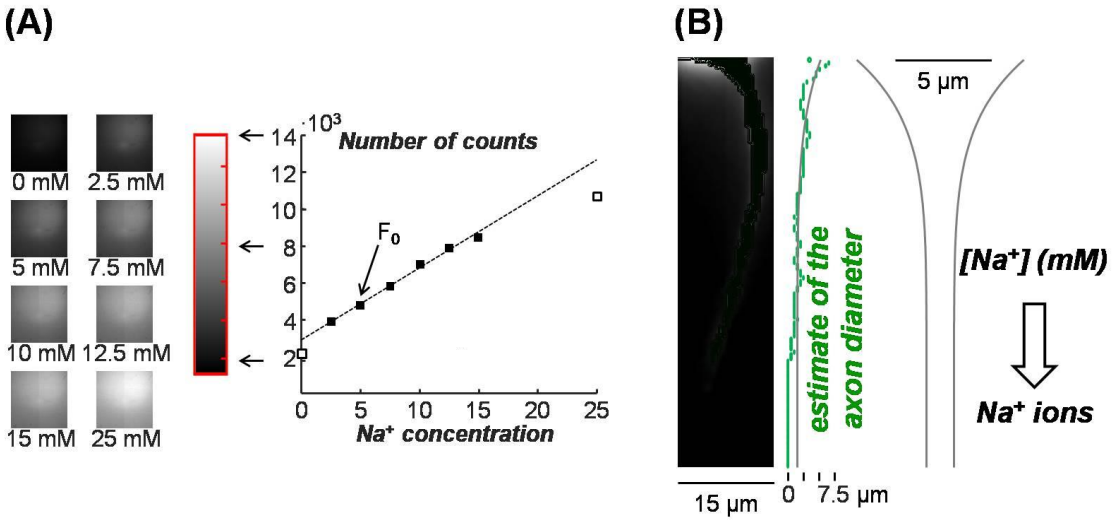

Figure 5.2: *Calibration of Na^+ signals (A)(left) Frames of cuvettes with basic internal solution with 0.5 mM ANG-2 and different Na^+ concentrations from 0 to 25 mM. Gray scale is indicated. (right) Plot of the light intensity against Na^+ concentration and linear fit. From the fit, 1% $\Delta F/F_0$ corresponds to 0.17 mM. (B)(left) In the depicted neuron, a mask is used to estimate the diameter of the axon initial segment. In this way, it is possible to convert the Na^+ concentration ($[Na^+]$) into a number of ions. (right) Schematic of the shape of the AIS.*

5.1.4 Block of Na^{2+} signals

To confirm the origin of the Na^+ fluorescence transient signals from VGNC we blocked TTX-sensitive Na^+ channels with Huwentoxin IV (HwTx-IV). Figure 5.2A shows a representative cell in which 2.5 µM HwTx-IV was locally applied next to the AIS. Both somatic action potentials and Na^+ transients along the axon where fully blocked. The inhibition of the somatic action potential and of the $\Delta F/F_0$ in different zones of the AIS was consistent in all 5 cells tested with this pharmacological block. The statistical values of the analysis of these experiments are reported in the caption of Figure 5.2B. These results

confirm that the Na^+ signals reported in this chapter exclusively originate from Na^+ influx via TTX-sensitive VGNCs.

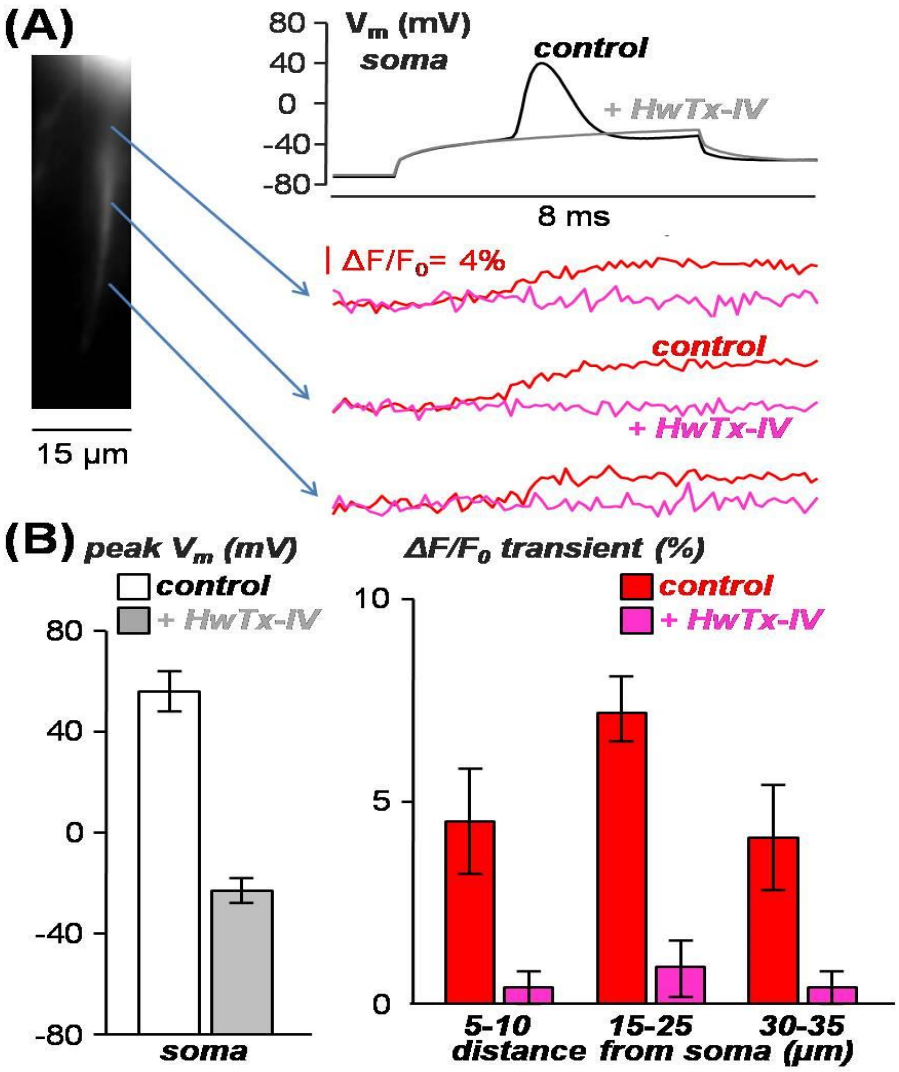

Figure 5.3: *Block of Na^+ signals by the TTX-sensitive Na^+ channels blocker Huwentoxin IV (HwTx-IV). (A) Action potential evoked in the depicted cell and corresponding $\Delta F/F_0$ signals in 3 positions in the control condition (average of 6 trials) and during the block (average of 2 trials). Signals recorded in control conditions inhibited by perfusion with solution containing 2.5 µM HwTx-IV. (B) Mean ± SD (N = 5 cells) of the peak V_m and of the $\Delta F/F_0$ transients in control conditions and after HwTx-IV application.*

5.2 Spatial distribution of Na^+

The question on the density of Na^+ channels in the AIS and whether it is higher in the AIS compared to the soma and dendrites has been extensively addressed in the last years. Even among the studies that show a higher concentration in the AIS, disagreement exists regarding the extent of the difference and the contribution of the higher Na^+ channel density in the AIS and whether this fact makes the AIS the preferable site for the action potential initiation. Measurements from immunostainings of Na^+ channels density in different neurons has shown a higher concentration of Na^+ channels in the AIS (~30 fold higher) than on the soma (Meeks and Mennerick, 2007; Wollner and Catterall, 1986; Kole et al., 2008). On the contrary, cell attached, outside out and bleb patch clamp recordings pinpointed a similar amount of Na^+ channel distribution in all compartments (Colbert et al., 1996; Colbert et al., 2002; Bradke et al., 2012; Aldrich et al., 1987). Both techniques have been shown to over or under estimate Na^+ channel distribution by labeling nonfunctional channel proteins or due to the tight coupling of these channels to the actin cytoskeleton, respectively.

In the next experiments we applied our novel Na^+ imaging approach to investigate the spatial distribution of Na^+ channel activation in the AIS. Again, we imaged changes in intracellular sodium during a single action potential evoked by somatic current injection. Figure 5.3A (top left) shows a neuron in the recording position. In this neuron, as in 5 other cells, the distal regions that appear less bright are not taken into account in the measurements as the laser spot is not big enough to illuminate the whole area of acquisition. Consistent with earlier work in the same type of neurons (Fleidervish et al., 2010) as well as cerebellar Purkinje neurons (Lasser-Ross and Ross, 1992), changes in Na^+ fluorescence during an action potential were largest in the axon, whereas they were very subtle or even undetectable in the soma (Figures 5.3A-B).

More specifically, in the six representative recordings in different axonal regions (indicated with blue arrows in Figure 5.3A), it can be seen that the signals beyond ~20 μm from the soma are the largest, whereas the fluorescence transient decreases beyond ~20 μm from the soma. Within the first 10-15 μm from the soma, peak amplitude of the fluorescence transient grows steadily, reaching a maximum at ~20 μm from the soma, and again decreasing from ~30 μm. This result is evident in the colour-coded image superimposed on the axon, corresponding to the maximal signal amplitude in all locations illuminated by the laser spot (Figure 5.3B). The results from 6 cells are shown in the scatter plot of Figure 5.3B

and the corresponding statistical analysis, performed on signals averaged on larger areas, is reported in Figure 5.3C.

In good agreement with previous studies (Kole et al., 2008; Baranauskas et al., 2012), our results are consistent with the hypothesis that Na^+ channel density is indeed higher in the axon, with the highest density occurring at 25-30 μm distance from the soma. Interestingly, these results suggest that the location of the highest sodium channel concentration does not co-localise with the region of action potential initiation attributed at 36-41 μm distance from the soma in mice, as shown by Baranauskas et al., 2012. On the other hand, Popovic et al., 2011 showed, through V_m imaging experiments in mice, that there is a spike trigger zone of ~16 μm long with its centre positioned ~30 μm from the edge of the soma, instead of just a single site.V_m imaging experiment must be performed to confirm the existence of a spike trigger zone in our experimental preparation. The theory suggesting that action potential initiation happens at the site where sodium channels distribution is highest would be in this case challenged. Additional studies have indicated that higher channel density is not required for initiating action potentials in the AIS (Lazarov et al., 2018). The channel density might not be crucial for initiating the action potential but it could be of importance in terms of the temporal accuracy of its generation, as indicated by several studies (Lazarov et al., 2018; Kopp-Scheinpflug and Tempel,2015).

Our results show the ability of our system to reproduce the reported characteristics of the spatial distribution of Na^+ channels in the axon with twice the spatial resolution and a temporal resolution five times faster than the so far presented Na^+ imaging experiments. Differences with previously reported findings are expected to be mostly in the temporal domain, where our resolution is improved 5 fold. A comparative study would be interesting, since it is evident that simply by re-sampling any of the recorded traces of Figure 5.3A down to 2 KHz we lose important information about the temporal, and also fundamental quantitative features of our signal, such as the onset time and the rising phase (Figure 5.4D). Therefore, it is clear that significant information will be obtained by conducting Na^+ measurements using our novel approach in the near future.

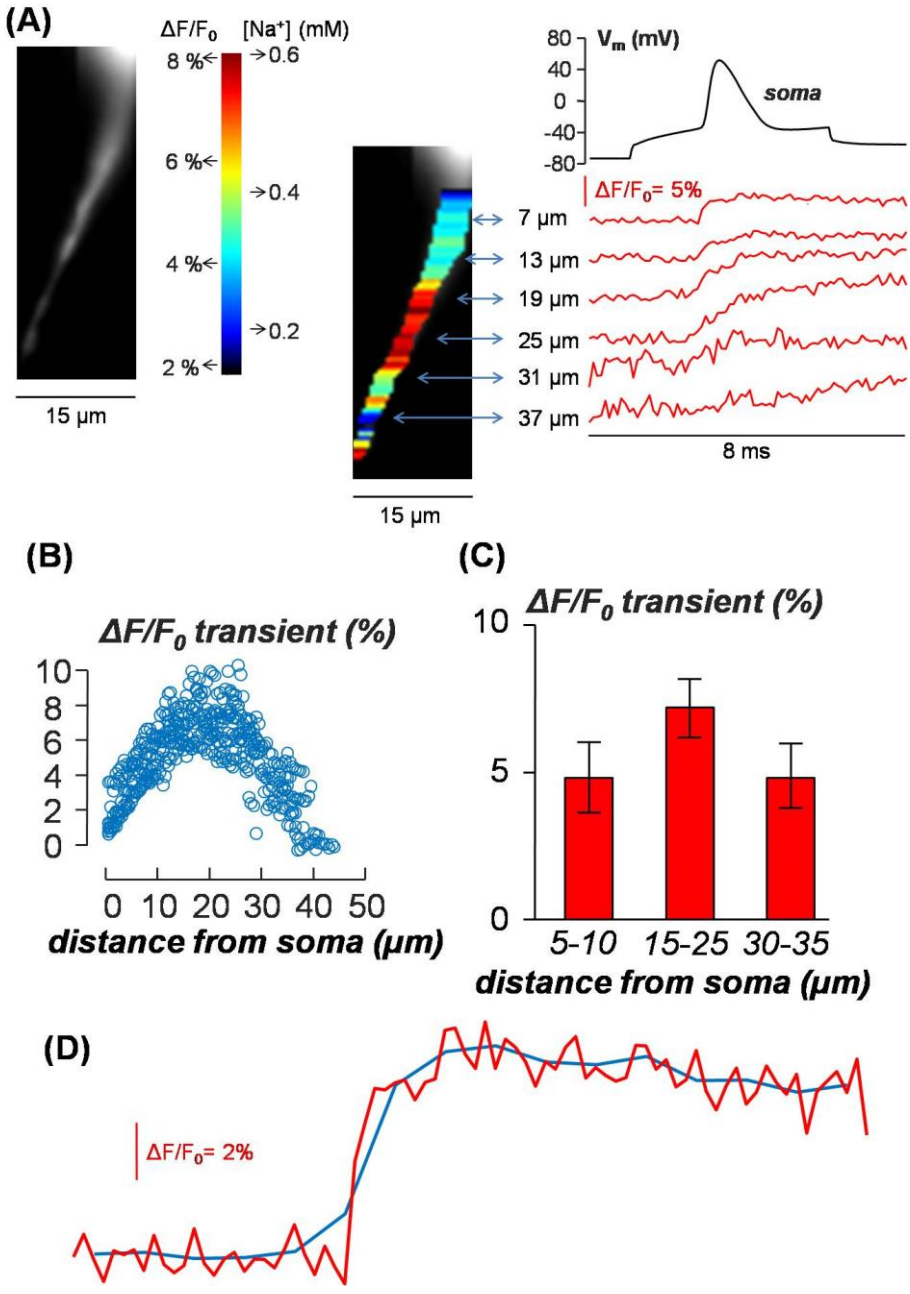

Figure 5.4: *(A) L5 pyramidal neuron filled with 0.5 mM ANG-2. Action potential evoked in the depicted cell and corresponding $\Delta F/F_0$ signals acquired at 10 kHz in 6 positions with estimated distance from the soma indicated (average of 4 trials). The spatial distribution of the maximum signal ($\Delta F/F_0$ transient) and the corresponding change in intracellular Na^+ concentration, estimated by calibration, is also reported in colour scale. (B) Scatter plot of $\Delta F/F_0$ transient against the distance from the soma from N = 6 cells. (C) Mean ± SD (N = 6 cells) of the $\Delta F/F_0$ transients in three zones (5-10 µm, 15-25 µm and 30-35 µm distance from the soma, respectively). The transient at 15-25 µm distances from the soma was significantly larger than in the other zones. (D) Red trace: recorded $\Delta F/F_0$ at 10 KHz. Blue trace: the same $\Delta F/F_0$ re-sampled at 2 KHz.*

5.3 Evaluation and correction for Na^+ lateral diffusion

In contrast to Ca^{2+}, there are no Na^+ buffering mechanisms in the cytosol and so Na^+ is free to diffuse. High-speed imaging is capable of monitoring free Na^+ diffusion. For short time periods, such as our recording intervals, Na^+ dynamics can be attributed entirely to influx and diffusion, while pumps seem to not contribute at these time scale (Fleidervish et al., 2010). Na^+ dynamics is shown to be dependent on the shape and size of the compartment as well as the available sinks in the neighboring compartments (Zylbertal et al., 2017). Here we estimated the lateral diffusion of sodium in the sodium current kinetics. A diffusion correction strategy is proposed based on the fluorescent recordings. First, $\Delta F/F_0$ was converted into number of sodium ions, following the procedure described in the previous section.

In theory, from the known Na^+ concentration, it should be straightforward to solve the below diffusion equation and find the sodium current

$$\frac{d[Na]_i}{dt} = I_i + D \cdot \frac{d[Na]_i}{dx^2}$$

Where D is the diffusion coefficient. In practice, the significant noise in optical recording does not allow derivatives to be applied on them, as the result would be simply noise with the desired result hidden somewhere below that noise. Simplifying the diffusion equation by removing the source, gives the following Partial Differential Equation (PDE):

$$\frac{\partial c}{\partial t} = D \cdot \frac{\partial c}{\partial x^2}$$

The solution to the diffusion equation without a source which describes the spreading by diffusion of an amount of substance M deposited at time t = 0 in the plane x = 0 (Crank, 1975. The mathematics of diffusion. Oxford, Clarendon press), is given by:

$$C = \frac{M}{\sqrt{4 \cdot \pi \cdot D \cdot t}} \cdot e^{-(x^2/4 \cdot D \cdot t)}$$

This equation was used as a base to build the diffusion correction mechanism used for my data, making a few adjustments based on the characteristics of my signals.

First of all, the expression M/ sqrt(4πDt) in this equation shows that the amount of Na^+ diffusing remains constant and equal to the amount originally deposited in the plane x = 0. This condition does not apply to my data and so this part was replaced with the measured Na^+ concentration, considering the Na^+ signal at each time interval as a new point source.

The model was assumed to have no 'memory' of the previous sources (i.e. no integration over time), as the signal at each given time point already contains this information. This means that diffusion at time t is only affected by the signal at time t-1.

A third assumption was that only the signal from the closest neighbour is sufficient to measure the contribution of diffusion. Considering the averaging procedure with the Gaussian weight during the image analysis described in a previous section, the closest neighbour was not considered the adjacent pixel but the 4 pixels away belonging to a region not included in the averaging of the pixel of interest. This distance was kept constant at x = 2μm. Although contribution from the closest neighbour is enough, since contribution from the other neighbours should give the same result up to a point, multiple neighbours can be considered and their effect can be averaged to increase accuracy.

The diffusion coefficient for sodium was kept as found in the literature, D= 0.6 $\mu m^2\ ms^{-1}$ (Kushmerick et al., 1969). Finally, the diffusion correction equation takes the form:

$$Difcor(x,t) = (N_{ions}(x+4,t-1) + N_{ions}(x-4,t-1) - 2\cdot N_{ions}(x,t)\ ) \cdot e^{-(1/D\cdot t)}$$

And if more neighbours are added,

$$Difcor(x,t) = \frac{1}{9}\cdot \sum_{i=1}^{n} [\ (N_{ions}(x+i\cdot 4,t-1) + N_{ions}(x-i\cdot 4,t-1) - 2\cdot N_{ions}(x,t)] \cdot e^{-\left(i^2/D\cdot t\right)}$$

Figure 5.5A-B (left) shows sodium signals expressed in N_{ions} before and after correction for diffusion, as well as the diffusion correction at different locations along the axon indicated with arrows. To assess whether diffusion affected the current kinetics at this timescale, the original signal and the diffusion correction were fitted with a single sigmoid function, which is sufficient to reproduce the current amplitude but not its kinetics.

The derivative of each sigmoid was calculated (Figure 5.5A right) to compare the amplitude of the signal and the diffusion correction. Figure 5.5B (left) shows the first two

signals with the highest diffusion correction and corresponding currents (right). From this analysis, it can be concluded that the diffusion contribution is very small and thus does not affect Na^+ current kinetics attributed to a single action potential. The diffusion profiles of 5 cells in four time windows at 1-20 ms, 21-40 ms, 41-60 ms and 61-80 ms were measured along the axonal length (Figure 5.5C). As expected, diffusion contribution increases with time; the longer the recording time is the more diffusion takes place. Also diffusion is more evident towards the soma which is a big sink.

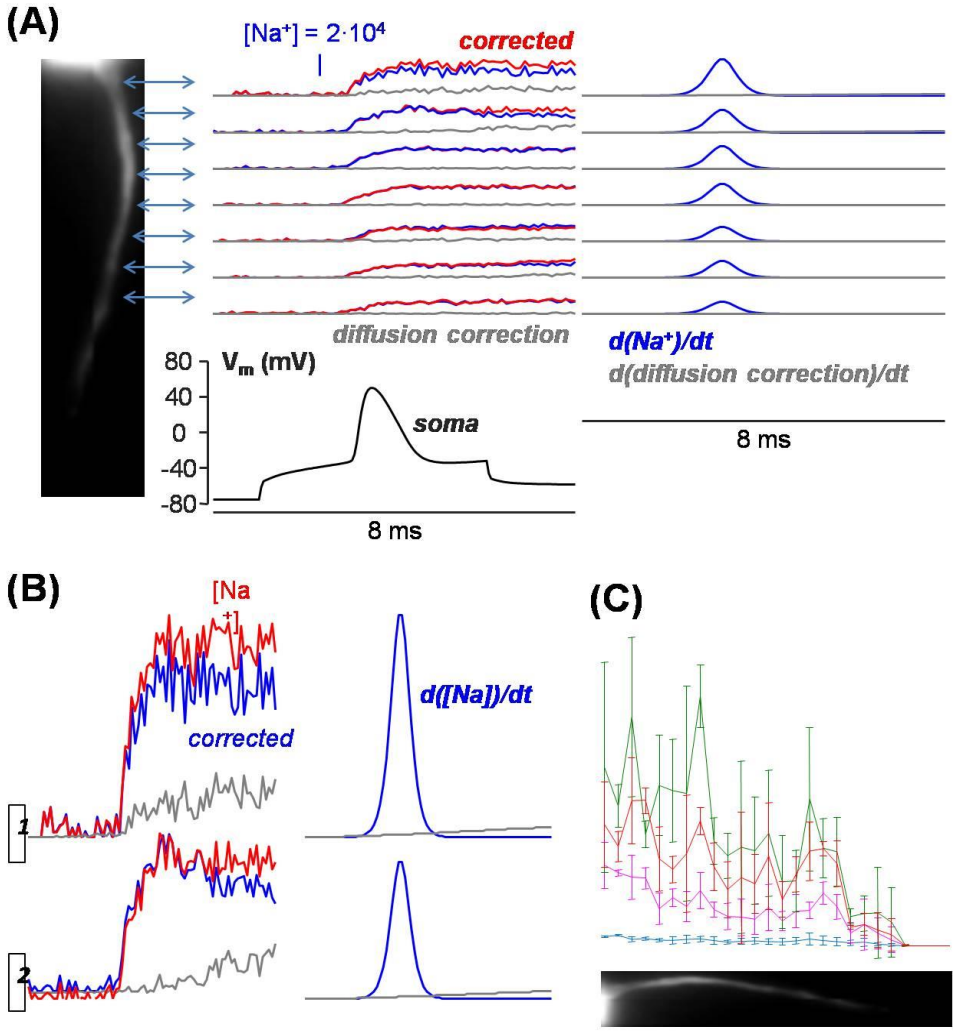

Figure 5.5: *Diffusion of Na+ (A) (right) A Layer5 Pyramidal neuron filled with 0.5 mM ANG2. (middle) Na^+ signals expressed in number of Na ions at different locations are shown in blue (average of 4 trials). Concentration corrected for diffusion shown in red. Gray traces are the absolute diffusion contribution. (bottom) Somatic membrane potential. (B) A single sigmoid was fitted to the signal and its derivative was calculated to measure the current amplitude (not kinetics). (right) The corrected signal and the diffusion correction are fitted with a sigmoid function to calculate the time derivatives.(C) The time derivative of the maximal diffusion corrections (regions 1 and 2) is negligible with respect to those of the corresponding corrected $\Delta F/F_0$ signals.(D) Diffusion profiles along the axon (128 pixels) of mean and std of 5 different cells and in four time ranges (1-20 ms blue, 21-40 ms magenta, 41-60 ms red, 61-80 ms green) versus distance from soma.*

5.4 Evaluation and correction for Na^+ lateral diffusion

Initiation of the action potential in the AIS has, among other theories, been attributed to the different kinetics of the Na^+ channel subtypes located there. It has been shown that the activation threshold in layer 5 pyramidal neurons is 7 - 14 mV lower in the distal AIS compared to the soma (Colbert and Pan, 2002; Hu et al., 2009). This shift is attributed to the low activation time of the Nav1.6 sodium channels that are highly concentrated at the distal part of the AIS, while the proximal AIS and soma have a higher concentration in Nav1.2 channels that have a higher threshold (Hu et al., 2009). Nav1.6 channels are considered to play a major role in the onset and upstroke of the AP (Oz et al., 2015), while Kv_1 channels are considered responsible for the width of the AP (Kole et al., 2007).

Moreover, persistent Na^+ currents have been suggested to play a role in regulating the AP threshold (Kole et al., 2008). It has been suggested that persistent Na^+ are produced solely by Na^+ channels located in the AIS (Astman et al., 2006; Stuart and Sakmann, 1995). More specifically, Nav1.6 has been suggested to be more effective in producing persistent Na^+ currents than Nav1.2 (Osorio et al., 2010; Smith et al., 1998; Burbidge et al., 2002).

Each and every one of these channels (and possibly other factors) may contribute to the shape of the Na^+ current kinetics. To investigate the kinetics of the Na^+ current associated with a single AP, we analysed the Na^+ transient in 6 Layer 5 neocortical pyramidal neurons. To obtain the kinetics of the Na^+ current from our recordings, Na^+ indicator fluorescence at a resolution of 100μs was characterised by the following sequential steps:

1. Calculate the fractional change of fluorescence (ΔF/F0).
2. Use the calibration to express fluorescence change in mM.
3. Calculate the diameter of the axon at various locations.
4. Convert mM concentration into number of Na+ ions.
5. Correct for diffusion.
6. Normalize to the asymptotic value.
7. Fit the signal with the product of three sigmoid functions.
8. Calculate the time derivative of the fit.

Steps 1-5 were described in a previous section. To fit the signals, the product of three sigmoid functions was used:

$$Y(t) = \prod_{i=1}^{3} \frac{1}{1 + e^{-a_i(t-b_i)}}$$

Where t is time and a_i and b_i are the parameters to be determined by the fit (Jaafari et al. 2015). The time derivative of the fitted signal, referred to in the text as Na^+ current or "$d(\Delta F/F_0)/dt$" signal, was expressed as percentage change over milliseconds (%/ms). The analysis was focused on a single axon region within the area of maximal fluorescence change as shown in the two examples of Figure 5.5A. The match between the Na^+ signal and the fit is an important factor in deriving the precise kinetics of the Na^+, as illustrated in Figure 5.5B.

In most $\Delta F/F_0$ signals, as in the two examples illustrated, there was a clear slope change observed before the peak of the signal. The first sigmoid sets the baseline before the onset of the signal while the other two sigmoids set the shapes of a first and second component that are necessary to reproduce the evident change in the slope mentioned above. The different kinetics of the two components is evident in the $d(\Delta F/F_0)/dt$ with a first sharp current with fast kinetics and a second one with slower kinetics.

To quantitatively analyse the time-course of the $d(\Delta F/F_0)/dt$ signal we characterised it with respect to parameters of the somatic AP. In all regions, the peak of the AP was delayed by 300-500 µs from the $d(\Delta F/F_0)/dt$ peak.. This result is not surprising because, after opening of Na^+ channels, the current is expected to be highest as the driving force for Na^+ is the strongest at this moment. Indeed, with 152 mM external concentration and 10 mM internal concentration, the reversal potential of at 34 °C is 74 mV. Thus, the driving force for Na^+ is ~5 times larger at the onset of the action potential (at -60/-55 mV) with respect to the time to peak (at +40/+50 mV). The profile of the peak interval in 6 neurons tested is reported in Figure 5.5B (left). We then analysed the second component of the $d(\Delta F/F_0)/dt$ measuring the Na^+ current available at the time when the AP reaches its half maximum. In the 6 analysed neurons, the slow current ranged from 10-28 % with respect to the fast peak and its statistics is reported in Figure 5.5B (right). Since this persistent current coincides with the action potential repolarisation, it is likely due to slowly inactivating VGNCs.

Altogether, the data presented in Figure 5.5 represent the first direct optical measurement of the physiological Na^+ current in the axon of layer 5 neocortical

pyramidal neurons. A possible origin of the two different components in the Na^+ current can be attributed to the different activated VGNCs. Indeed, as reported in Colbert and Pan, 2002; Hu et al., 2009; Ye et al., 2017; Rush et al.2005 and other studies, two subtypes of VGNC are found in the axon of the Layer 5 cortical neurons, Nav1.6 and Nav1.2, which have different kinetics. Whether these two channels co-localise and can give this kind of signal is unknown. However, early speculation is that the first current can be linked to Nav1.6 which is reported to have an activation threshold around -55mV with complete activation around -20 mV and half inactivation around -80 mV, while the second component can be linked to Nav1.2 which has a depolarizing shift of ~14mV. Another possible explanation is that the slower component can be the persistent sodium current that has been shown to be linked solely to sodium channels located in the AIS and specifically by Nav1.6 (Astman et al., 2006; Stuart and Sakmann, 1995; Osorio et al., 2010; Smith et al., 1998; Burbidge et al., 2002). The slower component is likely not linked with the resurgent sodium current reported for several neurons and is associated with both Nav1.6 and Nav1.2 (Rush et al., 2005; Afshari et al., 2004) since this current has much slower decay kinetics (Raman and Bean, 1997).

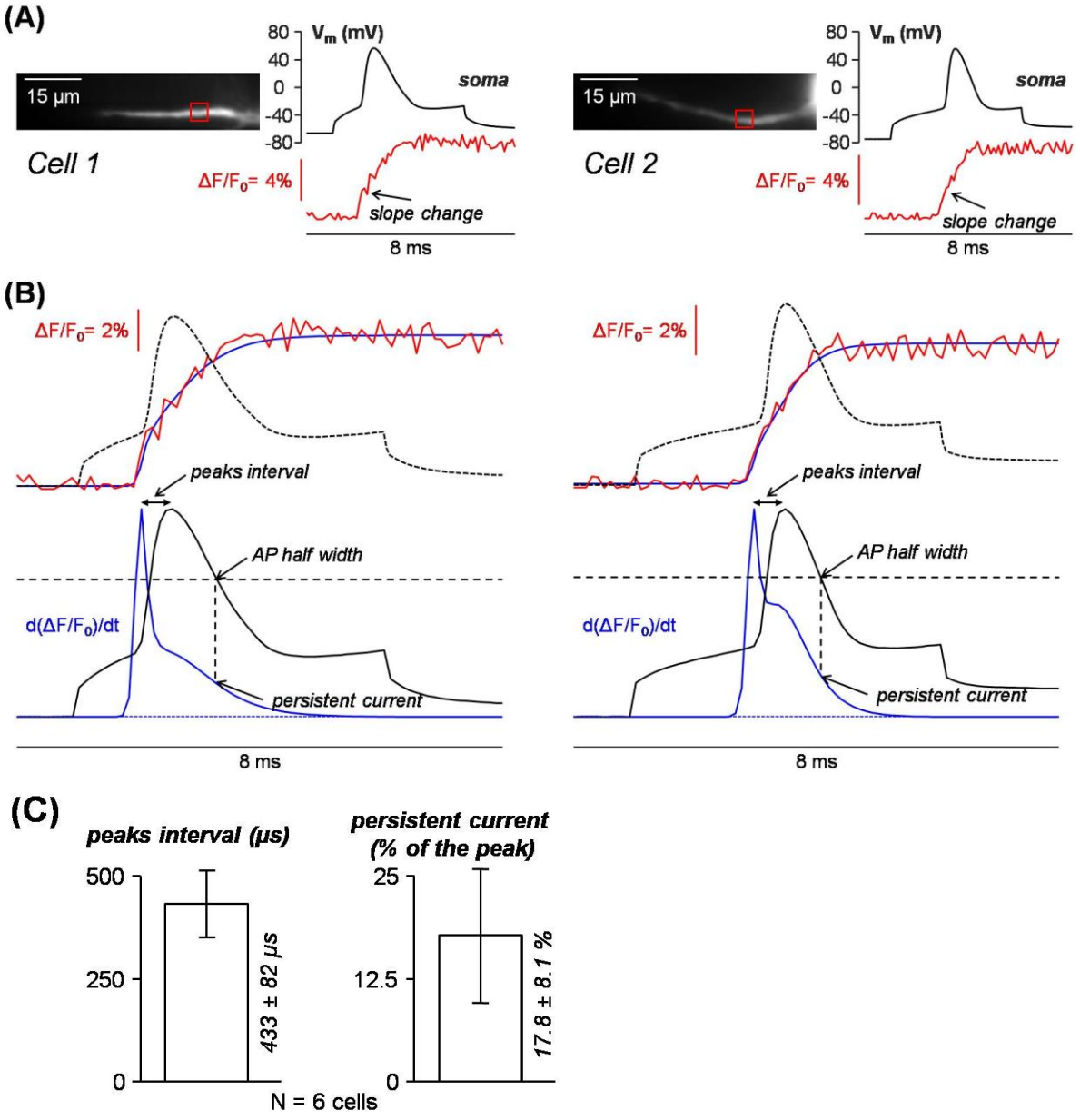

Figure 5.6: *Extraction of Sodium current kinetics (A) In two representative cells an evoked action potential evoked corresponding $\Delta F/F_0$ signals in the indicated position. The arrow points at a visible change in slope. (B) The $\Delta F/F_0$ signal is fitted with the product of two sigmoid functions (blue trace above) matching the change in slope. The action potential is also reported. The time derivative of the fitting function (blue trace below) is the estimate of the kinetics of the Na^+ current. The double-ended arrow indicates the interval between the peaks of the Na^+ current and the action potential. The single ended arrows indicate the time point of the action potential peak and the persistent Na^+ current during action potential repolarisation. (C) Mean ± SD (N = 6 cells) interval between the peaks of the Na^+ current, the action potential and the persistent Na^+ current.*

5.5 Perspectives on experiments that are currently going on in the laboratory.

A precise characterisation of the mechanisms underlying the Na^+ current kinetics and the association with action potential generation is of crucial importance in neuroscience. The Na^+ channel kinetics are expected to depend mostly on the properties of the VGNCs present at every location along the axon. Hu et al., 2009 suggested that in Layer 5 neocortical pyramidal neurons the distal part of the AIS is occupied exclusively by Nav1.6 channels while Nav1.2 channels are closer to the soma. This study also showed that there is a distinct role for Nav1.6 and Nav1.2 in action potential initiation and backpropagation, respectively.

To investigate the role of each VGNC in Na^+ current kinetics and the action potential initiation, we are currently using two toxins to selectively inhibit each channel subtype. Specifically, the 4,9-Anhydro-TTX is used to inhibit Nav1.6 channels, whereas Phrixitoxin-3 is used to inhibit Nav1.2.

Figure 5.7A shows a cell in which 1 µM 4,9-Anhydro-TTX was locally applied. Application of this blocker resulted in the reduction of the Na^+ signal along the axon except for the proximal region where the signal seems to be still elevated. In the proximal region, the shape of the Na^+ signal after 4,9-Anhydro-TTX application suggests that this signal originates from the persistent Na^+ current. The presence of a persistent Na^+ current is also suggested by the shape of the Na^+ signal in the control condition towards the end where a sudden increase in Na^+ concentration occurs. Interestingly, the application of this blocker, that is expected to selectively inhibit Nav1.6, did not lead to action potential failures. Instead, the action potential was delayed and the activation occurred at more depolarized values.

Figure 5.7B shows a cell in which 1 µM Phrixitoxin-3 was locally applied. Surprisingly, the putative block of Nav1.2 caused an even higher decrease in Na^+ signal along the whole axonal length (distal part in focus). Similar to the putative action on Nav1.6, the action potential detected at the soma was delayed. These results suggest that the two channels work in synergy in generating and shaping the action potential and they do not have distinct and specific roles in the initiation or in the backpropagation of action potentials as suggested by Hu W, et al., 2009. To obtain a conclusive interpretation of these results, however, additional experiments on the selectivity of the two blockers, with respect to the other channel species, must be performed.

Another interesting observation that must be mentioned for some of the cells analysed, is a subthreshold Na^+ transient preceding the initiation of the action potential and coinciding with

the subthreshold depolarisation associated with the somatic current injection (see for example the red trace in Figure 5.7B). It is not clear which channel is responsible for this specific current, although we observed that this signal is more affected by the putative block of Nav1.2 compared to the putative block of Nav1.6 (data not shown). A subthreshold current was observed in the majority of neurons I have analysed so far, and the observed location along the axon does not seem to be specific. Figure 5.7C shows a representative example neuron where a subthreshold signal is clearly distinguishable above the photon noise. Further analyses on the origin and role of this subthreshold signal need to be performed to locate its preferential position along the axon and to define its source.

Finally, the goal of my research that will continue for the next two years in the laboratory is to characterise, in great detail, the dynamics of all ion channels, including K^+ and Ca^{2+} channels (Shuet al., 2007; Kole et al., 2007; Yu et al., 2010), involved in the action potential generation and backpropagation. To this aim, I will use the combined imaging/computational approach that I developed during my thesis described in Chapter 4, but in addition I will perform V_m imaging as well as combined Na^+ and Ca^{2+} imaging using Na^+ ANG-2 measurements and Fura indicators (Miyazaki and Ross, 2015; Miyazaki et al., 2019). An example of this type of measurements is reported in Figure 5.7D. Altough is was attempted to perform combined V_m and Na^+ imaging, it was not possible to obtain clean signals because of the overlap in the emission spectra of the two dyes. This combination can in principle be achieved by using UV-excitable Na^+ indicators such as SBFI, but the sensitivity of these indicators is insufficient to obtain the high-quality measurements described in this chapter. Alternatively, a strategy similar to the one reported in the previous chapter, where we combined imaging and pharmacological studies with computational models to extract channel kinetics, can be utilised to extract the kinetics of the ion channels in the AIS during the action potential generation. A plethora of information can be acquired from these studies, increasing our understanding of the VGNC characteristics in the AIS, their role in initiating and shaping the action potential, and the pathological scenarios occurring in the case of mutations of Na^+ channels underlying some severe brain disorders such as autism.

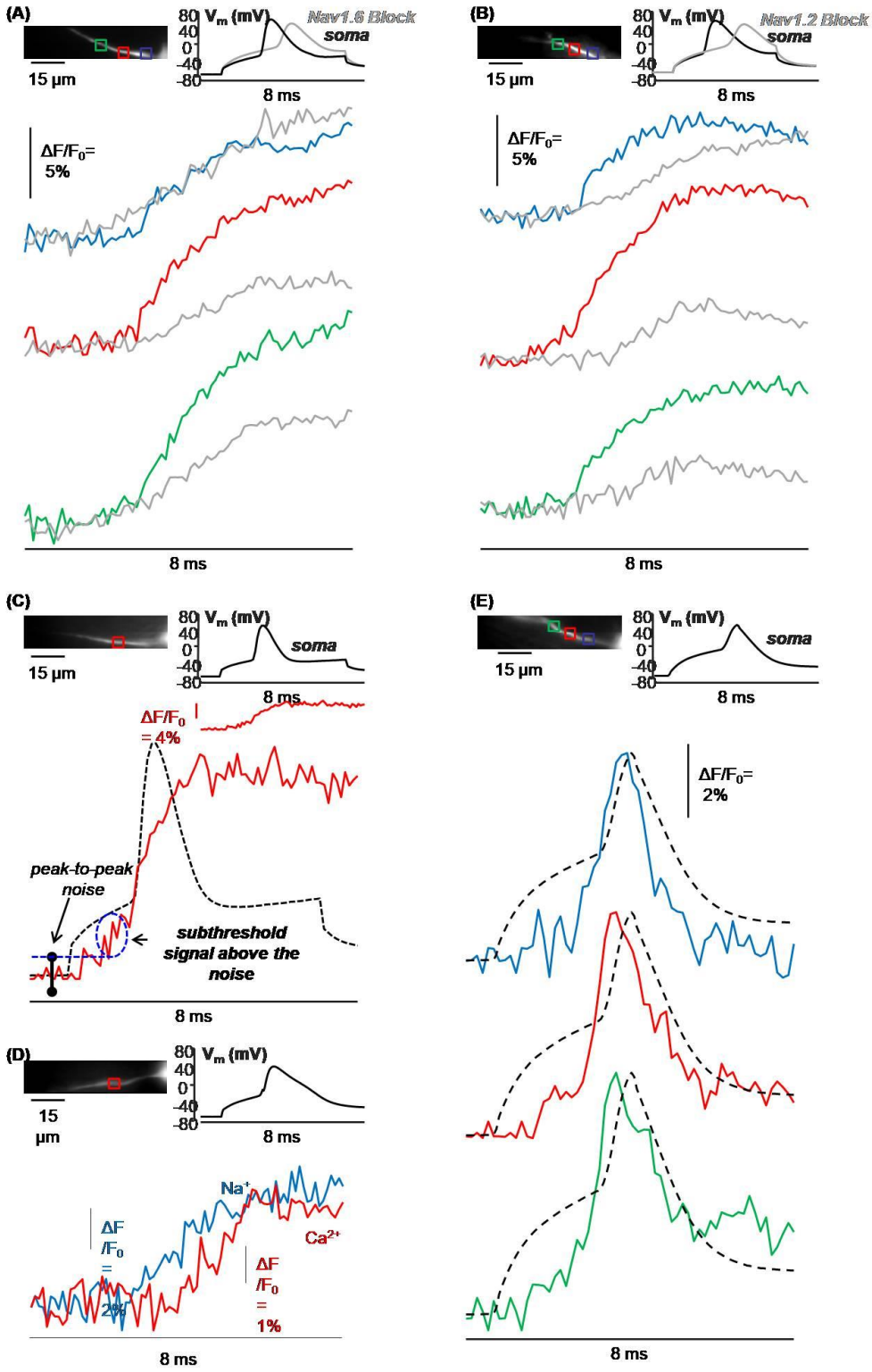

Figure 5.7: *Perspective experiments.* ***(****A) Block of Nav1.6 hhannels. Action potential evoked in the depicted cell and corresponding* $\Delta F/F_0$ *signal in three indicated positions, in control condition and after application of 4,9-Anhydro-TTX.* ***(****B) Block of Nav1.2 channels. Action potential evoked in the depicted cell and corresponding* $\Delta F/F_0$ *signal in three indicated positions in control condition and after application of Phrixotoxin. (C) Subthreshold currents. Action potential evoked in the depicted cell and corresponding* $\Delta F/F_0$ *signal in the indicated position. The same signal above is shown at a larger scale, superimposed to the action potential (black dotted line). The level of the photon noise (~3 times the SD) is indicated. The signal above the noise, corresponding to the subthreshold raising*

of the somatic V_m, is indicated. (D) Combined Na^+ and Ca^{2+} imaging. Action potential evoked in the depicted cell and corresponding $\Delta F/F_0$ Na^+ and Ca^{2+} signals in the indicated position. (E) Voltage imaging. Action potential evoked in the depicted cell filled with JPW and corresponding $\Delta F/F_0$ signal in three indicated positions. The action potential is superimposed to the signals (black dotted line).

5.6 Significance of measuring axonal Na^+ dynamics using our novel approach.

The spatial and temporal information on the activation and de-activation of Na^+ channels during action potential initiation and backpropagation, cannot be addressed with electrode techniques (Kole et al., 2008). This chapter reported a novel Na^+ imaging approach and a preliminary study of Na^+ signals and currents, in the AIS, during the generation of an action potential. The technique is based on Na^+ optical measurements of the fluorescence from the Na^+ dye ANG2 using an ultrafast camera. We were able to simultaneously monitor with unprecedented precision the kinetics of Na^+ currents and the somatic action potential (see Figure 5.6). We suggest that this current originates from the synergistic activation of two VGNCs.

In particular, we found that the Na^+ signal is different in the initial 10 µm of the AIS, in the area of maximal Na^+ channel distribution at ~20 µm distance from the soma, and beyond ~30 µm from the soma. While the highest concentration of Na^+ channels is found in the central part of the AIS, the site of action potential initiation has been shown to be the distal part (Palmer and Stuart, 2006), but whether this quantitative result applies to our specific biological preparation needs to be demonstrated. This mismatch in fact contradicts the hypothesis that the low threshold for action potential initiation in the distal AIS is due to the higher concentration of Na^+ channels. The action potential initiation in the distal AIS seems to be favoured by a large ratio source to load ratio (Moore et al., 1983; Mainen et al., 1995; Baranauskas et al., 2012). Na^+ channels are generally more concentrated in the AIS than in the dendrites and soma. This high density in the AIS provides a large source current which, along with its small axonal diameter, provides the optimal capacitive load and electrical isolation from the soma.

The diffusion of Na^+ was shown to contribute only slightly in shaping the Na^+ current and therefore Na^+ signal dynamics can essentially be described in terms of sodium influx, allowing the estimation of Na^+ current kinetics by calculating the time derivative of the Na^+ transient. In the proximal AIS, Na^+ signals show a change in their slope preceding or coinciding with the peak of the action potential recorded in the soma. This change in slope is

reflected in the Na^+ current shape that shows at least two components. While the timing of the maximal time derivative coincides with the onset of the action potential (when the driving force for Na^+ is maximal) a proposed key mechanism of the global kinetics of the current is the contribution of two VGNCs with different kinetics. Activation of the fast Nav1.6 channels participates in generating the fast rising part of the current, while the slow phase is attributed to Nav1.2 channels with slower kinetics. However; this explanation is only a first approximation since it neglects the fine kinetic properties of the two channels. In particular, the persistent current that regulates the duration of the slow inactivating current, is neglected here. Further experimental analyses are required to unravel in greater detail the kinetic behaviour of these two channels.

The observation of a subthreshold Na^+ signal above the photon noise can, in some cases, be a mechanism contributing to the initiation of the action potential. In future experiments, it will be pivotal to unravel the exact activity of different VGNCs during an action, a task that can now be performed using our innovative experimental approach. In these experiments, it will be necessary to unambiguously discriminate between the contributions of Nav1.2 and Nav1.6, a task that requires reliable selective blocking of each of the two channels independently.

Finally, to extract the kinetics of each ion channel contributing in shaping the action potential, computational approaches will be applied following the procedure described in the previous chapter, and this work will be continued by myself in the laboratory.

Chapter 6. Discussion and conclusions

Ion channels spanning the neuronal membrane allow the selective transport of ions between the extracellular and intracellular space. This mechanism is responsible for the complex electrical activity of neurons, from the generation of action potentials to to neurotransmitter release and plasticity (Hille, 2001). The malfunction (channelopathies) of these proteins due to genetical mutations (Catterall et al., 2008) or autoimmune disorders (Buckley and Vincent, 2005), has been linked to several diseases in humans.

Individual channels can be studied using the patch-clamp technique in wild-type or mutated animals (Sakmann and Neher, 1984). This approach though has several disadvantages. First isolated channels do not function the same way as when in their native system. The discrete biophysical properties of an ion channel in the neuron depend highly on the interactions with other channels as well as several intracellular mechanisms. Furthermore, patch clamp techniques do not allow for spatial characterization, while it is known that the different processes associated with ion channels do not depend solely on their biophysical properties but also on their distribution along the cell membrane in different neuronal regions.

While dysfunction even of a single channel subtype has been linked to several diseases (Schorge, 2018), it is clear that the synergistic activity with other channels is what governs the excitability of the cell under physiological or pathological conditions. It is therefore crucial to investigate the activity of ion channels in their native system in order to understand the origin of the physiological signal and how it is affected by channelopathies. This PhD work is a step towards this ambitious goal by introducing the development of cutting-edge technologies for fast ion and voltage imaging from single neurons in brain slices. The main objective is to go beyond the simple recording of the ion currents, by reconstructing the activity of the set of different ion channels underlying a particular physiological signal. To this purpose, the proposed strategy involves the use of selective inhibitors of individual channel subtypes with animal toxins. The use of toxins has been established in many studies of ion channels and has recently been proposed as a treatment method for channelopathies (Kozlov, 2018). The extraction of the individual currents from the rich experimental information, is done with the development of computational models using the NEURON simulating environment to match optical data (Hines and Carnevale, 1997).

6.1 Objectives and limitations of high spatial and temporal resolution functional imaging

A first major task in my PhD work was to improve the spatial resolution of the recordings performed in the laboratory by advancing the state-of-the-art of confocal imaging. The possibility to study Ca^{2+} currents in dendrites is grounded on the ability of recording Ca^{2+} fluorescence transients in the kHz range, from multiple neuronal sites simultaneously and with submicron resolution.

Wide field fluorescence imaging has been used to measure Ca^{2+} signals (Jaafari et al., 2014; Ait Ouares et al., 2016). Yet, the spatial resolution that we could be achieved thus far was of a few microns, i.e. not enough to analyse local signals at fundamental compartments such as synaptic terminals or spines. The major disadvantage of the wide field approach is the limited spatial resolution. The location of the fluorescence source is not possible because of the scattered light arising from all sites that do not correspond to the putative recording site of from out-of-focus regions. Theoretically, the system's resolution is defined by its ability to discriminate two point objects and it is limited by diffraction. But in practice, the light coming from each point source spreads out radially interfering with the other's making the single point appear as a finite size blurred object. In addition, a fraction of photons does not reach the detector. This effect is mathematically described by the point spread function (PSF). The size of the PSF depends on the Numerical Aperture (NA) which is mathematically expressed as $NA=n*\sin\theta$, with n the refractive index of the medium and θ the half maximum cone of light that sees the objective. The spatial resolution of the system is set by the diffraction limit as described by the equation $d=1.22*\lambda/2*NA$ where d is the diameter of the spot and λ the wavelength of the excitation light (Patterson, 2009). In live cell imaging the most common wavelengths are in the visible range and considering an objective with NA greater than 1 the maximum d would theoretically be in the submicron range. In reality though this resolution cannot be achieved in brain slices where the cell is usually not on the surface but several microns bellow and thus the surrounding tissue scatters the light reducing the resolution.

Several techniques, such as confocal and 2-photon imaging (2P), that reject the scattered light have been developed but the use of them is subject to the experimental needs in spatiotemporal resolution, field of view, light dosage etc. The principle of both mentioned techniques is the scanning of points one by one sequentially, thus reducing either the exposure time or temporal resolution. In particular, if high-speed multiple-points acquisitions

are required, the short exposure time results in low light levels and poor SNR. Strategies to combine camera imaging with either confocal or 2P imaging include the use of a spinning disk (for confocal imaging) or patterned (holographic) illumination.

During my thesis I was involved in the development and assess of a novel fast multisite confocal system which is now fully functional in our laboratory (Filipis et al., 2018). The system is based on a rapid custom-made spinning disk providing an optimal compromise between minimal light rejection and confocality below 1 μm, with adequate axial sectioning. For the improved spatial resolution, we developed a novel non-pinned photodiode CMOS camera that overcomes the inherent problems of previous commercial CMOS cameras. This 4M pixels camera has real 16,000 dynamic range obtained with a 14 bits A/D device and the analog processing and digitization is achieved in parallel by 16 processors permitting to reach high speeds up to 25k frames/s in sub-images of ~1k pixels. We showed that the system is capable of recording Ca^{2+} signals from multiple sites of a dendrite with temporal resolution of over 1 kHz and at the same time clearly discriminate signals coming from dfferent synaptic spines (below 1 μm) or the dendritic bulk.

Additional to the system's ability to reject scattered light, is the ability to significantly reduce photobleaching, compared to wide field imaging, thanks to the quantalized illumination of the different neuronal regions.

Despite the high acquisition rate of these recordings that allow detecting fast Ca^{2+} transients associated with action potentials or synaptic activity, the measurement of the kinetics of fast Ca^{2+} channels is not possible (Jaafari et al., 2016). The limitation of confocal imaging in acquisition speed is mainly set by the number of detected photons, which is reduced by light rejection.

The way to obtain submicron resolution without rejection of emitted light is to use two-photon imaging that also allows axial confinement of fluorescence excitation (Oertner, 2002). Two-photon imaging without scanning microscopy is achievable by patterning the light shape to match the imaged structures, i.e. by performing two-photon holographic illumination (Papagiakoumou et al., 2013). In voltage imaging, signals have been recorded at several kHz from small neuronal compartments using one-photon holographic illumination (Foust et al., 2015; Tanese et al., 2017). In contrast, 2P holographic illumination has been set for Ca^{2+} imaging in brain slices and in vivo, but without achieving recordings from submicron structures in the kHz range (Nikolenko et al., 2008; Pozzi et al., 2015; Yang et al., 2016; Bovetti et al., 2017). Yet, it appears possible to achieve this resolution in the near future.

However, the present confocal system has several advantages over 2P. Microscopes that are equipped for electrophysiology can easily introduce the spinning disk in their existing system. It does not require advanced knowledge of optics to use and it is economic compared to other techniques such as 2P, as it requires minimal maintenance. The multimode laser box includes multiple wavelengths of excitations that each can be used to excite different indicators and extend the method to measuring other ions, or V_m as well. Additionally, the multimode laser box is 5-10 times more economic than typical lasers of equivalent power, used in conventional confocal microscopy.

6.2 Why using a computational approach to unravel native ion channel dynamics

The second task of my PhD thesis was to introduce a novel approach of data analysis, grounded on NEURON modelling, to extract ion currents from imaging experiments. In native neurons, physiological activation and de-activation of each ion channel is regulated by activation of other ion channels resulting in a synergy that determines electrical and chemical signals. The specific working hypothesis is that voltage-gated Ca^{2+} channels (VGCCs) are always functionally coupled to K^+ channels in two possible ways: to Ca^{2+}-activated K^+ channels (CAKC) through Ca^{2+} influx; or to voltage-gated K^+ channels (VGKCs), in particular A-type, through reciprocal V_m changes.

In this project, we focus on three classes of channels: VGCCs, VGKCs and CAKCs, which are the principal determinants of electrical activity in the dendrites of Purkinje Neurons and represent a substantial fraction of channelopathies underlying disorders in the Cerebellum. The PN receives a unique CF synapse responsible of large excitatory postsynaptic potential (EPSP) that depolarises the dendrite (Canepari and Vogt, 2008). The CF-EPSP spreads passively throughout the dendrites where it activates T-type (Isope et al., 2012) and P/Q-type (Usowicz et al., 1992) VGCCs. Then, the transient elevation of intracellular Ca^{2+} activates both SK K^+ channels (Hosy et al., 2011) and BK K^+ channels (Rancz and Hausser, 2006), and the ensemble of activated Ca^{2+} and K^+ channels, including VGKCs, shapes the waveform of the dendritic V_m.

A single-compartment NEURON model was proposed to predict the channel kinetics associated with the CF-EPSP (Anwar et al., 2012). Several models for each channel,

including kinetics of activation and inactivation, are available at the website https://senselab.med.yale.edu/ModelDB/. These models though are typically extracted by experimental channel analysis not performed *in situ*. We used this model, available in the ModelDB database, as starting point for our analysis and progressively changed the parameters to finally match our experimental data, leading to realistic reconstruction of the physiological kinetics of each individual channel involved. The model comprises 6 channels: P/Q-type and T-type VGCCs, A-type VGKCs, BK and SK Ca^{2+}-activated K^+ channels and a generic HVA-VGKC. The experiment and the simulations were performed at three initial V_m states: a hyperpolarised state (~-80 mV), and intermediate state (~-65 mV) and a depolarised state (~-50 mV). To compare experimental recordings (i.e. fluorescence changes) and computer simulations, optical signals are calibrated also considering endogenous Ca^{2+} buffering as previously described (Ait Ouares et al., 2016). By adjusting conductance models, computer simulations matched precisely V_m and Ca^{2+} signals. These adjustments were done by considering 12 cells in which these recordings were performed, and 47 additional cells where each channel was selectively blocked either by a toxin or by another organic molecule. According to the information extracted by using these toxins, satisfactory information on the kinetics of relevant ionic currents were revealed as well as functional interactions among channels that underlie important neuronal signals.

Both in experiments and simulation, when the dendrite is hyperpolarised the block of A channels, but not that of P/Q and BK channels has an effect on the Ca^{2+} signal. Vice-versa, when the dendrite is depolarised, the blocks of P/Q and BK channels, but not that of A channels, have an effect on the Ca^{2+} signal. The currents from the three channels obtained by NEURON simulations clearly indicate that A-type VGKCs prevent activation of P/Q-type VGCCs at hyperpolarised states, as suggested in a study (Otsu et al., 2014), and that BK K^+ channels are activated by P/Q channels, but both P/Q and BK channels activate at depolarised states when A channels are inactivated. This remarkable result shows that it is possible to reconstruct the realistic synergistic kinetics of all major channels involved in a signal and, for the first time, to unambiguously demonstrate the functional interactions of these ion channels that determine the V_m and Ca^{2+} signals. Thus, in this original approach, we could deliver to ModelDB a relatively simple model with only one compartment, but we enriched the database with realistic channel kinetics models under physiological and pathological conditions.

Here, a major research hypothesis is that the match of experimental data with NEURON simulations will not only reveal a realistic model for native functional channel synchrony, but

also the alterations induced by mutated proteins associated with channelopathies. The final product of this analysis, however, is essentially the extraction of all relevant ionic currents to establish links among channels and how the mutated function of one channel affects the function of the others. It is therefore clear how this general strategy will be a powerful and unique tool to unravel ion channel behaviours under physiological and pathological conditions.

6.3 Towards the full understanding of the action potential

Finally the last task of my PhD work was dedicated to the extension of the technique into Na^+ imaging, a necessary step to address the fundamental problem of the action potential generation, using combined imaging and computational techniques. Voltage gated Na^+ ions are the key component in the generation and propagation of the action potential in neurons. Hodgkin and Huxley first demonstrated the role of the VGNDs in the action potential (Hodgkin and Huxley, 1952). Their study though is only the crudest approximation of the physics of the action potential, in particular because their characterization was done in terms of Na^+ conductance.

In reality, different types of VGNCs are often co-expressed in most of the systems and they contribute in shaping the action potential. Specifically, in Layer 5 neocortical pyramidal neurons, Nav1.2 and Nav1.6 have been shown to cooperate in the generation of the action potential in the AIS of these neurons (Hu et al., 2009). Channelopathies involving either of these two channels cause several neurological diseases, including epilepsy and autism (Lena and Mantegazza, 2019; Spratt et al., 2019; Cannon, 2006; Dib-Hajj and Waxman, 2010; Jurkat-Rott et al., 2010; Mantegazza et al., 2010; Claes et al., 2009). It appears therefore evident that the ability of optically measuring Na^+ influx can be crucial to investigate the consequences of these pathologies. However, unlike Ca^{2+}, very few studies using Na^+ fluorescence imaging can be found in the literature, mirroring the lack of an efficient method to perform in the spatiotemporal resolution required for such measurements. In the last part of my thesis I tried to tackle this problem, using the advanced optical system developed in the beginning of my thesis, to measure Na^+ transients with the sensitive indicator ANG-2 (Miyazaki and Ross, 2015).

Using the cutting -edge technology develped in our laboratory we could study with unprecedented precision the spatial and temporal profiles of signals in the AIS. The spatial profile of the Na^+ flux recorded, is in line with previous studies (Kole et al.2008; Baranauskas et al., 2012), where it is shown that maximal Na^+ channel distribution is found at ~20 μm distance from the soma (middle of AIS). Uncertainty though exists as to where the AP initiates. Several studies show that the initiation occurs at the distal part of the AIS, while other studies suggest a bigger initiation zone that includes the middle of the AIS where maximal distribution has been shown (Baranauskas et al., 2012; Popovic et al., 2011). The size of the AIS can vary between species and neuronal types, depending also on the age of the animal, and thus, further experiments need to be performed to answer this question for our specific case.

Most importantly, we developed a procedure to extract the precise Na^+ current kinetics, involved in generating the action potential along the AIS. Since there are no intracellular buffers for Na^+ in the AIS, the recorded fluorescent signal is a function of only the flux of ion channels and diffusion (Fleidervish et al., 2010). We also demonstrated that diffusion during the time window of our recordings plays a minimal role in the form of the signal and in most cases the signals can be considered to reflect only Na^+ flux . This allows for the Na^+ current to be measured as the time derivative of the fluorescent signal.

The calculated Na^+ current shows two distinct components, a fast activating-inactivating component and a slow activating-inactivating component. As expected the first component seems to be maximal during the strongest Na^+ driving force. Additionally, interesting observations can be made about the second component, which appears to peak under a low driving force for Na^+. This indicates that, although the amplitude of the second component appears smaller than that of the first, the same does not apply for the concentration of activated channels. Interestingly, in order for the second component to occur under this low electrical gradient, a very big number of Na^+ channels must be active.

To fully understand the origin and shape of the action potential, a strategy similar to that reported in the previous section must be employed, where the imaging data will be reproduced by computational models to extract the channel kinetics of all ion channels involved in the action potential generation. In addition, preliminary data optained during this part of my thesis, involving the pharmacological test of the two VGNCs, Nav1.2 and Nav1.6, as well as the existence of a subthreshold Na^+ signal will be further tested to determine their contribution in the current kinetics.

6.4 Conclusions and future perspectives

The basic scheme reported below summarises the content of my thesis and the questions that will be addressed in the near future using this work. Two types of major advances were achieved during, one involving the optical techniques and the other the computational. In the field of optical techniques, we achieved the enhancement of the spatial and temporal resolution in functional imaging using a novel confocal system to reject out of focus light that can opperate in the ms and μm range. Furthermore, we could resolve Na^+ transients at highspatiotemporal resolution. These improvements constitute a technique that can be used to facilitate the understanding of the physiological behavior of native ion channels. What's more, using simple computational models we could establish a technique to interpret the big load of information provided by the imaging datasets to extract channel kinetics. The future perspective is to integrate the Na^+ imaging data into a computational model that will predict the observed physiological signal and allow the extraction of the mechanisms involved as well as their kinetics. Having characterized the physiological parameters, the technique can be farther utilized to study dysfunctions in ion channels that underlie specific diseases.

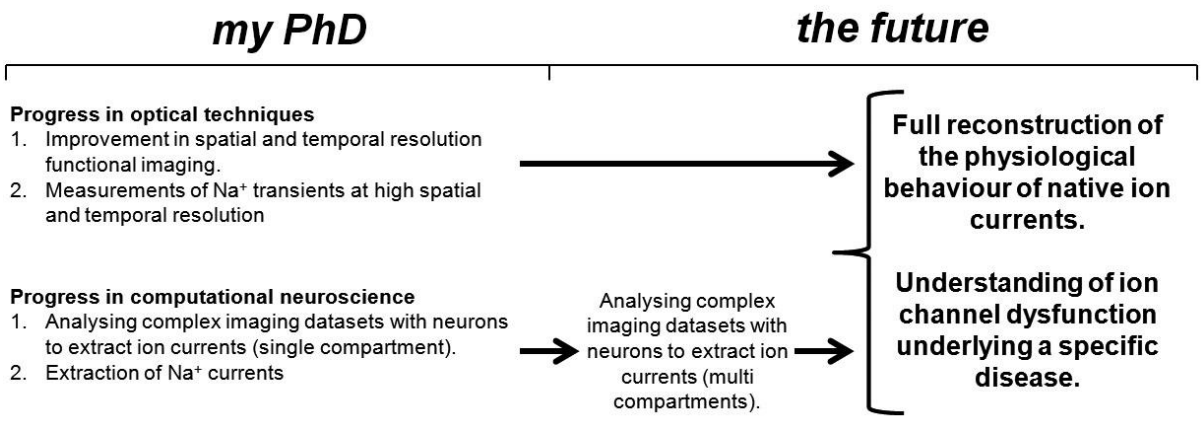

Chapter 7. Bibliography

1. Afshari FS, Ptak K, Khaliq ZM, Grieco TM, Slater NT, McCrimmon DR, Raman IM (2004). Resurgent Na currents in four classes of neurons of the cerebellum. J Neurophysiol 92: 2831–2843.
2. Ait Ouares K, Filipis L, Tzilivaki A, Poirazi P, and Canepari M (2019). Two Distinct Sets of Ca^{2+} and K^{+} Channels Are Activated at Different Membrane Potentials by the Climbing Fiber Synaptic Potential in Purkinje Neuron Dendrites. J. Neurosci. 39: 1969-1981.
3. Ait Ouares K, Jaafari N, Canepari M (2016). A generalised method to estimate the kinetics of fast Ca^{2+} currents from Ca^{2+} imaging experiments. J Neurosci Methods 268: 66 -77.
4. Aldrich RW, Stevens CF (1987). Voltage-dependent gating of single sodium channels from mammalian neuroblastoma cells. J Neurosci 7(2):418–431.
5. Amunt K, Ebell C, Muller J, Telefont M, Knoll A, Lippert T (2016). The Human Brain Project: Creating a European Research Infrastructure to Decode the Human Brain. Neuron 92 (3):574-581.
6. Anwar H, Hong S, De Schutter E (2010). Controlling Ca^{2+}-activated K^{+} channels with models of Ca^{2+} buffering in Purkinje cells. Cerebellum 11: 1–13.
7. Araki T, Otani T (1955). Response of single motoneurons to direct stimulation in toad's spinal cord. JNeurophysiol 18:472–85.
8. Astman N, Gutnick MJ, Fleidervish IA (2006). Persistent sodium current in layer 5 neocortical neurons is primarily generated in the proximal axon. J Neurosci 26(13): 3465–3473.
9. Baranauskas G, David Y, Fleidervish IA (2012). Spatial mismatch between the Na+ flux and spike initiation in axon initial segment. PNAS 110 (10) :4051-4056.
10. Barnett SF, Snape M, Hunter CN, Juárez MA, Cadby AJ (2017). A Novel Application of Non-Destructive Readout Technology to Localisation Microscopy. Sci Rep. 7: 42313.

11. Bègue A, Papagiakoumou E, Leshem B, et al. (2013). Two-photon excitation in scattering media by spatiotemporally shaped beams and their application in optogenetic stimulation. Biomed Opt Express. 4(12):2869–2879.
12. Berglund A, (2004). Nonexponential statistics of fluorescence photobleaching. J. Chem. Phys. 121: 2899–2903.
13. Bernstein J (1902). Untersuchungen zur Thermodynamik der bioelektrischen Ströme. Pflügers Arch 92:521–562 .
14. Boiko T, Van Wart A, Caldwell JH, Levinson SR, Trimmer JS, Matthews G (2003). Functional specialization of the axon initial segment by isoform-specific sodium channel targeting. Journal of Neuroscience. 23(6): 2306–2313.
15. Borlinghaus RT (2006). High speed scanning has the potential to increase fluorescence yield and to reduce photobleaching. Microscopy Research and Technique .69 (9): 689-692.
16. Bosmans F, Rash L, Zhu S, Diochot S, Lazdunski M, Escoubas P, Tytgat J (2006). Four novel tarantula toxins as selective modulators of voltage-gated sodium channel subtypes. Mol. Pharmacol. 69: 419–429.
17. Bovetti S, Moretti C, Zucca S, Dal Maschio M, Bonifazi P, Fellin T (2017). Simultaneous high-speed imaging and optogenetic inhibition in the intact mouse brain. Sci Rep 7: 40041.
18. Boycott BB (1998). John Zachary Young. 18 March 1907-4 July 1997. Biographical memoirs of fellows of the royal society.
19. Bradke F, Fawcett JW, Spira ME (2012). Assembly of a new growth cone after axotomy: The precursor to axon regeneration. Nat Rev Neurosci 13(3): 183–193.
20. Brager DH, Johnston D (2014). Channelopathies and dendritic dysfunction in fragile X syndrome. Brain Research Bulletin. 103: 11-17.
21. Brenowitz SD, Regehr WG (2005). Associative short-term synaptic plasticity mediated by endocannabinoids. Neuron. 45: 419-431.
22. Brette R (2013). Sharpness of spike initiation in neurons explained by compartmentalization. PLoS Comput Biol 9(12): e1003338.
23. Buckley C, Vincent A (2005). Autoimmune channelopathies. Nat. Clin. Pract. Neurol. 1(1): 22–33.
24. Burbidge SA, Dale TJ, Powell AJ, Whitaker WR, Xie XM, Romanos MA, Clare JJ (2002). Molecular cloning, distribution and functional analysis of the $NA_v1.6$. Voltage-gated sodium channel from human brain. Mol Brain Res. 103: 80–90.

25. Canepari M, Djurisic M, Zecevic D (2007). Dendritic signals from rat hippocampal CA1 pyramidal neurons during coincident pre- and post-synaptic activity: a combined voltage- and calcium-imaging study. J Physiol. 580: 463–484.
26. Canepari M, Mammano F (1999). Imaging neuronal calcium fluorescence at high spatio-temporal resolution. J Neurosci Methods 87: 1-11.
27. Canepari M, Nelson L, Papageorgiou G, Corrie J, Ogden D (2001). Photochemical and pharmacological evaluation of 7-nitroindolinyl-and 4-methoxy-7-nitroindolinyl-amino acids as novel, fast caged neurotransmitters. J. Neurosci. Methods 112: 29–4210.
28. Canepari M, Ogden D (2006). Kinetic, pharmacological and activity-dependent separation of two Ca2+ signalling pathways mediated by type 1 metabotropic glutamate receptors in rat Purkinje neurones. J Physiol. 573: 65–82.
29. Canepari M, Vogt K, Zecevic D (2008). Combining voltage and calcium imaging from neuronal dendrites. Cell Mol Neurobiol. 58: 1079–1093.
30. Canepari M, Vogt KE (2008). Dendritic spike saturation of endogenous calcium buffer and induction of postsynaptic cerebellar LTP. PLoS ONE. 3: e4011.
31. Canepari M, Willadt S, Zecevic D, Vogt KE (2010). Imaging inhibitory synaptic potentials using voltage sensitive dyes. Biophys J. 98: 2032–2040.
32. Cannon SC (2006) Channelopathies of the Nervous System. In: Runge M.S., Patterson C. (eds) Principles of Molecular Medicine. Humana Press 1088-1096.
33. Catterall WA, Dib-Hajj S, Meisler MH, Pietrobon D (2008). Inherited neuronal ion channelopathies: new windows on complex neurological diseases. J. Neurosci., 28: 11768-11777.
34. Ceriani F, Ciubotaru CD, Bortolozzi M, Mammano F (2016). Design and Construction of a Cost-Effective Spinning Disk System for Live Imaging of Inner Ear Tissue. In: Sokolowski B. (eds) Auditory and Vestibular Research. Methods in Molecular Biology, vol 1427. Humana Press, New York, NY
35. Claes LRF, Deprez L, Suls A, Baets J, Smets K, Van Dyck T, Deconinck T, Jordanova A, De Jonghe P (2009). The SCN1A variant database: a novel research and diagnostic tool. Hum Mutat 30: E904–E920.
36. Clay J, DeFelice L (1983). Relationship between membrane excitability and single channel open-close kinetics. Biophys J. 42:151–157.

37. Coates CG, Denvir DJ, Conroy E, McHale N, Thornbury K, Hollywood M. Back-illumintated electron multiplying technology; The world's most sensitive CCD for ultra low-light microscopy. http://www.emccd.com/papers.htm
38. Coates CG, Denvir DJ, McHale NG, Thornbury KD, Hollywood M (2004). Optimizing low-light microscopy with back-illuminated electron multiplying charge-coupled device: enhanced sensitivity, speed, and resolution. J. Biomed. Opt. 9(6): 1244-1252.
39. Cohen LB, Salzberg BM, Grinvald A (1978). Optical methods for monitoring neuron activity. Annual Review of Neuroscience. 1: 171-182.
40. Colbert CM, Johnston D (1996). Axonal action-potential initiation and Na+ channel densities in the soma and axon initial segment of subicular pyramidal neurons. J. Neurosci. 16: 6676-6686.
41. Colbert CM, Pan E (2002). Ion channel properties underlying axonal action potential initiation in pyramidal neurons. Nat. Neurosci. 5: 533-538.
42. Connor JA (1986). Digital imaging of free calcium changes and of spatial gradients in growing processes in single, mammalian central nervous system cells. Proc Natl Acad Sci USA 83: 6179– 6183.
43. Coombs JS, Curtis DR, Eccles JC (1957a). The interpretation of spike potentials of motoneurones. J Physiol. 139: 198–231.
44. Corle TR, Chou CH, Kino GS (1986). Depth response of confocal optical microscopes. Opt. Lett. 11: 770-772.
45. Crank (1975). The mathematics of diffusion. Oxford, Clarendon press
46. Cueni L, Canepari M, Adelman JP, Luthi A (2009). Ca^{2+} signaling by T-type Ca^{2+} channels in neurons. Arch Eur J Physiol 457: 1161–1172.
47. Cueni L, Canepari M, Luján R (2008). T-type Ca^{2+} channels, SK2 channels and SERCAs gate sleep-related oscillations in thalamic dendrites. Nat Neurosci 11: 683–692.
48. Dal Maschio M, Difato F, Beltramo R, Blau A, Benfenati F, Fellin T (2010). SSimultaneous two-photon imaging and photo-stimulation with structured light illumination. Opt Express 18(18):18720-31.
49. Davies R, Graham J, Canepari M (2013). Light Sources and Cameras for Standard in Vitro Membrane Potential and High-Speed Ion Imaging. J Microsc 251: 5-13.

50. De Schutter E (1998). Dendritic Voltage and Calcium-Gated Channels Amplify the Variability of Postsynaptic Responses in a Purkinje Cell Model. J. Neurophysiol 80(2): 504-519.
51. De Schutter E, Bower JM (1994). An active membrane model of the cerebellar Purkinje cell: II Simulation of synaptic responses. J. Neurophysiol 71: 401-419.
52. Deiters OFK (1865). Untersuchungen über Gehirn und Rückenmark des Menschen und der Säugethiere. Vieweg; Braunschweig, Germany pp. 1–318.
53. Dib-Hajj SD, Waxman SG (2010). Isoform-specific and pan-channel partners regulate trafficking and plasma membrane stability; and alter sodium channel gating properties. Neuroscience Letters 486(2): 84-91.
54. Dodge FA, Cooley JW (1973) .Action Potential of the Motorneuron. IBM J Res Dev 17: 219-29.
55. Donnert G, Eggeling C, Hell SW (2007). Major signal increase in fluorescence microscopy through dark-state relaxation. Nat Methods 4:81–86.
56. Du Bois-Reymond E (1841-1895). Laboratory diaries, Staatsbibliothek zu Berlin, Preußischer Kulturbesitz, Handschriftenabteilung: Sammlung Darmstaedter.
57. Edgerton JR, Reinhart PH (2003). Distinct contributions of small and large conductance Ca^{2+}-activated K^{+} channels to rat Purkinje neuron function. J Physiol. 548(Pt 1): 53–69.
58. Edwards C, Ottoson D (1958). The site of impulse initiation in a nerve cell of a crustacean stretch receptor. J Physiol. 143(1): 138–148.
59. Fertig HA (2002), Deconfinement in the two-dimensional XY model, Phys. Rev. Lett. 89: 035703
60. Filipis L, Ait Ouares K, Moreau P, et al. (2018). A novel multisite confocal system for rapid Ca^{2+} imaging from submicron structures in brain slices. J. Biophotonics 11: e201700197.
61. Finch E, Augustine G (1998). Local calcium signalling by inositol-1,4,5-trisphosphate in Purkinje cell dendrites. Nature 396: 753–756.
62. Fine A et al. (1988). Confocal microscopy: applications in neurobiology; Trends in Neurosciences 11(8): 346 – 351.
63. Fleidervish IA, Lasser-Ross N, Gutnick MJ, Ross WN (2010). Na^{+} imaging reveals little difference in action potential-evoked Na^{+} influx between axon and soma. Nat Neurosci. 13(7): 852–860.

64. Foust A, Popovic M, Zecevic D, McCormick DA (2010). Action potentials initiate in the axon initial segment and propagate through axon collaterals reliably in cerebellar Purkinje neurons. J Neurosci. 30(20): 6891–6902.
65. Foust AJ, Zampini V, Tanese D, Papagiakoumou E, Emiliani V (2015). Computer-generated holography enhances voltage dye fluorescence discrimination in adjacent neuronal structures. Neurophotonics. 2(2): 021007.
66. Gähwiler BH, Llano I (1989). Sodium and potassium conductances in somatic membranes of rat Purkinje cells from organotypic cerebellar cultures. J Physiol. 417: 105–122.
67. Glickstein M, Sultan F, Voogd J (2011). Functional localization in the cerebellum. Cortex, 47(1): 59–80.
68. Goldman-Wohl DS, Chan E, Baird D, Heintz N (1994). Kv3.3b: a novel Shaw type potassium channel expressed in terminally differentiated cerebellar Purkinje cells and deep cerebellar nuclei. J Neurosci. 14(2): 511–522.
69. Grynkiewicz, G. et al. (1985). A new generation of Ca2 þ indicators with greatly improved fluorescence properties. J. Biol. Chem. 260: 3440–3450
70. Hamill 0P, Marty A, Neher E, Sakmann B, Sigworth FJ (1981). Improved patch clamp techniques for high-resolution current recording from cells and cell-free membrane patches. Pflugers Arch. Eur. J. Physiol. 391: 85-100.
71. Hille B (1991). Ionic Channels of Excitable Membranes. Sinauer Associates, Sunderland, MA, USA.
72. Hille B (2001). Ion Channels of Excitable Membranes (third edition). Sinauer, Sunderland MA.
73. Hines ML, Carnevale NT (1998). The NEURON simulation environment. Neural Computation 9(6): 1179-1209
74. Hirano T, Hagiwara S (1989). Kinetics and distribution of voltage-gated Ca, Na and K channels on the somata of rat cerebellar Purkinje cells. Pflugers Arch. 413: 463–469.
75. Hodgkin A, Huxley A (1939). Action Potentials Recorded from Inside a Nerve Fibre. Nature 144: 710–711.
76. Hodgkin A, Huxley A, Katz B (1952). Measurement of current-voltage relations in the membrane of the giant axon of Loligo. J Physiol. 116(4): 424–448.
77. Hosy E, Piochon C, Teuling E, Rinaldo L, Hansel C (2011). SK2 channel expression and function in cerebellar cells. J. Physiol. 589: 3433–3440.

78. Hounsgaard J, Midtgaard J (1988). Intrinsic determinants of firing pattern in Purkinje cells of the turtle cerebellum in vitro. J Physiol. 402: 731–749.
79. Hoxha E, Tempia F, Lippiello P, Miniaci MC (2016). Modulation, Plasticity and Pathophysiology of the Parallel Fiber-Purkinje Cell Synapse. Front Synaptic Neurosci. 8:35.
80. Hu W, Tian C, Li T et al. (2009). Distinct contributions of Nav1.6 and Nav1.2 in action potential initiation and backpropagation. Nat Neurosci 12: 996–1002.
81. Isope P, Hildebrand ME, Snutch TP (2012). Contributions of T-type voltage-gated calcium channels to postsynaptic calcium signaling within Purkinje neurons. Cerebellum 11: 651-665.
82. Jaafari N, Canepari M (2016). Functional coupling of diverse voltage-gated Ca(2+) channels underlies high fidelity of fast dendritic Ca(2+) signals during burst firing. J Physiol. 594(4): 967–983.
83. Jaafari N, Canepari M (2016). Functional coupling of diverse voltage-gated Ca2+ channels underlies high-fidelity of fast dendritic Ca2+ signals during burst firing. J Physiol 594: 2557-2558.
84. Jaafari N, De Waard M, Canepari M (2014). Imaging Fast Calcium Currents beyond the Limitations of Electrode Techniques. Biophys J 107: 1280-1288.
85. Jaafari N, Marret E. Canepari M (2015). Using simultaneous voltage and calcium imaging to study fast Ca2+ channels. Neurophotonics 2: 021010.
86. Jabłoński AZ (1935). Über den Mechanismus der Photolumineszenz von Farbstoffphosphoren. Physik 94: 38.
87. Jurkat-Rott K, Holzherr B, Fauler M, Lehmann-Horn F (2010). Sodium channelopathies of skeletal muscle result from gain or loss of function. Pflugers Arch. 460(2): 239–248.
88. Kole M, Ilschner S, Kampa B et al. (2008). Action potential generation requires a high sodium channel density in the axon initial segment. Nat Neurosci. 11: 178–186.
89. Kole MH, Letzkus JJ, Stuart GJ (2007) Axon initial segment Kv1 channels control axonal action potential waveform and synaptic efficacy. Neuron 55: 633–647.
90. Kopp-Scheinpflug C, Tempel BL (2015). Decreased temporal precision of neuronal signaling as a candidate mechanism of auditory processing disorder. Hear Res. 330(Pt B):213–220.
91. Kosaka T, Kosaka K, Nakayama T, Hunziker W, Heizmann CW (1993). Axons and axon terminals of cerebellar Purkinje cells and basket cells have higher levels of

parvalbumin immunoreactivity than somata and dendrites: quantitative analysis by immunogold labeling. Exp Brain Res. 93:483–491.

92. Kozlov S (2018). Animal toxins for channelopathy treatment. Neuropharmacology 132: 83-97.
93. Kushmerick MJ, Larson RE, Davies RE (1969). The chemical energetics of muscle contraction I. Activation heat, heat of shortening and ATP utilization for activation-relaxation processes. Proc. R. Soc. Lond. B 174:1036.
94. Lasser-Ross N, Ross WN (1992). Imaging voltage and synaptically activated sodium transients in cerebellar Purkinje cells. Proc. R. Soc. Lond. B 247:1318.
95. Latorre R, Oberhauser A, Labarca P, Alvarez O (1989). Varieties of calcium-activated potassium channels. Annu Rev Physiol. 51:385–399.
96. Lauxmann S, Boutry-Kryza N, Rivier C, Mueller S, Hedrich UB, Maljevic S, Szepetowski P, Lerche H, Lesca G (2013). An SCN2A mutation in a family with infantile seizures from Madagascar reveals an increased subthreshold Na^+ current. Epilepsia 54: e117–e121.
97. Lazarov E, Dannemeyer M, Feulner B, Enderlein J, Gutnick MJ, Wolf F et al. (2018). An axon initial segment is required for temporal precision in action potential encoding by neuronal populations. Sci. Adv. 4: aau8621.
98. Léna I, Mantegazza M (2019). NaV1.2 haploinsufficiency in Scn2a knock-out mice causes an autistic-like phenotype attenuated with age. Sci Rep. 9(1):12886.
99. Linaro D, Storace M, Giugliano M (2011). Accurate and fast simulation of channel noise in conductance-based model neurons by diffusion approximation. PLoS computational biology, 7(3): e1001102.
100. Llano I, Marty A, Armstrong CM, Konnerth A (1991). Synaptic- and agonist-induced excitatory currents of Purkinje cells in rat cerebellar slices. J Physiol. 434: 183-213.
101. Llinás R, Sugimori M, Lin J-W, et al. (1989). Blocking and isolation of a calcium channel from neurons in mammals and cephalopods utilizing a toxin fraction (FTX) from funnel-web spider poison. Proceedings of the National Academy of Sciences of the United States of America. 86:1689–1693.
102. Llinas R., Sugimori M. (1980). Electrophysiological properties of in vitro Purkinje cell dendrites in mammalian cerebellar slices. J. Physiol. 305, 197–213.
103. Lorincz A, Nusser Z (2008). Cell-type-dependent molecular composition of the axon initial segment. J Neurosci. 28(53):14329–14340.

104. Losonczy A, Makara J, Magee J (2008). Compartmentalized dendritic plasticity and input feature storage in neurons. Nature 452, 436–441.

105. Maeda H, Ellis-Davies GC, Ito K, Miyashita Y, Kasai H (1999). Supralinear Ca^{2+} signaling by cooperative and mobile Ca^{2+} buffering in Purkinje neurons. Neuron 24:989–1002.

106. Magee JC, Johnston D (1997). A synaptically controlled, associative signal for Hebbian plasticity in hippocampal neurons. Science 275: 209–213.

107. Magee JC, Johnston D (2005). Plasticity of dendritic function. Curr Opin Neurobiol 15:334–342.

108. Mainen ZF, Joerges J, Huguenard JR, Sejnowski TJ (1995). A model of spike initiation in neocortical pyramidal neurons. Neuron 15:1427–1439.

109. Maki BA, Cummings KA, Paganelli MA, Murthy SE, Popescu GK (2014). One-channel cell-attached patch-clamp recording. J Vis Exp. 88:51629.

110. Mantegazza M, Rusconi R, Scalmani P, Avanzini G, Franceschetti S (2010). Epileptogenic ion channel mutations: from bedside to bench and, hopefully, back again. Epilepsy Res. 92: 1–29.

111. Markov A (1906). Extension de la loi de grands nombres aux evénements dependants les uns déautres. Bulletin de la societé physico-mathématique de Kasan ´ (2) 15(4):135–156. In Russian.

112. McDougal RA, Morse TM, Carnevale T, Marenco L, Wang R, Migliore M, Miller PL, Shepherd GM, Hines ML. Twenty years of ModelDB and beyond: building essential modeling tools for the future of neuroscience. J Comput Neurosci 42:1-10, 2017.

113. McGeown JG (2010). Seeing is believing! Imaging Ca^{2+}-signalling events in living cells. Exp Physiol. 95(11):1049–1060.

114. Meeks JP, Mennerick S (2007). Action Potential Initiation and Propagation in CA3 Pyramidal AxonsJournal of Neurophysiology 97(5): 3460-3472.

115. Meisler MH, Kearney JA (2005). Sodium channel mutations in epilepsy and other neurological disorders. J Clin Invest. 115(8):2010–2017.

116. Minassian NA, Gibbs A, Shih AY, Liu Y, Neff RA, Sutton SW, Mirzadegan T, Connor J, Fellows R, Husovsky M, Nelson S, Hunter MJ, Flinspach M, Wickenden AD (2013). Analysis of the structural and molecular basis of voltage-sensitive sodium channel inhibition by the spider toxin huwentoxin-IV (μ-TRTX-Hh2a). J Biol Chem 288:22707-22720.

117. Minta A, Tsien RY (1989). Fluorescent indicators for cytosolic sodium. J. Biol. Chem. 264: 19449-.

118. Miyazaki K, Ross WN (2015). Simultaneous Sodium and Calcium Imaging from Dendrites and Axons. eNeuro 2 pii: ENEURO.0092-15.

119. Moore JW (2010). A personal view of the early development of computational neuroscience in the USA. Front Comput Neurosci. 4:20.

120. Moore JW, Stockbridge N, Westerfield M (1983). On the site of impulse initiation in a neurone. J Physiol (Lond) 336:301–311.

121. Nakada C, Ritchie K, Oba Y, Nakamura M, Hotta Y, Iino R, Kasai RS, Yamaguchi K, Fujiwara T, Kusumi A (2003). Accumulation of anchored proteins forms membrane diffusion barriers during neuronal polarization. Nat. Cell Biol. 5:626–632.

122. Narahashi T, Moore JW, Scott WR (1964). Tetrodotoxin blockage of sodium conductance in lobster giant axons. J Gen Physiol. 47(5):965–974.

123. Naumann G, Lippmann K, Eilers J (2018). Photophysical properties of Na^+-indicator dyes suitable for quantitative two-photon fluorescence-lifetime measurements. Journal of Microscopy 272: 136-144.

124. Naundorf B,Wolf f, Volgushev M (2006). Unique features of action potential initiation in cortical neurons. Nature. 440:1060–1063.

125. Neher E, Sakmann B (1976). Single-channel currents recorded from membrane of denervated frog muscle fibres. Nature.

126. Nguyen JP, Shipley FB, Linder AN, Plummer GS, Liu M, Setru SU, Shaevitz JW, Leifer AM (2016). Whole-brain calcium imaging with cellular resolution in freely behaving caenorhabditis elegans. Proc. Natl. Acad. Sci. 113(8), E1074–E1081.

127. Nicholls et al. (2011). From Neuron to Brain fifth edition, Sinauer Associates.

128. Nikolenko V, Watson BO, Araya R, Woodruff A, Peterka DS, Yuste R (2008). SLM Microscopy: Scanless Two-Photon Imaging and Photostimulation with Spatial Light Modulators. Front Neural Circuits 2:5.

129. Nilius B, Hess P, Lansman J et al. (1985). A novel type of cardiac calcium channel in ventricular cells. Nature 316: 443–446.

130. Nishigaki T, Wood CD, Shiba K, Baba SA, Darszon A (2006). Stroboscopic illumination using light-emitting diodes reduces phototoxicity in fluorescence cell imaging. BioTechniques 41:191–197.

131. Oerster HC (1820). Experimenta circa effectum conflictus electrici in acun magneticum,Nuremburg, Schrag'schen Buchhandlung.

132. Oertner TG (2002).Functional imaging of single synapses in brain slices. Exp. Physiol. 87: 733–736.

133. Osorio N, Cathala L, Meisler MH, Crest M, Magistretti J, Delmas P (2010). Persistent Nav1.6 current at axon initial segments tunes spike timing of cerebellar granule cells. J Physiol. 588:651–670.

134. Otsu Y, Marcaggi P, Feltz A, Isope P, Kollo M, Nusser Z, Mathieu B, Kano M, Tsujita M, Sakimura K, Dieudonné S (2014). Activity-dependent gating of calcium spikes by A-type K^+ channels controls climbing fiber signaling in Purkinje cell dendrites. Neuron 84:137-151.

135. Öz P, Huang M, Wolf F (2015). Action potential initiation in a multi-compartmental model with cooperatively gating Na channels in the axon initial segment. J Comput Neurosci 39: 63.

136. Palmer LM, Clark BA, Gründemann J, Roth A, Stuart GJ, Häusser M (2010). Initiation of simple and complex spikes in cerebellar Purkinje cells. J Physiol. 588(Pt 10):1709–1717.

137. Palmer LM, Stuart GJ (2006). Site of action potential initiation in layer 5 pyramidal neurons. J. Neurosci. 26: 1854–1863.

138. Papagiakoumou, E. (2013), Optical developments for optogenetics. Biol. Cell, 105: 443-464.

139. Papagiakoumou, E., Anselmi, F., Bègue, A. et al. (2010). Scanless two-photon excitation of channelrhodopsin-2. Nat Methods 7, 848–854.

140. Patterson GH (2009). Fluorescence microscopy below the diffraction limit. Semin Cell Dev Biol. 20(8):886–893.

141. Penjweini R, Loew HG, Hamblin MR, Kratky KW (2012). Long-term monitoring of live cell proliferation in presence of PVP-Hypericin: a new strategy using ms pulses of LED and the fluorescent dye CFSE. J Microsc. 245(1):100–108.

142. Popovic MA, Foust AJ, McCormick DA, Zecevic D (2011). The spatio-temporal characteristics of action potential initiation in layer 5 pyramidal neurons: a voltage imaging study. J Physiol. 589(17):4167–4187.

143. Pozzi P, Gandolfi D, Tognolina M, Chirico G, Mapelli J, D'Angelo E (2015). High-throughput spatial light modulation two-photon microscopy for fast functional imaging. Neurophotonics 2(1):015005.

144. Rall W (1957). Membrane time constant of motoneurons. Science 126(3271): 454.

145. Raman IM, Bean BP (1997). Resurgent sodium current and action potential formation in dissociated cerebellar Purkinje neurons. J Neurosci. 17(12):4517–4526.

146. Rancz EA, Häusser M (2006). Dendritic calcium spikes are tunable triggers of cannabinoid release and short-term synaptic plasticity in cerebellar Purkinje neurons. J Neurosci 26:5428-5437.

147. Rizwan AP, Zhan X, Zamponi GW, Turner RW (2016). Long-Term Potentiation at the Mossy Fiber-Granule Cell Relay Invokes Postsynaptic Second Messenger Regulation of Kv4 Channels. J Neurosci 36: 11196-11207.

148. Roder P, Hille, C (2014). ANG-2 for quantitative Na+ determination in living cells by time-resolved fluorescence microscopy. Photochem. Photobiol. Sci. 13, 1699–1710.

149. Rosker C, Lohberger B, Hofer D, Steinecker B, Quasthoff S, Schreibmayer W. (2007). The TTX metabolite 4, 9-anhydro-TTX is a highly specific blocker of the Nav1. 6 voltage-dependent sodium channel. Am J Physiol Cell Physiol 293: 783–789.

150. Ross AE, Nguyen MD, Privman E, Venton BJ (2014). Mechanical stimulation evokes rapid increases in extracellular adenosine concentration in the prefrontal cortex. J Neurochem. 130(1):50–60.

151. Ross W, Fleidervish I, Lasser-Ross N (2013). Imaging Sodium in Axons and Dendrites Cold Spring Harb Protoc; doi:10.1101/pdb.prot074310

152. Safo PK, Regehr WG (2005). Endocannabinoids control the induction of cerebellar LTD. Neuron 48: 647–659.

153. Sakmann B, Neher E (1984). Patch clamp techniques for studying ionic channels in excitable membranes. Annu. Rev. Physiol. 46: 455-472.

154. Sanderson MJ, Smith I, Parker I, Bootman MD (2014). Fluorescence microscopy. Cold Spring Harb Protoc. doi:10.1101/pdb.top071795.

155. Schmidt-Hieber C, Jonas P, Bischofberger J (2008). Action potential initiation and propagation in hippocampal mossy fibre axons. J Physiol. 586(7):1849–1857.

156. Schorge S (2018). Channelopathies go above and beyond the channels. Neuropharmacology doi: 10.1016/j.neuropharm.2018.02.011.

157. Schwaller B (2010). Cytosolic Ca^{2+} buffers. Cold Spring Harb Perspect Biol. 2(11):a004051.

158. Shu Y, Yu Y, Yang J (2007), McCormick DA. Selective control of cortical axonal spikes by a slowly inactivating K+ current. Proc Natl Acad Sci USA 104(27):11453–11458.

159. Silver RA, Momiyama A, Cull-Candy SG (1998). Locus of frequency-dependent depression identified with multiple-probability fluctuation analysis at rat climbing fibre-Purkinje cell synapses. J. Physiol. 510 881–902. 10.1111/j.1469-7793.1998.881bj.x

160. Smith MR, Smith RD, Plummer NW, Meisler MH, Goldin AL (1998). Functional analysis of the mouse Scn8a sodium channel. J. Neurosci. 18, 6093–6102.

161. Solinas S, Forti L, Cesana E, Mapelli J, De Schutter E, D'Angelo E (2007). Computational reconstruction of pacemaking and intrinsic electroresponsiveness in cerebellar Golgi cells. Front Cell Neurosci. 1:2. doi:10.3389/neuro.03.002.2007.

162. Song L, Hennink E, Young T, Tanke H (1995). Photobleaching kinetics of fluorescein in quantitative fluorescence microscopyBiophys. J. 68: 2588-2600.

163. Spratt PWE, Ben-Shalom R, Keeshen CM, Burke KJ Jr, Clarkson RL, Sanders SJ, Bender KJ (2019). The Autism associated Gene Scn2a contributes to dendritic excitability and synaptic function in the prefrontal cortex. Neuron 103(4):673-685.e5.

164. Spring and Davidson, MicroscopyU/ introduction to fluorescence microscopy.

165. Stenmark H (2009). Seeing is believing. Nat.Rev.Mol.Cell Biol. 10:582.

166. Sterrat D, Graham B, Gillies A, Willshaw D (2011). Principles of computational modelling in neuroscience. University Press, Cambridge, UK.

167. Stocker M (2004). Ca^{2+}-activated K^{+} channels: molecular determinants and function of the SK family. Nat Rev Neurosci 5: 758–770.

168. Stokes GG (presented: 1850; published: 1856) . On the numerical calculation of a class of definite integrals and infinite series. Transactions of the Cambridge Philosophical Society 9(I): 166–188.

169. Stuart G, Häusser M (1994). Initiation and spread of sodium action potentials in cerebellar Purkinje cells. Neuron 13:703.

170. Stuart GJ and Spruston N (1995). Probing dendritic function with patch pipettes. Curr. Opin. Neurobiol. 5(3): 389-394.

171. Stuart GJ, Sakmann B (1994). Active propagation of somatic action potentials into neocortical pyramidal cell dendrites. Nature 367:69–72.

172. Stuart, G and Nelson Spruston (1995). Probing dendritic function with patch pipettes. Current opinion in neurobiology 5 3: 389-94.

173. Sugawara T, Mazaki-Miyazaki E, Ito M, Nagafuji H, Fukuma G, Mitsudome A, Wada K, Kaneko S, Hirose S, Yamakawa K (2001) Nav1.1 mutations cause febrile seizures associated with afebrile partial seizures. Neurology 57: 703-705.

174. Swensen AM, Bean BP (2003). Ionic mechanisms of burst firing in dissociated Purkinje neurons. J Neurosci. 23(29):9650–9663.

175. Szabo V, Ventalon C, De Sars V, Bradley J, Emiliani V (2014). Spatially selective holography photoactivation and functinal fluorescence imaging in freely behaving mice with a fiberscope. Neuron 84(6):1157-69.

176. Takahara Y, Matsuki N, Ikegaya Y (2011). Nipkow confocal imaging from deep brain tissues J. Integr. Neurosci., 10: 121-129.

177. Takechi H, Eilers J, Konnerth A (1998). A new class of synaptic response involving calcium release in dendritic spines. Nature 396:757–760.

178. Tanese D, Weng JY, Zampini V, et al. (2017). Imaging membrane potential changes from dendritic spines using computer-generated holography. Neurophotonics 4(3):031211.

179. Tempia F, Alojado ME, Strata P, Knöpfel T (2001). Characterization of the mGluR1-mediated electrical and calcium signaling in Purkinje cells of mouse cerebellar slices. J. Neurophysiol. 86: 1389–1397.

180. Tempia F, Kano M, Schneggenburger R, Schirra C, Garaschuk O, Plant T, Konnerth A (1996). Fractional calcium current through neuronal AMPA-receptor channels with a low calcium permeability. J Neurosci. 16:456–466.

181. Tombola F, Pathak MM, Isacoff EY (2006). How does voltage open an ion channel? Annu Rev Cell Dev Bion 22: 23-52.

182. Tominaga T, Tominaga Y (2013). A new nonscanning confocal microscopy module for functional voltage-sensitive dye and Ca^{2+} imaging of neuronal circuit activity. J. Neurophysiol. 110(2): 553–561.

183. Usowicz MM, Sugimori M, Cherksey B, Llinás R (1992). P-type calcium channels in the somata and dendrites of adult cerebellar Purkinje cells. Neuron 19:1185-1199.

184. Van Wart A, Trimmer JS, Matthews G. Polarized distribution of ion channels within microdomains of the axon initial segment. J Comp Neurol 500: 339–352.

185. Veys K, Snyders D, De Schutter E (2013). Kv3.3b expression defines the shape of the complex spike in the Purkinje cell. Front Cell Neurosci 7:205.

186. Williams SR, Mitchell SJ (2008). Direct measurement of somatic voltage clamp errors in central neurons. Nat. Neurosci 11(7): 790-798.

187. Wollner DA, Catterall WA (1986). Localization of sodium channels in axon hillocks and initial segments of retinal ganglion cells. Proc Natl Acad Sci USA 83:8424–8428.

188. Womack MD, Chevez C, Khodakhah K (2004). Calcium-activated potassium channels are selectively coupled to P/Q-type calcium channels in cerebellar Purkinje neurons. J Neurosci 24:8818–8822.

189. Yang W, Miller JE, Carrillo-Reid L, et al. (2016). Simultaneous Multi-plane Imaging of Neural Circuits. Neuron 89(2):269–284.

190. Ye M, Yang J, Tian C, et al. (2018). Differential roles of NaV1.2 and NaV1.6 in regulating neuronal excitability at febrile temperature and distinct contributions to febrile seizures. Sci Rep. 8(1):753. Published 2018 Jan 15.

191. Ye Mingyu, Yang J, Tian C et al. (2018). Differential roles of NaV1.2 and NaV1.6 in regulating neuronal excitability at febrile temperature and distinct contributions to febrile seizures. Sci Rep 8:753

192. Yu FH, Yarov-Yarovoy V, Gutman GA, Catterall WA (2005). Overview of molecular relationships in the voltage-gated ion channel superfamily. Pharmacol Rev 57: 387–295.

193. Yu Y, Maureira C, Liu X, McCormick D (2010). P/Q and N channels control baseline and spike-triggered calcium levels in neocortical axons and synaptic boutons J. Neurosci., 30: 11858-11869.

194. Yu Y, Shu Y, McCormick DA (2008). Cortical action potential backpropagation explains spike threshold variability and rapid-onset kinetics. J Neurosci 28:7260–7272.

195. Yuste R (2015). From the neuron doctrine to neural networks. Nature Rev. Neurosci 16: 487-497.

196. Zagha E, Manita S, Ross WN, Rudy B (2010). Dendritic Kv3.3 potassium channels in cerebellar purkinje cells regulate generation and spatial dynamics of dendritic Ca2+ spikes. J Neurophysiol. 103(6):3516–3525.

197. Zhang Y, Bonnan A, Bony G, Ferezou I, Pietropaolo S, Ginger M, Sans N, Rossier J, Oostra B, LeMasson G, Frick A (2014). Dendritic channelopathies contribute to neocortical and sensory hyperexcitability in Fmr1(-/y) mice. Nat Neurosci 17: 1701-1709.

198. Zylbertal A, Yarom Y, Wagner S (2017). The Slow Dynamics of Intracellular Sodium Concentration Increase the Time Window of Neuronal Integration: A Simulation Study. Front Comput Neurosci. 11:85.